TRANSPORT AND MAGNETIC PROPERTIES OF Pb₁₋ₓMnₓTe(Cr) Pb₁₋ₓMnₓTe(Mo)

A.I. Artamkin[1], A.E. Kozhanov[1], M. Arciszewska[2], W.D. Dobrowolski[2], T. Story[2], E.I. Slynko[3], V.E. Slynko[3], L.I. Ryabova[1], D.R. Khokhlov[1]

[1]M. V. Lomonosov Moscow State University, Vorobjevy Gory, 1, Moscow 119992, Russia
[2]Institute of Physics PAN, Al. Lotnikow, 32/46, Warsaw 02-668, Poland
[3]Chernovtsy Division of Institute of Problems of Semiconductor Material Science NUAS, I. Vilde, 5, Chernovtsy 274001, Ukraine

We have investigated transport and magnetic properties of the Pb₁₋ₓMnₓTe alloys doped with Cr and Mo. Anomalous behavior of the pinned Fermi level position with manganese concentration was observed. It was shown that in Pb₁₋ₓMnₓTe(Mo) the Fermi level could be pinned within the valence band as well as within the gap. In the latter case considerable persistent photoconductivity was observed at low temperatures. The studies of the magnetic susceptibility showed that magnetic properties of Pb₁₋ₓMnₓTe doped with Cr, Mo are defined by weak antiferromagnetic interaction between manganese ions.

1. Introduction

A^4B^6 group semiconductors are well-known materials for the infrared optoelectronics. Lead chalcogenides and some of their solid solutions are the most important examples of them. Lead telluride is a narrow-gap semiconductor, which has a cubic face-centered lattice of NaCl type. The direct gap is 190 meV at T = 0 K and it increases with the temperature rise at the rate of 0.4 meV/K. Extrema of the valence and conduction bands are located at the *L*-point of the Brillouin zone. Lead telluride-based solid solutions grow with a high deviation from the stoichiometry and all native defects are electrically active, so high concentration of vacancies and interstitial atoms results in high free carrier concentration of about 10^{19} cm^{-3}. Free carrier density can be further controlled via doping of the initial PbTe with elements of several groups of the Periodic Table (e.g. I, III, V, VII group elements). Moreover this doping results in the strong and unusual effects which are not characteristic of the undoped material [1]. Doping of the lead telluride-based alloys with In or Ga leads to the Fermi level (FL) pinning effect and to the appearance of a long-term relaxation phenomena at low temperatures. In a certain range of indium concentration the FL can be pinned within the gap leading to the appearance of semiinsulating state at low temperatures. This is explained by assuming that the dopant serves as a multi-charge center [2]. The neutral (with respect to the lattice) In^{2+} state is unstable and decays to a donor or an acceptor: $2In^{2+} \rightarrow In^{+} + In^{3+}$.

The transition metal and rare earth impurities are of a special interest since the position of the respective impurity levels may be, in principle, tuned by the magnetic field. In PbTe(Yb) and PbTe(Cr), the FL is pinned in one of the allowed bands[3,4] and contrary to the indium dopant, the valence of the impurity atom is changed only by one: $Yb^{2+} \rightarrow Yb^{3+}$, $Cr^{2+} \rightarrow Cr^{3+}$. In this case the persistent photoconductivity and other long-term non-equilibrium processes are not observed. They appear only in the doped lead telluride-based alloys, for instance, in Pb₁₋ₓMnₓTe. In this case doping of PbTe with Mn increases the bandgap at the rate of 40 meV/mol.%Mn [5], but does not provide local or quasilocal levels in the vicinity of the actual bands. So if the FL is pinned by doping with other impurities in one of the allowed bands, variation of the Mn concentration may lead to the shift of the FL into

the gap and to the appearance of a semiinsulating state at low temperatures. In this case persistent photoconductivity and other long term non-equilibrium processes can be observed.

In this paper, we report on transport and magnetic properties of $Pb_{1-x}Mn_xTe$ alloys doped with Cr and Mo. Previously, in ytterbium doped $Pb_{1-x}Mn_xTe$ alloys giant negative magnetoresistance and persistent photoconductivity effects have been observed at low temperatures [6]. The impurity level formed by Cr is similar to Yb level. The difference is that $Pb_{1-x}Mn_xTe(Cr)$ is n-type semiconductor (instead of p-type in Yb case) and it would be interesting if such kind of effect may be observed in this case. The Mo impurity has the same electron structure of outer electron shell as Yb and Cr and has not been studied previously.

2. Samples

Bulk crystals were grown by the Bridgman technique. The concentration of Mn increased from the top to the end of the ingot and the concentration of Cr and Mo decreased. The ingot was cut into slices perpendicular to the growth direction. The concentration of dopants in each slice was determined by the energy dispersive X-ray fluorescence analysis for Cr doped samples and by the emission spectral analysis for samples doped with Mo. Samples of the size $1 \times 1 \times 5$ mm^3 were cut from the slices. Electrical contacts to the n-type samples were soldered with indium and to the p-type samples were made by welding platinum wires. Galvanomagnetic, photoelectrical and magnetic susceptibility measurements were performed in the temperature range 4.2 – 300 K.

3. Experimental Results
3.1. Transport Measurements

The temperature dependences of the resistance were measured for all samples. For the several samples doped with Cr, such dependence had an activation part at temperatures $T > 30$ K followed by saturation at low temperatures. In these samples the persistent photoconductivity effect was observed at $T < 35$ K (fig.1a). It is interesting to note that the activation energy calculated on linear parts of the curves by formula $\rho = \rho_0 \exp(E_a/2kT)$ dropped with the increase of Mn content N_{Mn} (Table 1). The temperature dependences of resistance of other chromium doped samples were of metallic type.
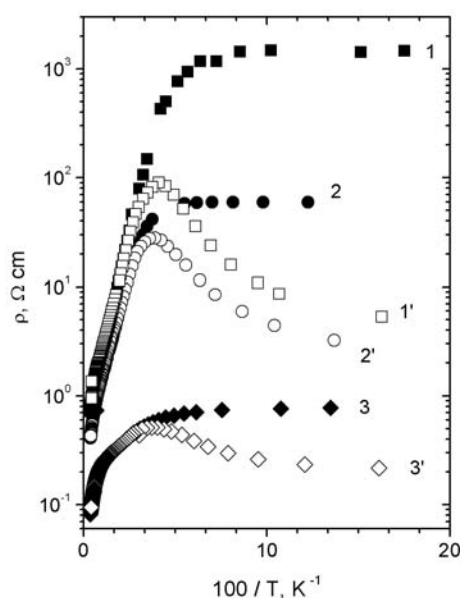

Figure 1a. Temperature dependences of resistivity of $Pb_{1-x}Mn_xTe(Cr)$ taken in darkness (1-3) and under infra-red illumination (1'-3'). Mn concentration, mol.%: 1, 1' – 11.2; 2, 2' – 14.2; 3, 3' – 18.2.
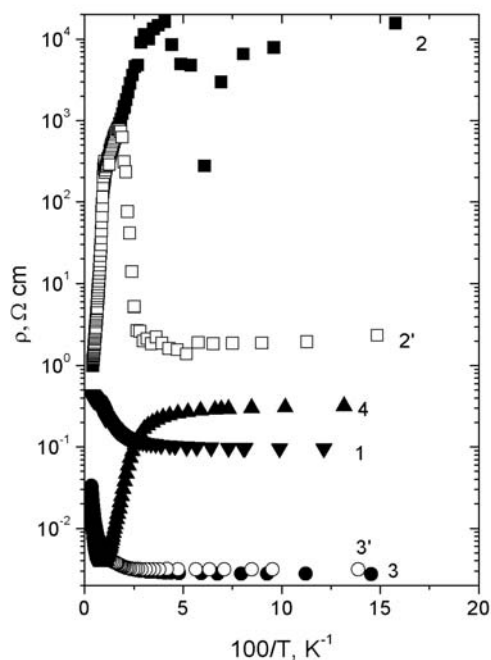
Figure 1b. Typical temperature dependences of resistivity of four groups of $Pb_{1-x}Mn_xTe(Mo)$ samples in the darkness (solid dots) and under infra-red illumination (open dots). $1 - N_{Mn} = 9.5$ mol.%, $N_{Mo} = 0.015$ at.%; 2, 2' – 3.56 mol.%, 0.025 at.%; 3, 3'–7 mol.%, 0.025 at.%; 4-19.94 mol.%, 0.84 at.%.

Table 1. Activation energy E_a and the temperature of the appearance of the photoconductivity T_C for $Pb_{1-x}Mn_xTe(Cr)$.

N_{Mn}, mol.%	N_{Cr}, at.%	E_a, meV	T_C, K
18.2	< 0.5	5.4	38.6
14.2	< 0.5	21.7	35.9
11.2	< 0.5	25.2	38.9

The samples of molybdenum doped $Pb_{1-x}Mn_xTe$ are divided to four groups (fig.1b) with the respect to the type of temperature dependences of resistivity. One may note that this dividing correlates with the concentration of Mo. So the first group consists of the samples with $N_{Mo} < 0.018$ at.%, the second one $0.018 < N_{Mo} < 0.038$ at.%, the third one $0.04 < N_{Mo} < 0.4$ at.%, and $N_{Mo} > 0.4$ at.% for the fourth group. Infrared illumination leads to appearance of considerable persistent photoconductivity at $T < 50$ K for the second group samples. The amplitude of this effect falls with the Mo concentration rising.
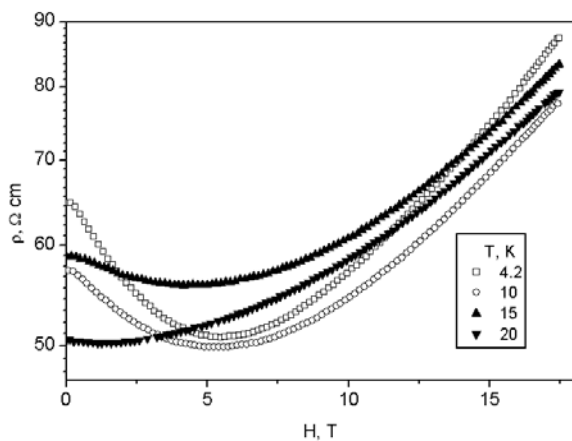

Figure 2a. Magnetic field dependence of resistivity of $Pb_{1-x}Mn_xTe(Cr)$. $N_{Mn} = 14.2$ mol.%.
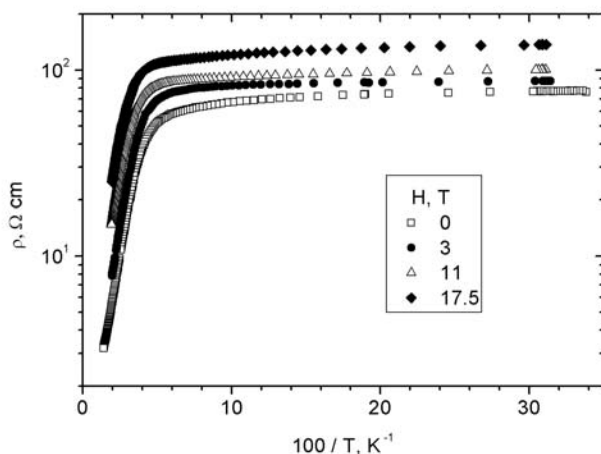
Figure 2b. Temperature dependences of resistivity of $Pb_{1-x}Mn_xTe(Cr)$ sample at different magnetic fields.
$N_{Mn} = 14.2$ mol.%.

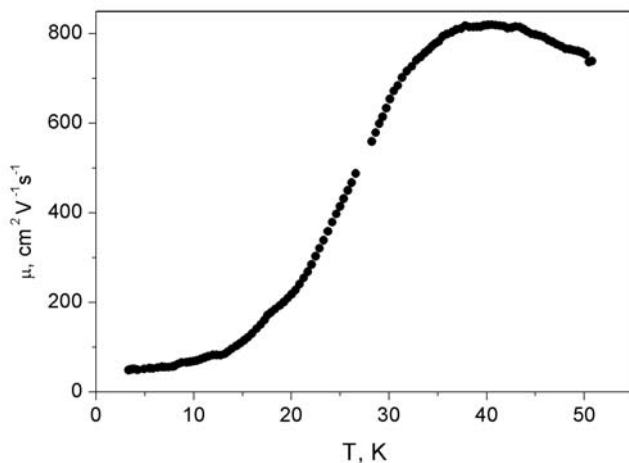Figure 3. Typical temperature dependence of Hall mobility of $Pb_{1-x}Mn_xTe(Cr)$, $x = 0.182$.

For $Pb_{1-x}Mn_xTe(Cr)$, the negative magnetoresistance was observed at temperatures less than 15 K (fig.2a). The amplitude of the effect is much lower than in the case of $Pb_{1-x}Mn_xTe(Yb)$ [6], but is still about 30%, that it is much higher than the negative magnetoresistance normally observed for disordered systems. The drop of the resistance in magnetic field decreases with increasing temperature and disappears at $T > 15$ K. It can be seen from fig.2b that the resistance gradually rises with lowering temperature in the field intervals $H < 5$ T and $H > 8$ T at the temperatures below 15 K. However, the sample resistance almost saturates at temperatures less than 10 K in the field interval 5 T $< H < 8$T. It is important to note that the temperature dependence of the resistance consists of two activation parts at $H < 5$ T. The activation energy corresponding to the relatively high temperatures ($T > 15$ K) is about 5-6 meV and slightly rises with increasing magnetic field. While the low-temperature activation energy decreases with field going down to zero at $H \sim 5$ T. Then it appears again and increases at $H > 8$ T. The drop in the temperature dependence of the Hall mobility (fig.3) is the same as one normally observed in the disordered systems or in the situation when the conductivity is defined by percolation. The maximal value of mobility $\mu \sim 10^3$ cm^2/Vs is typical for the conduction band electrons in this temperature range. Data taken for the other $Pb_{1-x}Mn_xTe(Cr)$ samples demonstrate the same trends.

3.2. Magnetic Measurements

Measurements of the magnetic susceptibility χ at the temperatures from 4.2 K to 120 K were carried out for several samples of $Pb_{1-x}Mn_xTe(Cr)$ and $Pb_{1-x}Mn_xTe(Mo)$. All temperature dependences of the magnetic susceptibility demonstrate the Curie-Weiss behavior. The Curie temperature Θ_C for all measured samples is shown in table 2. The magnetic ion concentration N was estimated using the expression: $C = 1/(3 k_B) N S (S + 1) (g \mu_B)^2$, where C is the Curie constant from the Curie-Weiss formula $\chi = C/(T-\Theta_C)$, S is a spin of magnetic ion, g is a Lande g-factor, k_B is the Boltzmann constant, μ_B is the Bohr magneton.

Table 2. The results of magnetic measurements

N_{Cr}, at.%	N_{Mo}, at.%	N_{Mn}, mol.%	N, mol.%	Θ_C, K
0	0.019	3.76	3.8	-1,7
0	0.036	3.2	2.98	-1,4
0	0.052	2.62	2.32	-1,1
0	0.45	11.2	2.2	-1,0
0	0.847	19.94	2.56	-0,9
< 0.5	0	18.2	18.5	-4.4
< 0.5	0	14.2	16.88	-4.3
< 0.5	0	11.2	16.96	-4.4
< 0.5	0	1.6	14.18	-3.70
0.56	0	8.7	9	-0.15
0.2	0	6.6	8.82	-0.82
0.5	0	9.8	11.46	-0.6
0.25	0	8.1	9.94	-1.7

4. Discussion

Several unexpected experimental observation must be mentioned. The first one is the drop of the resistance activation energy with the increase of Mn content in $Pb_{1-x}Mn_xTe(Cr)$ (Table 1). As it is known, the FL is pinned high in the conduction band in PbTe(Cr) and is linked to the middle of the gap [3]. Therefore the increase of the Mn content that gives rise to the bandgap should provide a shift of the pinned FL below the conduction band bottom and further into the gap. A decrease in the impurity activation energy with increasing Mn content x is observed instead. The reason for such a behavior may be the influence of the degree of Cr doping on the position of the pinned FL.

For $Pb_{1-x}Mn_xTe(Cr)$, the activation part of the resistance temperature behavior observed at $T > 15$ K corresponds to the thermal activation of free electrons from the pinned FL to the conduction band as suggested by high value of mobility. It means that the conduction band free electrons contribute to the positive magnetoresistance observed at the low fields at elevated temperatures, but they do not contribute to the negative magnetoresistance effect.

The activation energy corresponding to the process observed at the low temperatures and in the low fields is much smaller than the distance between the impurity level that pins the chemical potential and the conduction band. The Hall data suggest that the charge carriers responsible for this activation have a much lower mobility. Therefore it is natural to assume that the mechanism of this low-temperature activation energy is the following. The amount of Cr in the samples is relatively high which leads to a considerable widening of the respective

impurity level. This widening results in the metallic-like impurity-band transport, as long as the FL is inside the middle part of the respective density of states distribution. This type of transport is observed in the intermediate range of magnetic fields $5\,T < H < 8\,T$. If the FL stays in the "tails" of the impurity density of state profile, the conductivity is defined by a thermal activation from the FL to the mobility edge in the impurity band. Apparently this situation takes place at low $H < 5\,T$ and high $H > 8\,T$ magnetic ranges.

The application of a magnetic field may result in the splitting of impurity states with the different spin directions. Under these conditions, the overall filling of the band does not change but filling of each of the spin-polarized impurity subbands may change and result in a shift of the FL with respect to the mobility edge in the lowest subband. In any case, it is clear that the effect is defined by peculiarities of the magnetotransport via the impurity band, not by the conduction band electrons, as in the II-VI semiconductors [7].

The origin of a different behavior of the Mo doped samples that has led us to divide them into four groups may be explained as follows. For the first group of samples, it is likely that the Mo concentration is not enough to compensate free carriers resulting from native defects, so the FL is not pinned in these samples. For the second group the most characteristic feature is the appearance of the photoconductivity effect at low temperatures. This effect has not been observed in undoped $Pb_{1-x}Mn_xTe$ solid solutions, so it is related to the presence of a molybdenum impurity level, which pins the FL within the gap.

For the third group of samples, the resistance drops by more than an order of magnitude with the temperature lowering from 300 K to 4.2 K. This effect is a signature of the FL pinning since in this case the resistance drops with lowering temperature not only due to the increase of mobility, but also because of the rise of the free hole concentration. For the fourth group of the Mo doped $Pb_{1-x}Mn_xTe$ samples, the FL is pinned by the molybdenum level within the gap. The saturation of resistance at low temperatures is likely to be related to the carrier transport via the Mo impurity level.

The Curie temperature estimated for all measured samples is negative which means that there is an antiferromagnetic interaction between magnetic ions. Mn concentration estimated from the Curie-Weiss formula appears to be equal to the values measured by the emission spectral analysis and by the X-ray fluorescence analysis. Therefore the magnetic properties of the material are defined by Mn ions only. Cr and Mo contributions to magnetic properties of $Pb_{1-x}Mn_xTe$ are small because their concentrations are much smaller than the Mn one.

References
[1] B.A. Akimov, A.V. Dmitriev, D.R. Khokhlov, L.I. Ryabova, Phys. Status Solidi A 137, 9 (1993).
[2] A.I. Belogorokhov, B.A. Volkov, I.I. Ivanchik, D.R. Khokhlov, JETP Letters 72, 178 (2000).
[3] L.M. Kashirskaya, L.I. Ryabova, O.I. Tananaeva, N.A. Shirokova, Sov. Phys. Semicond. 24, 848 (1990).
[4] I.I. Ivanchik, D.R. Khokhlov, S.V. Ponomarev, A.A. Terekhov, E. I. Slynko,Yu.K. Vygra-nenko, A. de Visser, in: Proc. 24 Intern. Conf. on Physics of Semiconductors, Jerusalem (Israel) 1998, ed. Gershoni D., World Scientific, Singapore 1998, Pt. VIII B, paper 8.
[5] J. Niewodniczanka-Zawadzka, G. Elsinger, L. Palmetshofer, A. Lopez-Otero, E.J. Fant-ner, G. Bauer, W. Zawadzki, Physica B&C 117-118, 458 (1983).
[6] I.I. Ivanchik, D.R. Khokhlov, A.V. Morozov, A.A. Terekhov, E.I. Slynko, V.E. Slynko, A. de Visser, W.D. Dobrowolski, Phys. Rev. B 61, R14889 (2000).
[7] A. Mycielski, J. Mycielski, J. Phys. Soc. Jpn. A 49, 807 (1980).

KINETIC MODEL OF RADIATIVE RECOMBINATION PROCESSES IN 2H-MoS₂ CRYSTALS

D. Dumchenko

Institute of Applied Physics, Academy of Sciences of Moldova, 5 Academiei str., MD-2028, Chisinau, Republic of Moldova

Abstract

Steady-state photoluminescence (PL) measurements revealed 2H-MoS₂ crystals. Two distinct radiative regions in the near infrared are performed. The first region consisting of several sharp lines is produced by bound excitons related to the halogen transport agent intercalated within the van der Waals gap of the layered compound. The second region is a broad spectral band, originates from the radiative recombination between an intrinsic defect center and the valence band in the conditions of a strong electron-phonon coupling. The spectral and temperature behavior of the PL intensity are described in the framework of a two-channel kinetic recombination model in thermal equilibrium conditions.

1. Introduction

2H-MoS₂ crystallizes in the hexagonal structure (space group $P6_3/mmc - D_{6h}^4$) consisting of covalently bonded S-Mo-S layers linked by weak van der Waals forces [1,2]. The unit cell contains two layers; the sulfur atoms in one layer are directly above the molybdenum atom in the next. These compounds are indirect band gap semiconductors [3,4,5]. It was shown [6,7] that the strong photoluminescence observed in synthetic MoS₂ crystals is caused by recombination of excitons bound to the neutral centers formed by the intercalation of halogen molecules Cl₂ placed in well-defined sites of the van der Waals gap.

In this work the results of experimental investigations and modelling, for the temperatures range 2÷150K and the energy range 0.7÷1.4eV are presented.

2. Experimental Results

The studied synthetic 2H-MoS₂ single crystals were grown by means of chemical vapor transport method, using chlorine Cl₂ as a transport agent. Naturally grown samples were cut from large natural bulk molybdenite crystals and then cleaved to produce fresh clean surfaces. The steady-state photoluminescence (PL) measurements were performed with a variable-temperature optical cryostat, a one-meter grating monochromator coupled to a cooled Ge-detector, and standard lock-in detection techniques. The luminescence excitation was provided by an Ar-ion laser (λ=514 nm). All spectra were corrected for the wavelength-dependent response of the optical system.

For investigated materials two distinct spectral regions were identified (fig. 1).

The first one is an excitonic region, located in the vicinity of the indirect band gap, consisting of several sharp zero-phonon lines and their vibronic replica. These lines are caused by recombination of excitons bound to halogen molecules, intercalated during the growth process.

The second spectral region is the IR vibronic broad band, characteristic also of natural $2H\text{-}MoS_2$ crystals without halogen impurities. This region is associated with an intrinsic defect of the host lattice, which acts as a shunt channel and contributes to the thermal quenching of the exciton emission at $T>60K$.
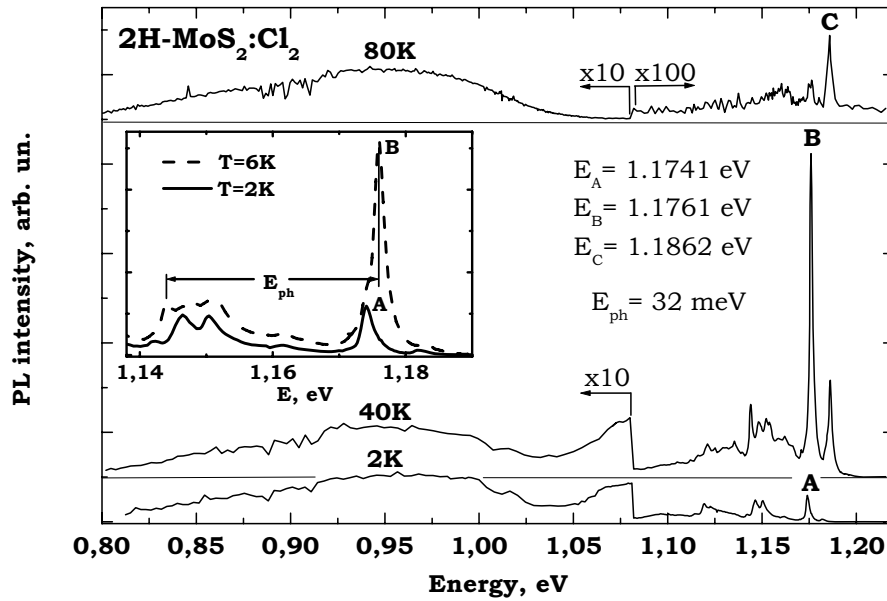

Fig. 1. Temperature evolution of the photoluminescence spectra of 2H-MoS2:Cl2 crystals.

In contrast to the broad band, the intensity of which remains constant up to almost 100K, the amplitudes of the sharp lines have a strong dependence on temperature. There were observed at least three zero-phonon spectral lines. The long wavelength line *A* is manifested only at lowest temperature (see insert to Fig.1).
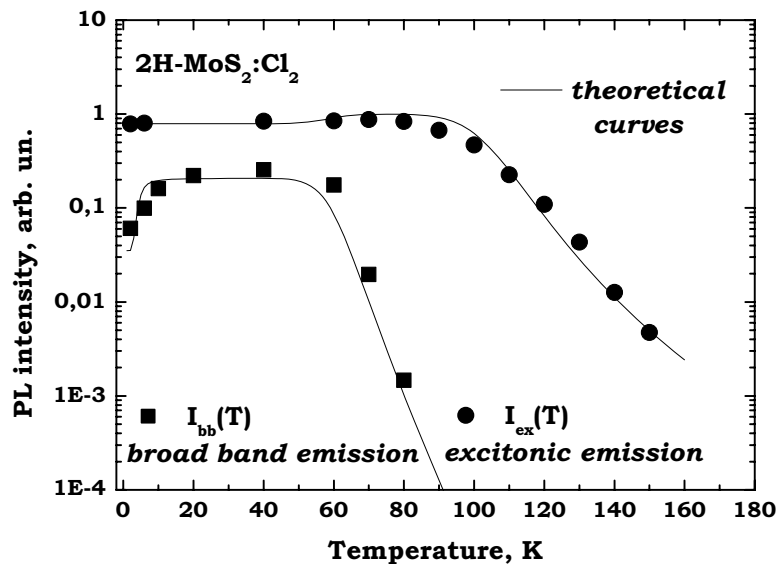

Fig. 2. Temperature dependence of the integrated intensity for the excitonic emission and the broadband emission.

The temperature increasing leads to the redistribution of the PL intensity to the sharp lines *B* and *C*. At *T*=6K the *A*-line can be observed just as a shoulder of the *B*-line. The *B*-line amplitude is the highest in the whole emission spectra up to *T*≈50K, when the *C*-line became dominating. At *T*>50K a fast thermal exponential quenching of the short wavelength emission occurs. The activation energy of this quenching is E_{q1}≈0.1eV. At *T*>80K already only the broad band luminescence is observed. The experimental temperature dependences of the broad band intensity as well as of the integral intensity of the three zero-phonon lines ($I_{ex}=I_A+I_B+I_C$) are presented in Fig.2 (dots).

3. Discussion

In order to describe the temperature behavior of the radiative spectral components we consider an *n*-type 2H-MoS$_2$ crystal structure that leads us to a level diagram (Fig. 3).
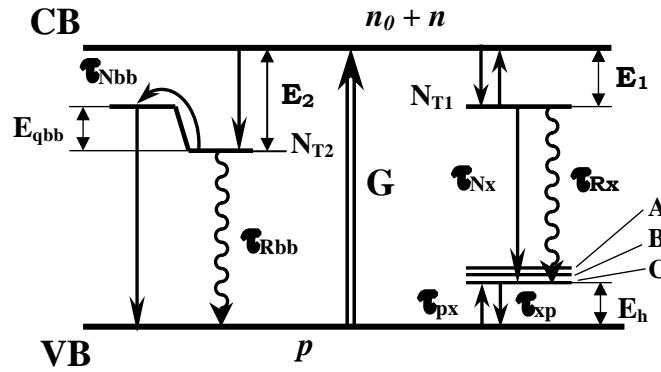

Fig. 3. Representation of level diagram with radiative and nonradiative processes.

Under the assumption of low-level excitation and thermal equilibrium the equations, which describe the kinetic behavior of minority carriers in n-type material, are given as follows:

$$\frac{dp}{dt} = G - p \cdot \upsilon_{th} \cdot \sigma_{px} \cdot \left(N_{T1}^e - N_{T1}^x \right) + \frac{N_{T1}^x}{\tau_{xp}} - p \cdot \frac{N_{T2}^e}{N_{T2}} \cdot \left(\frac{1}{\tau_{Rbb}} + \frac{1}{\tau_{Nbb}} \right),$$

$$\frac{dN_{T1}^x}{dt} = p \cdot \upsilon_{th} \cdot \sigma_{px} \cdot \left(N_{T1}^e - N_{T1}^x \right) - N_{T1}^x \cdot \left(\frac{1}{\tau_{Rx}} + \frac{1}{\tau_{Nx}} + \frac{1}{\tau_{xp}} \right).$$

Here *p* is the concentration of the minority holes, N_{T1}^e and N_{T2}^e the concentration of electron-occupied T_1-isoelectronic and T_2-deep centers, N_{T1}^x the concentration of centers which have an exciton bound to the site, $\tau_{Rx}(\tau_{Nx})$ is the bound exciton radiative (nonradiative) recombination time, $\tau_{Rbb}(\tau_{Nbb})$ - T_2-levels radiative (nonradiative) time (hole shunt-path capture time), σ_{px} is the hole capture cross section by electron occupied centers, υ_{th} is thermal velocity of minority carriers, τ_{xp} - isoelectronic trap exciton hole thermalization time and *G* is the excitation rate.

In *n*-type material the concentrations of electron-occupied isoelectronic and deep centers are in thermal equilibrium with the majority-carrier concentration

$$N_{T1}^e = f_{e1} \cdot N_{T2}, \quad N_{T2}^e = f_{e2} \cdot N_{T2} \; ,$$

where f_{e1} and f_{e2} are the electron occupancy probabilities of T_1 and T_2 centers respectively. In this case, from the steady-state solution

$$\frac{dN_{T1}^x}{dt} = 0 \quad \text{and} \quad \frac{dp}{dt} = 0,$$

assuming that in considered temperature range all deep T_2 -centers ($E_{T2} \cong 0.3$ eV) are electron-occupied ($f_{e2} = 1$, $N_{T2}^e = N_{T2}$), and that at low-level excitation $p << N_{T2}$, $N_{T1}^e >> N_T^x$, the following relationship results for the quantum efficiencies of the excitonic radiative recombination $\eta_{Rx}(T)$ and the broad band emission $\eta_{Rbb}(T)$:

$$\eta_{Rx} = \frac{N_{T1}^x}{\tau_{Rx}} \cdot \frac{1}{G} = \left(1 + \frac{\tau_{Rx}}{\tau_{Nx}}\right)^{-1} \cdot \left[1 + \frac{\tau_{cp}}{\tau_{Rbb}} \cdot \left(1 + \frac{\tau_{Rbb}}{\tau_{Nbb}}\right) \cdot \left(1 + \frac{\tau_{Rx}}{\tau_{xp}}\right)\right]^{-1} \, ,$$

$$\eta_{Rbb} = \frac{p}{\tau_{Rbb}} \cdot \frac{1}{G} = \left(1 + \frac{\tau_{Rbb}}{\tau_{Nbb}}\right)^{-1} \cdot \left\{1 - \left[1 + \frac{\tau_{cp}}{\tau_{Rbb}} \cdot \left(1 + \frac{\tau_{Rbb}}{\tau_{Nbb}}\right) \cdot \left(1 + \frac{\tau_{Rx}}{\tau_{xp}}\right)\right]^{-1}\right\},$$

where $\tau_{cp} \equiv \left(\upsilon_{th} \cdot \sigma_{px} \cdot N_{T1}^e\right)^{-1}$, are defined as the capture time of holes by electron-occupied isoelectronic centers and by nonradiative shunt centers respectively.

The kinetic equations were solved numerically as function of temperature and density of traps N_{T1} and N_{T2}. The curves obtained after calculations and the experimental points are presented in Fig. 2. How it can be seen, the curves obtained from our model fit with a good precision the temperature dependence of the quantum efficiencies of the excitonic emission and the broad band emission.

References

[1] A. Wilson and A.D. Yoffe, Adv. Phys. 18, 193 (1969).
[2] W.J. Schutte, J.L. De Boer, and F. Jellinek, J. Solid State Chem 70, 207 (1987).
[3] A. Aruchamy (ed), *Photoelectrochemistry and Photovoltaics of Layered Semiconductors,* (Kluwer Academic Publishers, 1992).
[4] Th. Böker, R. Severin, A. Müller, C. Janowitz, R. Manzke, D. Vob, P. Krüger, A. Mazur, J. Pollmann, Phys. Rev. B 64, 235305 (2001).
[5] A. Klein, S. Tiefenbacher, V. Eyert, C. Pettenkofer, W. Jaegermann , Phys. Rev. B 64, 205416 (2001).
[6] L. Kulyuk, E. Bucher, L. Charron, E. Fortin, A. Nateprov, and O. Schenker, Nonlinear Opt. 29, 501 (2002).
[7] L. Kulyuk, L. Charron and E. Fortin, Phys. Rev. B 68, 075314 (2003).

ELECTRONIC STRUCTURES OF LUMINESCENCE CENTERS IN PURE AND DEFECTIVE SCINTILLATION CRYSTALS AWO$_4$ (A = Pb, Cd, Zn)

Yu.A. Hizhnyi, S.G. Nedilko, T.N. Nikolaenko

Faculty of Physics, Kyiv National Taras Shevchenko University, 2, block 1, Glushkova av., 03022, Kyiv, Ukraine, e-mail: hizhnyi@univ.kiev.ua

Abstract

The electronic structures of the set of molecular clusters of dielectric oxide crystals AWO$_4$ (A = Pb, Cd, Zn), the sizes of which increase sequentially are *ab-initio* calculated by the Restricted Hartree-Fock (RHF) method. The results of calculations of molecular orbitals and energy dependences of partial densities of electronic states of different clusters are compared each to other and to experimental data. It is found that calculated electronic structures of the tungstate groups and cations which are surrounded in cluster by certain number of the nearest neighbor atoms of the crystals quite well represent the experimentally obtained value of the forbidden gap of corresponding AWO$_4$ crystal.

1. Introduction

Dielectric oxide crystals AWO$_4$ (A = Pb, Cd, Zn) are well known materials, which are widely used in various scintillation applications. PbWO$_4$ crystals are characterized by tetragonal crystal lattice of the scheelite type and possess space symmetry group I$_4$/a [1]. The cadmium and zinc tungstates are monoclinic wolframite-type crystals with the space group P2/c [2].

During the recent years the optical properties of these crystals were intensively studied experimentally [3, 4] and theoretically [5]. According to generally accepted view, the centers of luminescence in AWO$_4$ crystals are spatially and energetically localized objects, therefore, the intention to clarify the nature of luminescence in these crystals by means of calculations of the electronic structure of a separated crystal fragment – cluster looks quite grounded. Up to now we have published several works, where we developed our cluster approach in investigations of the electronic structure of luminescence centers in oxide crystals [6, 7]. In this work we intend to investigate in what way the size of a cluster determines representation of the optical properties of corresponding AWO$_4$ crystal.

2. Calculation Details

The following sequence of clusters was chosen for consideration. Firstly we consider only the anion component of a tungstate crystal – tungstate molecular group (WO$_4^{2-}$ in the case of lead tungstate, and WO$_6^{6-}$ in the case of cadmium and zinc tungstates). This was done, because the majority of researcher assume that luminescence of these crystals originates from the tungstate groups [3]. At the same time, almost all authors recognize that tungstate groups in AWO$_4$ undergo the influence of the corresponding cations of the crystals. In order to take into account this influence in calculations we constructed larger clusters, which contained two formula units – two cations and two tungstate groups. In the case of lead tungstate such cluster was denoted as PWO-2 (CWO-2 in the case of cadmium tungstate). And the third

types of clusters were the clusters in which the tungstate group and the cation were surrounded by the nearest neighbor atoms of the crystals. Such cluster of lead tungstate crystal is denoted as PWO-12. It was constructed of 12 FUs $PbWO_4$ (72 atoms). The cluster of $CdWO_4$ crystal is denoted as CWO-16. It was constructed of 104 atoms of the crystal, which represent 4 closely lying fragments of tungstate chains of WO_6 octahedrons (16 full FUs). Similar cluster of $ZnWO_4$ is denoted as ZWO-16. The central element (CE) was selected in each cluster. The CE comprises one tungstate group and the cation closest to it.

Calculations are carried out *ab-initio* by the Restricted Hartree-Fock (RHF) method using the PC GAMESS version [8] of the GAMESS (US) QC package [9]. Details of the calculations of partial densities of states (PDOS) $N_{a,r}(E)$ were described in our work [6]. The electronic structure of the CE was extracted from the results of the calculations of the whole cluster (energy levels of molecular orbitals ε_i and decomposition coefficients $C^i_{a,r}$ of molecular wave functions Ψ_i into atomic orbitals $\varphi_{a,r}$ where the index a denoted an atom, and r – an atomic orbital) in the following way. Only those $C^i_{a,r}$, which represent atoms of the CE were taken into account in calculation of $N_{a,r}(E)$.

3. Results and Discussion.

$PbWO_4$. As it is known, the edge of fundamental absorption of lead tungstate is located near 4 eV [4]. The photo-luminescence of $PbWO_4$, a blue band with maximum at 2.9 eV is excited in band with maximum at ~4 eV [10]. The calculated energies of molecular orbitals of tungstate group WO_4^{2-} with symmetry of free tungstate anion T_d are present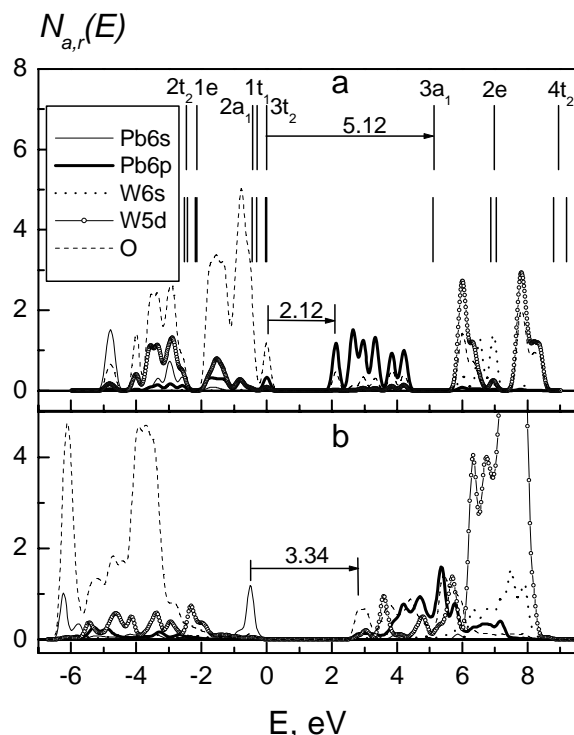ed in Fig. 1a (the upper row of vertical strokes). The lowest energy of $3t_2 - 3a_1$ transition in such group is 5.12 eV. It is obvious from the obtained values of transition energies that the excitation band of the luminescence at 4 eV or with fundamental absorption of the lead tungstate in this spectral region can be hardly associated with transitions in tungstate groups. Then the following question arises. Can calculations of such kind as we use give results, which will allow ascribing (at least qualitatively) of light absorption in this energy region (near 4 eV) to electronic transitions in certain object of the crystal (tungstate group, lead cation, point defect, etc.). Here are two possible ways to answer this question. The first is to take into account possible distortion of tungstate group induced by the crystal field. Due to this distortion the energies of MOs of tungstate group can be shifted with respect to the energies of free tungstate anion resulting in shifts of transition energies. In order to test this we

Fig. 1. Calculated MO energies of WO_4^{2-} groups (with T_d symmetry – upper strokes and with geometry as in $PbWO_4$ crystal – lower strokes), PDOS distributions $N_{a,r}(E)$ of PWO-2 cluster (a), and of the central element of PWO-12 cluster (b).

have modeled the distortion in calculation by taking the coordinates of O and W atoms being equal to coordinates of these atoms in $PbWO_4$ crystal. The results of this calculation are presented in the lower row of vertical strokes in Fig. 1a. As it is seen from the Figure, there are no substantial changes in positions of MOs, moreover the lowest energy of transition decreases only to 5.09 eV that is still far from 4 eV.

Another explanation of the question put above is that the transitions in Pb^{2+} cations have lower energies than tungstate groups and can provide the crystals absorption near 4 eV. It is obvious that in order to examine this in calculations the atomic orbitals of lead atoms must be involved into basis of the calculation. In order to realize this we constructed the cluster PWO-2, which contains Pb^{2+} cations (Fig. 1a). We have to note that unoccupied MOs of such system being of predominantly lead character are located below (from 2 to 4.5 eV) the MOs formed entirely by the states of tungstate group (from 6 to 9 eV). This means that the electronic states of Pb^{2+} cations should play an important role in formation of optical properties of $PbWO_4$ crystals. However, the energy distance between the highest occupied and the lowest unoccupied MOs of PWO-2 cluster is equal to 2.12 eV (Fig. 1a). This is much lower value than the energy of the fundamental absorption edge of the crystal (4 eV). Therefore we can conclude that the optical properties of lead tungstate crystal in the region of fundamental absorption can not be correctly described in calculation of a model system like PWO-2 cluster. In order to improve the situation we considered larger cluster PWO-12, in which the influence of the nearest atoms of the lead tungstate crystal on one Pb^{2+} cation and one WO_4^{2-} group is taken into account (Fig. 1b). As it is seen, the energy gap in this case (3.35 eV) is closer to 4 eV, than in the case of PWO-2 cluster. And moreover, if we consider the electronic transitions in Pb^{2+} cation and WO_4^{2-} group of the CE separately more accordance between calculations and experiment can be found. It was proved by good agreement between experimental reflection spectrum of $PbWO_4$ and calculated PDOS distribution of the CE [6]. So, we can conclude that the calculated electronic structure of the CE of PWO-12 cluster satisfactorily represents obtained experimentally optical properties of the lead tungstate crystal.

It should be also noted that such an object as Pb^{2+} cation of WO_4^{2-} tungstate group which is only partially surrounded in PWO-2 cluster by the nearest atoms of the crystal can be regarded as a defect center. Such centers can be lead cations and tungstate groups located on the crystal surface or on imaginary surface of micro-fragments in bulk of the crystal. As it is seen from the results of calculations (Fig. 1a), such defect centers are characterized by lower transition energies than the corresponding objects in the bulk of the crystal (associated with CE of PWO-12 cluster, Fig. 1b) and should have the electronic states in the forbidden gap of $PbWO_4$ crystal and, therefore, cause an additional absorption.

CdWO_4. Analogous sequence of clusters was considered for cadmium and zinc tungstate crystals. Since the results of calculations for these two crystals are in great measure similar we consider here only the case of $CdWO_4$ (Fig. 2). As it is known from experimental data, the edge of fundamental absorption of cadmium tungstate is located near 5 eV [11]. The calculated energy levels of molecular orbitals of WO_6^{6-} tungstate group with atomic coordinates of the group in $CdWO_4$ crystal are presented in Fig. 2a. As it is seen, the energy distance between the highest occupied and the lowest unoccupied MOs equals to 2.70 eV. The energy gap of CWO-2 cluster (the latter is similar to PWO-2) is 4.18 eV, which is closer to experimental data. And, at last, the energy distance between two valuable peaks of occupied and unoccupied electronic density of the central element of CWO-16 cluster (5.11 eV, Fig. 2b) is much closer to experimentally detected edge of fundamental absorption. This means that the calculated energy gap of the central element of CWO-16 cluster better represents the
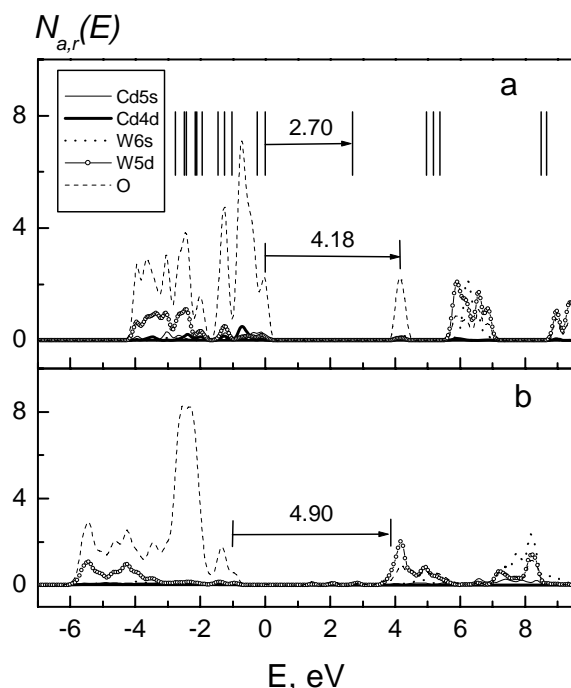
Fig. 2. Calculated MO energies of WO_6^{6-} group and PDOS distributions $N_{a,r}(E)$ of CWO-2 cluster (a); $N_{a,r}(E)$ distributions of the central element of CWO-16 cluster.

value of the forbidden gap (E_g) of the crystal than it was in the case of CWO-2 cluster or the WO_6^{6-} group. The situation is similar to the central element of PWO-12 cluster and $PbWO_4$ crystal (see above). Therefore the following general conclusion concerning the sizes of clusters in cluster modeling of the electronic structure of oxide crystals AWO_4 (A = Pb, Cd, Zn) should be made. The electronic structure of the tungstate group (WO_4^{2-} or WO_6^{6-}) and the A^{2+} cation which are surrounded in cluster by certain number of the nearest neighbor atoms of the crystals quite well represent the experimentally obtained value of E_g of corresponding AWO_4 crystal. Moreover, we found that addition of few formula units to PWO-12 cluster does not change (within the accuracy of 3 %) the PDOS distributions of the CE atoms of the cluster. But in order to prove that these distributions converge to some values when the size of the cluster increases, further investigations of larger clusters should be done. This is the aim of our future work.

Conclusion

From the calculations of the electronic structures of sequences of clusters with increasing sizes of AWO_4 (A = Pb, Cd, Zn) crystals it was found the following. The calculated energies of electronic transitions in the tungstate group (WO_4^{2-} or WO_6^{6-}) and the A^{2+} cation which are surrounded in cluster by the nearest neighbor atoms of the crystals quite well represent the experimentally obtained value of the forbidden gap of corresponding crystal.

Acknowledgement

References

[1] J.M. Moreau, Ph. Galez, J.P. Peigneux, M.V. Korzhik, J. Alloys Compd. 46, 238 (1996).
[2] M. Daturi, M.M. Borel, A. Leclaire, et al., J. Chem. Phys. 93, 2043 (1996).
[3] V. Nagirnyi, M. Kirm, A. Kotlov, et al., J. Lumin. 102-103, 597 (2003).
[4] I.A. Kamenskikh, V.N. Kolobanov, V.V. Mikhailin, et al., Nucl. Instrum. Methods A 470, 270 (2001).
[5] Y. Abraham, N.A.W. Holzwarth, R.T. Williams, Phys. Rev. B62, 1733 (2000).

[6] Yu.A. Hizhnyi, S.G. Nedilko, M.U. Bilyi, Rad. Effects and Defects in Solids 157, 839 (2002).
[7] Yu.A. Hizhnyi, S.G. Nedilko, J. Lumin. 102-103, 688 (2003).
[8] A.A. Granovsky, http://classic.chem.msu.su/gran/gamess/index.html
[9] M.W. Schmidt, K.K. Baldridge, J.A. Boatz, et al., J. Comput. Chem. 14, 1347-1363 (1993)
[10] M.U. Bilyi, S.G. Nedilko, Yu.A. Hizhnyi, et al., Ukrainian Phys. J. 47, 846-851 (2002).
[11] V. Nagirnyi, E. Feldbach, L. Jonsson, et al., Radiation Measurements 33, 601-604 (2001).

LONG-TERM RELAXATION OF PHOTOCONDUCTIVITY IN $Cd_{3-x}Zn_xAs_2$ CRYSTALS

A.F. Kniazev[1], A.V.Kochura[2]

[1]*State University, St. Radistcheva 33, Kursk 305000, Russia*
[2]*State Technical University, St. SO Let Octyabrja 94. Kursk 305040, Russia*

$Cd_{3-x}Zn_xAs_2$ solid solutions belong to the group of semiconductors $A^3 B^2$ [1]. Their properties are described in the detailed review [2]. These solutions cause interest because their band structure is likely to be similar to the band structure of $Cd_{1-x}Hg_xTe$. It was verified by establishing the characteristic dependence of the width of a forbidden gap on the composition of $Cd_{3-x}Zn_xAs_2$ crystals. The margins of the forbidden gap in Cd_3As_2 and in Zn_3As_2 at T=OK come to -0,1 electronvolt and 1,1 electronvolt correspondingly. This fact attracts attention to the mentioned solutions as possible materials for application in sensors of infrared emanation receivers. The introduction of admixture of group IV elements to solid solutions at x>1.5 helped to produce overcompensated crystals. In those crystals the photoconductivity was originally found [4]. The thermal characteristics of $Cd_{1-x}Zn_xAs_2$ crystal photoconductivity were investigated.

One of the most interesting photoelectric effects in semiconductors is the so-called long-term relaxation of photoconductivity (LRP). The phenomenon reveals itself in long periods (from minutes to hours) of photo response of relaxation when the light is on or off. The known phenomenon of the residual (frizzed) conductivity (RC) ought to be considered as a particular case of LRP. The phenomenon consists in conservation of unusually high, in comparison with equilibrium, margin of sample conductivity for a considerable period of time (up to $10^6 – 10^7$ sec) after the end of the sample light exposure. The researchers' interest in LTR and RC is determined by two factors – the possibility of practical application of the mentioned materials in optical electric memory units or vidicons and the nontrivial physical nature of the phenomena. The LPR is discovered in many types of semiconductors, both crystalline and amorphous. In review [6] the characteristics of LPR and RC are presented and the authors made an attempt to explain all the experimental results on the basis of a unified theory.

We pioneer the discovery of LRP and RC phenomena in the crystals of solid solutions $Cd_{3-x}Zn_xAs_2$ (x ≈ 1.8). The crystals of $Cd_{3-x}Zn_xAs_2$ with selenium doping were grown by Bridgman vertical method in the form of ingots with 10 mm in cross-section. Washers 0.5 mm thick were cut out of the ingots. The typical sample size was 5 mm x 3 mm x 0.5 mm. Copper wire contacts of 0.06 mm were soldered onto the washers. The sample was clued onto the cold pin of a cryostat. Light exposure was made with the help of a common filament lamp. The response signal was taken from the load resistor and was registered by SH-300 device or was sent to N308 logger in case the "fast" constituent of the relaxation characteristic was being investigated. The measurements were mostly taken at T=80 K. This article presents some experimental data of long-term relaxation of photoconductivity in $Cd_{3-x}Zn_xAs_2$ crystals with selenium doping.

Fig. 1 shows typical photocurrent relaxation curves for two samples with the composition of x ≈ 1.8. At the time t = 0 light exposure was stopped and afterwards the samples remained in darkness. There is a fast and a slow component in the relaxation time function. The process of photocurrent relaxation lasts for hours and tens of hours, which is

very characteristic of LRP and RC [6]. The phenomenon of the temperature quenching of the residual conductivity was also discovered in this type of crystals. In heating the crystals in darkness to T ≈ 200 K residual conductivity drops to zero, and in sample freezing to T = 77 K its conductivity equals with the initial level of conductivity.
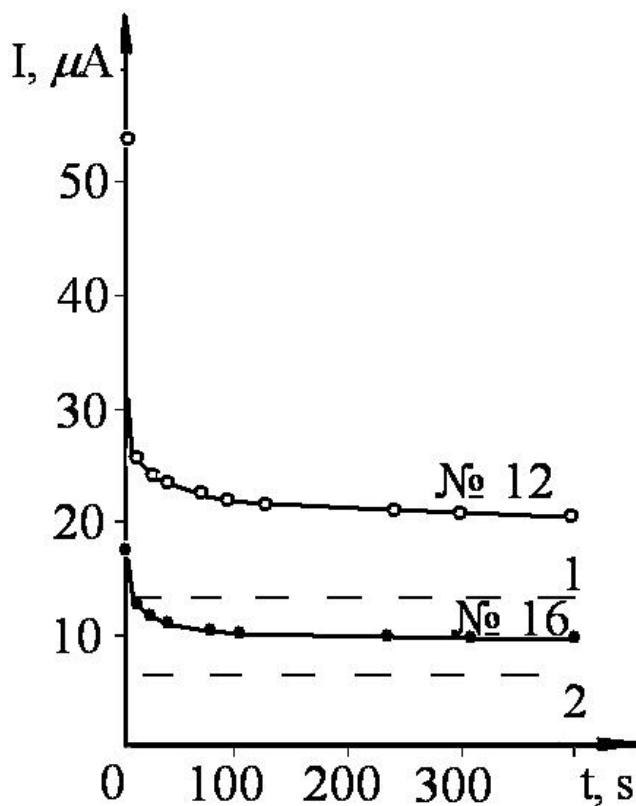

Fig 1. Photocurrent relaxation curves in $Cd_{3-x}Zn_xAs_2$ crystals, T=77K. 1 – photocurrent in dark room for the sample №12, 2 – for the sample №16.
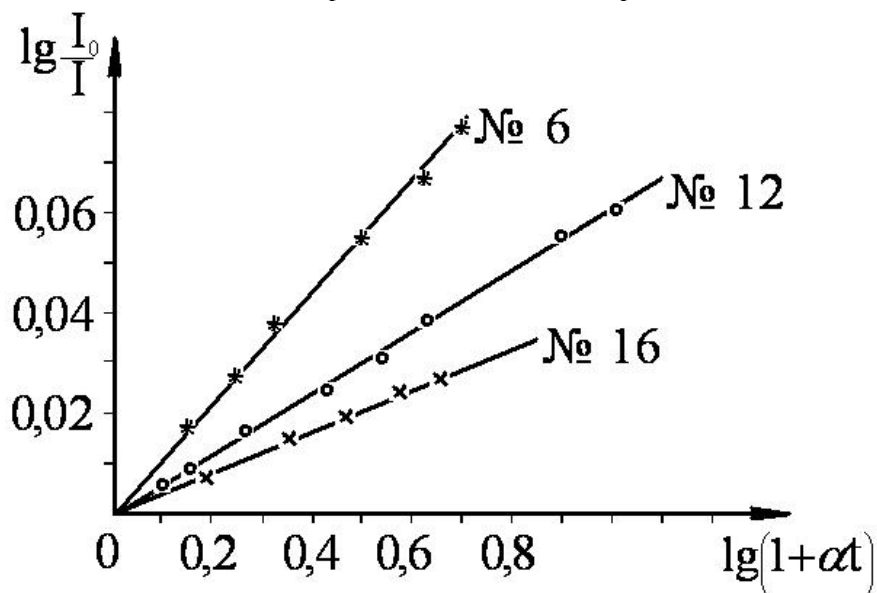

Fig. 2. The relations between $lg\ I_0/I = f\ (lg\ (1+ \alpha\ t))$. T=77K.

Samples №№ are shown on the plot.

The LPR phenomenon is explained on the basis of the double-barrier model, presented in [7]. According to this model it is supposed that there are two types of barriers in a semiconductor - the recombination barrier and the drift barrier, they are not physically separated. The precise calculation shows [7] that the photocurrent kinetics is determined by the following dependence:

$I=I_o (1+ \alpha t)^{-\gamma}$, where I_o is the current at the moment of time t_o, when the fast relaxation processes are over. The α and γ are the magnitudes to be calculated according to the double-barrier model. Fig. 2 shows relations between $lg I_o/I = f(1+ \alpha t)$.

The values of α and γ are calculated on the base of experimental dependences *lg $I_o/I \sim \gamma$ αt* and *lg $I_o/I \sim lg \alpha t$* for limit conditions then *$\alpha t << 1$ or $\alpha t >> 1$* correspondingly. The values of α and γ are presented in table 1. For example for CdS films $\alpha=4,5\cdot10^{-3}$ c^{-1}, $\gamma=0,14$ (T = 86K) [7].

Table 1. α and γ values for selected samples.

## of samples	α, c^{-1}	γ
6	$1,76\cdot10^{-2}$	$1,13\cdot10^{-1}$
12	$6,5\cdot10^{-3}$	$5,5\cdot10^{-2}$
16	$1,17\cdot10^{-2}$	$3,5\cdot10^{-2}$

The difference in γ values (γ represents the ratio between the width of the depletion layer at the drift barrier and that of the depletion layer at the recombination barrier) might be explained on the base of the quality of the $Cd_{3-x}Zn_xAs_2$ crystals, which depends on the technology of crystal's growth. Knowing the lifetime of support of charge in $Cd_{3-x}Zn_xAs_2$ ($x\approx1.8$), $\tau_o=5\cdot10^{-3}$, it is possible to estimate the height of the recombination barriers.

Assuming $\tau= 10$ hours, at T=80 K from $\tau = \tau_o \epsilon^{\varphi/KT}$ we have $\varphi\approx0.1$ electronvolt and it seems to be balanced. In the estimation of the height of the dark drift barrier according to the multiply of RC, we have calculated the value of $\varphi_{ST}=3\cdot10^{-3}$ electronvolt which is significantly less than the value of $\varphi_{ST}=0.2$ electronvolt for CdS films [7]. It should be mentioned, however that our estimates were obtained for rather thick $Cd_{3-x}Zn_xAs_2$ crystals.

To summarize we should point out the fact that the research of LRP and RC in $Cd_{3-x}Zn_xAs_2$ crystals might be continued to improve our understanding of this interesting phenomenon.

References

[1] V. Zhdanovich Structure and characteristics of $A^{II}B^{IV}$ compounds //Physics and Chemistry of Solids.
[2] E.K. Arushanov Prog. Cryst. Growth Char&ct. 3., p.211. 1980.
[3] R.J. Wagner, E.O. Palic, J.W. Swiggard // J. Phys. Chem Sol. (Suppl). 32, p.471. 1971.
[4] E.K. Arushanov, A.F. Kniazev, A.N. Nartepov //PhTP. 18, Iss. 7. pp. 1202- 1204. 1983.
[5] A.F. Kniazev, A.N. Nartepov // Bulletin of Academy of Science of Moldova, #3, pp 42-44, 1993.
[6] M.K. Sheikman, A.Ya. Shick // PhTP. Iss. 10, p.209, 1976.
[7] V.B. Sandamirskiy, A.G. Zhdan, M.A. Messerer, I.B. Guliaev // PhTP. Iss. 7, p.1314, 1973.

PHOTOLUMINESCENCE OF n-ZnSe SINGLE CRYSTALS DOPED WITH IODINE BY VAPOUR PHASE DIFFUSION

A.N. Avdonin, G.N. Ivanova, D.D. Nedeoglo, N.D. Nedeoglo and V.P. Sirkeli

Department of Physics, Moldova State University, A. Mateevich str. 60, MD-2009, Chisinau, Republic of Moldova
Tel: +373 22 577586; Fax: +373 22 244248; e-mail: nedeoglo@usm.md

Photoluminescence spectra of n-ZnSe single crystals doped with iodine are investigated in the temperature range from 83 to 300 K. It is shown that the edge PL band is formed by overlapping of the PL lines attributed to I_{Se} donor-bound ecxitons (I_2^I) and V_{Zn} acceptor-bound excitons (I_1^D). A model of radiation mechanisms, which explain the redistribution of the edge and long-wave PL bands intensities with increasing doping level of the samples, is proposed.

1. Introduction

Due to the large band gap energy ($E_g \sim 2.7$ eV at 300 K), zinc selenide is a perspective material for visible light-emitting diodes, especially for the diodes operating in the blue region of the spectrum. The necessity of obtaining high-intensive radiation requires good electrical and optical parameters of the crystals. These parameters depend on the type and quantity of the doping impurity, its aptitude to self-compensation and formation of complexes with native defects.

It was considered for a long time that the group III elements, such as Al, Ga, In, were good donor impurities for zinc selenide. However, it was shown later that these impurities were unsuitable for obtaining of heavily doped n-type ZnSe crystals as the probability of formation of associative acceptors, which consist of both native and doping impurity defects, rapidly increases with increasing dopant concentration [1]. The influence of Al and Cl impurities on radiative properties of ZnSe epitaxial films was analyzed in work [2]. It was shown the superiority of group VII elements over group III elements as donor dopants. The doping of n-ZnSe epitaxial films with Cl [3] and I [4] allowed the doping leve increasing up to 10^{19} cm^{-3} and $3 \cdot 10^{19}$ cm^{-3}, respectively.

The influence of ZnI_2 vapour pressure on luminescence properties of n-ZnSe single crystals is investigated in the present paper. The choice of ZnI_2 vapour as a medium of diffusion doping is caused by the fact that such a doping reduces the number of V_{Zn} native defects, which compensate donor impurity, and promotes incorporation of iodine atoms into Se sublattice vacancy sites.

2. Experimental Results and Discussion

Photoluminescence (PL) spectra of iodine-doped n-ZnSe single crystals were investigated in the temperature range from 83 to 300 K. The doping was made during a long-term (100 h) high-temperature (950 ºC) thermal treatment of n-ZnSe single crystals in ZnI_2 vapour. The doping level was varied by changing vapour pressure in quartz ampoules with the samples (the ampoules were previously evacuated to the pressure of $\sim 10^{-4}$ torr). For this
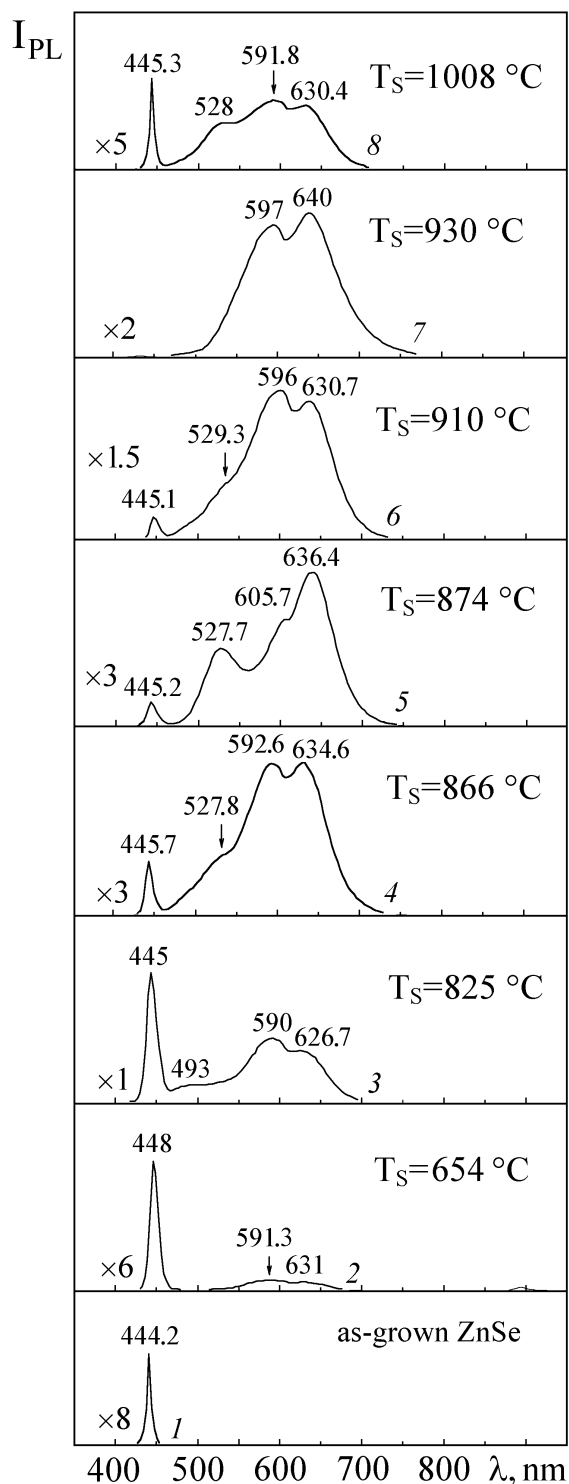
Fig. 1. PL spectra of n-ZnSe crystals annealed in ZnI_2 vapour at different temperatures of ZnI_2 vapour source. T = 83K.

purpose, the temperature of ZnI_2 vapour source was varied from 654 to 1008 °C. After termination of the annealing, the ampoules were rapidly cooled down. Luminescence was excited by radiation of ILGI-503 nitrogen impulse laser with 337.1 nm wavelength (3.675 eV). A MDR-23 monochromator with reciprocal dispersion of 1.4 nm/mm was used.

The PL spectrum for the original n-ZnSe crystal contains one narrow (21 meV) band of excitonic radiation with a maximum at 444.2 nm (2.789 eV) (Fig. 1, curve 1). There are no other bands in the region from 500 to 800 nm. The annealing of the crystals in ZnI_2 vapour leads to a broadening of the edge PL band (3 ÷ 4 times as large) and to its shift towards long wavelengths. Overlapping wide bands of long-wave luminescence also appear after such a treatment. For instance, the PL spectrum for the n-ZnSe crystal annealed in ZnI_2 vapour at T_S = 654 °C contains wide bands with maxima at 591.3 nm (2.095 eV) and 631 nm (1.964 eV). The edge PL band is broadened ($W_{1/2}$ ~ 71 meV) and shifted towards 448 nm (2,765 eV).

The structure of PL spectra is practically unchanged with increasing temperature of ZnI_2 vapour source (Fig. 1, curves 2-8). The half-width of the edge band increases to $W_{1/2}$ = 85 meV at T_S = 866 °C, its intensity decreases (Fig. 2, a), and spectral maximum position shifts towards short wavelengths (Fig. 2, b). The further increase of the source temperature leads to a rapid decrease of the half-width and localization of the band at 445 nm (2.784 eV) (Fig. 2, a, b).

Fig. 1 shows that the decrease of the edge PL band intensity is accompanied by an increase of the long-wave PL intensity. As the source temperature T_S increases to 910 °C, the intensity ratio between the edge and long-wave (λ_{max} = (590 ÷ 596) nm) PL bands decreases. At T_S = 930 °C, the edge PL band disappears and the spectrum contains only the double-peaked band of long-wave luminescence (Fig.1, curve 7). The increase of the source temperature to 1008 °C leads again to an increase of the edge PL band intensity (Fig. 1,
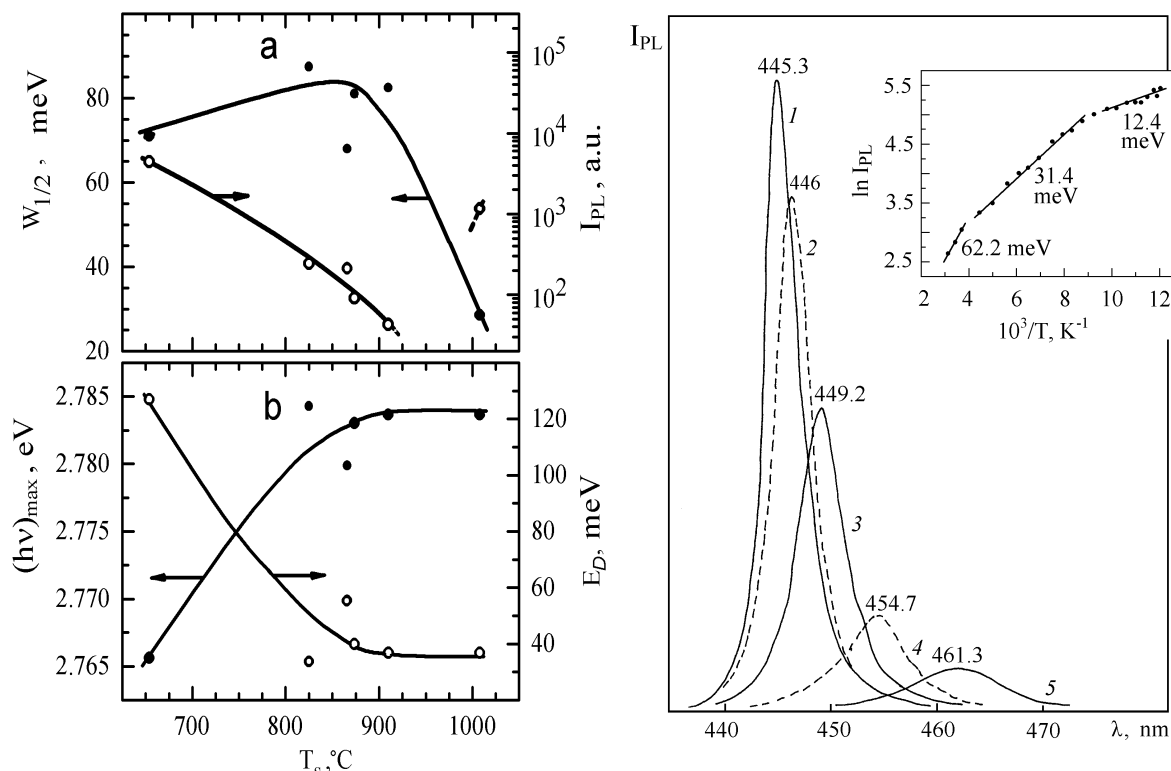
Fig. 2. Half-width and intensity (a), spectral position and donor ionization energy (b) for the excitonic PL band versus ZnI_2 vapour source temperature.

Fig. 3. Temperature evolution of the edge PL spectra for the n-ZnSe:I crystal annealed at $T_S = 1008$ °C.
T, K: 1–85, 2–94, 3–134, 4–200, 5–319.
Inset: Temperature quenching of the edge PL band intensity.

curve 8). It becomes narrower (Fig. 2, a) and is now dominant in the spectrum.

The temperature evolution of the edge PL spectra for the n-ZnSe:I crystal annealed at $T_S = 1008$ °C is given in Fig. 3. As temperature increases, the edge PL intensity decreases, the band broadens and shifts towards long wavelengths.

Fig. 4 shows the temperature dependence of free exciton band position (curve 1) calculated for n-ZnSe crystal using the formula [5]:

$$E_x(T) = 2.804 - 8.59 \cdot 10^{-4} \frac{T^2}{T + 405} \text{ (eV)},$$

where $E_g = 2.804$ eV is the band gap energy at $T = 83$ K, $\dfrac{dE_g}{dT} = 8.59 \cdot 10^{-4}$ eV/K is the temperature coefficient of ZnSe band gap energy changing, $\theta_D = 405$ K is the Debye temperature for ZnSe. The temperature dependence of the edge PL band position determined experimentally for the sample annealed in ZnI_2 vapour at $T_S = 1008$ °C is also presented in Fig. 4 (curve 2). It is seen that the maximum of the edge PL band for the n-ZnSe:I crystal is localized at long wavelengths in comparison with the free exciton band. As temperature increases, the position of the edge PL band maximum approaches the calculated value for the free exciton band, and these two values coincide near room temperature.

Characteristic features of the edge PL band are its localization in the region of wavelengths, which correspond to excitonic luminescence, and a great value of its half-width

($W_{1/2} \sim 70\div85$ meV). We think that such a great half-width is caused by overlapping of the PL lines attributed to I_{Se} donor-bound excitons (I_2^I) and V_{Zn} acceptor-bound excitons (I_1^D).The fact that the activation energy of the edge PL intensity temperature quenching has two values for all the I-doped samples in the temperature range from 83 to 240 K [6] (Fig. 3, inset) is the evidence of excitonic nature of this PL band. If this band had been attributed to radiative recombination of electrons localized on I_{Se} donors with holes from the valence band, the temperature quenching activation energy would have had only one value, equal to E_D (I_{Se}).
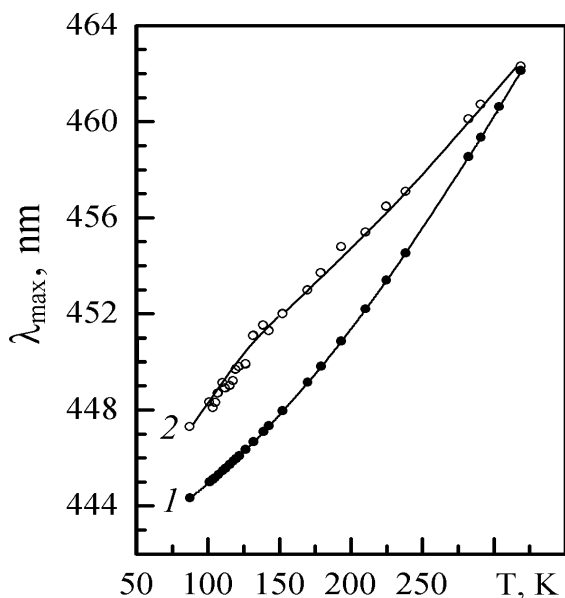

Fig. 4. The edge PL band position versus temperature for n-ZnSe:I crystal, T_S=1008 °C. 1 – calculated curve for free excitons, 2 – experimental curve.

3. Conclusion

The redistribution of the edge and long-wave PL bands intensities with increasing doping level of the samples (Fig. 1) is well described in the limits of the proposed model of radiation mechanisms for these PL bands. As the temperature of ZnI_2 vapour source increases, the iodine vapour pressure in ampoules with the samples increases too. The rising concentration of I_{Se} defects results in increasing probability of (V_{Zn}-I_{Se}) associative acceptor formation and increasing intensity of long-wave luminescence. The probability of simple I_{Se} and V_{Zn} defect formation decreases, and as they are responsible for the edge PL band, its intensity decreases down to complete disappearance in the spectrum for the crystal annealed at T_S = 930 °C (Fig. 1, curve 7). However, as it was mentioned above, a very intensive narrow band with a maximum at 445.3 nm (2.782 eV) dominates in the spectrum for the sample annealed at higher vapour source temperature T_S = 1008 °C (Fig. 1, curve 8).

We suppose that in heavily doped crystals (T_S = 1008 °C), iodine atoms effectively occupy selenium vacancies and promote the generation of native (V_{Zn}) and impurity (I_{Se}) defects. A number of I_{Se} impurity defects take part in the formation of donor-bound excitons, which are responsible for the edge PL band localized at 445.3 nm, the rest of them form (V_{Zn}-I_{Se}) associative acceptors, which are responsible for the long-wave wide PL band.

References
[1] V.Z. Bolboshenko, D.D. Nedeoglo, Phys. Tekh. Poluprov. 21, 1247 (1987) (in Russian).
[2] A. Kamata, T. Uemoto, M. Okajima, K. Hirahara, M. Kawachi, T. Beppu, J. Cryst. Growth 86, 285 (1988).
[3] A. Kamata, K. Hirahara, M. Kawachi, T. Beppu, Abstracts of the 17th Conf. on Solid State Devices in Materials, Tokyo, p. 233 (1985).
[4] N. Shibata, A. Ohki, A. Katsui, J. Cryst. Growth 93, 703 (1988).
[5] Y. Shirakava, H. Kukimoto, J. Appl. Phys. 51, 2014 (1979).
[6] A.N. Avdonin, G.N. Ivanova, D.D. Nedeoglo, N.D. Nedeoglo, J. Appl. Spectroscopy 69, 244 (2002) (http://imaph.bas-net.by/JAS).

FERROELECTRIC PHASE TRANSITION AND IMPURITY-LATTICE CORRELATIONS IN $Pb_{1-X}Ge_XTe(Ga)$

B.A. Akimov, D.R. Khokhlov, V.V. Pryadun, L.I. Ryabova

Physics Department, Moscow State University, Moscow, 119992, Russia

The impedance of single-crystal samples of PbTe(Ga) and $Pb_{1-X}Ge_XTe(Ga)$ ($0 \leq x \leq 0.095$) is investigated in the frequency range from 10^2 to 10^6 Hz and temperature range 4.2–300 K. The temperature dependence of the capacitance of all the $Pb_{1-X}Ge_XTe(Ga)$ samples studied exhibited two types of features. These are a pronounced peak at a temperature $T \sim T_{ph}$, caused by a dielectric anomaly at the ferroelectric phase transition, and strong frequency dependent increase of the capacitance in the temperature region $T < 100$ K. The ferroelectric phase transition temperature for all the samples is found to be significantly higher than the characteristic temperatures of the long term relaxation process appearance. Thus these phenomena seem not to be correlated directly. The low temperature behavior of the capacitance may be caused by recharge processes in the impurity system accompanied by local reconstruction of the impurity center surrounding.

1. Introduction

The impurities characterized by mixed valence (In, Ga, Cr, Yb and some others) generate in lead telluride based solid solutions a system of deep energy levels, their position depending on the composition of the solution and the kind of a dopant. The Fermi level pinning, persistent photoconductivity at low temperatures, specific view of current-voltage characteristics, nonexponential relaxation of nonequilibrium carriers, unusual magnetic properties may be regarded as characteristic features of such doped solutions.

Most of the models developed to describe the impurity behavior consider the strong correlation of the impurity charge state and local distortion of the lattice nearby the impurity center [1]. Nevertheless the conception of ferroelectric phase transition induced by the doping was not still disproved by direct experiment.

$Pb_{1-X}Ge_XTe(Ga)$ single crystals seem to be the mostly suitable object for such kind of investigation. Their electrophysical and photoelectric characteristics have been studied in detail [2-6]. The phase transition temperature T_{ph} in undoped $Pb_{1-X}Ge_XTe(Ga)$ is well known [7,8]. Doping with Ga leads to significant resistance growth due to the Fermi level pinning within the energy gap and persistent photoconductivity appearance at $T \leq T_C \approx 80$ K. Thus the opportunity to measure the impedance indicating the dielectric permittivity behavior for single crystal samples without specially prepared p-n junction appears.

2. Samples and Experimental Technique

Single-crystal samples of $Pb_{1-X}Ge_XTe(Ga)$ ($0 \leq x \leq 0.095$) were obtained by sublimation from the vapor phase. An impurity of 1.5 mol. % GaTe was introduced directly into the growing melt. The composition of the samples was determined by the X-ray diffraction method. The values of the lattice constant are presented in the Table. The samples intended for impedance measurements were in the form of rectangular slabs with an area of ~ 4 x 4 mm and thickness ~ 1 mm. The surface of the slabs was coated by a 95%In+4%Ag+1%Au alloy.

For the measurements the samples were placed in a chamber that shielded them from background radiation.

Table. Characteristics of the investigated samples

N	Lattice constant a, A	X	T_{ph}, К (liter.)	T_{ph}, К (exper)	Energy gap E_g, meV	E_A, meV
1	6,4642	0	-	-	190	55
2	6,4426	0.046	136	140	265	75
2	6,4260	0.08	196	165	297	140
4	6,4196	0.095	224	190	313	150

The measurements were made with E7-12 and MIT 9216A ac current bridges at frequencies f from 10^2 to 10^6 Hz in the temperature interval 4.2–300 K. The temperature dependence of the resistivity ρ was measured in dc on samples 1x1x5 mm in size in darkness and under illumination by IR radiation sources.

3. Experimental Results

The typical view of the temperature curves of the resistivity ρ measured in darkness and under illumination of a lightemitting diode at wavelength $\lambda = 1$ μm is shown in Fig.1 for the $Pb_{1-X}Ge_XTe(Ga)$ sample with $x = 0.046$. Similar curves had been observed previously for solid solutions of various compositions [2–6]. The characteristic feature distinguishing the $\rho(T)$ curve for $Pb_{1-X}Ge_XTe(Ga)$ from that for PbTe(Ga) is the presence of a maximum followed by rapid drop of the ρ value at cooling even for the curve taken in darkness. In lead telluride containing gallium $\rho(T)$ increases monotonically with decreasing temperature all the way down the lowest temperatures of the experiment. Persistent photoconductivity is
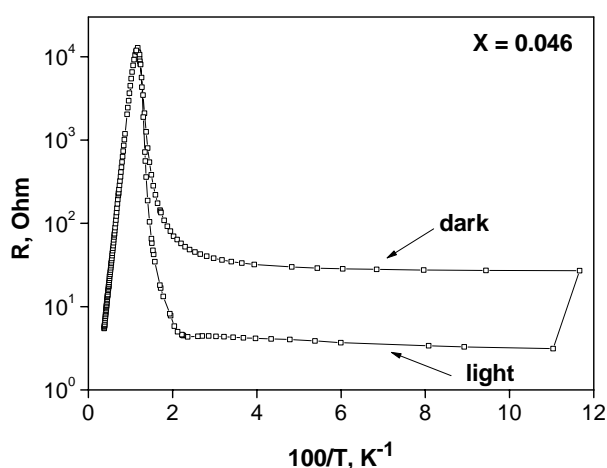

Fig.1. Temperature dependence of the resistance R for $Pb_{1-X}Ge_XTe(Ga)$ sample ($x = 0.046$) in darkness and under illumination.

observed at $T<T_C = 80$ K, where T_C is independent of the composition x of the solid solution. In Refs. [2] and [4–6] a correlation was noted between the composition x of the solid solution and the temperature T_m corresponding to the maximum on the $\rho(T)$ curves obtained under conditions of shielding. This suggested that the maximum is due to a phase transition [4–6] the temperature of which is shifted by approximately 80 K downward on the temperature scale because of the presence of the dopant. However, the possibility of such a substantial change in phase transition temperature for such an insignificant impurity concentration has raised valid objections [2,3]. In the high-temperature region the $\rho(T)$ curves for all the samples studied exhibited a segment corresponding to an activational character of the conductivity. The activation energies E_A calculated from the relation $\rho \sim \exp(E_A /kT)$ are given in the Table. It should be noted that the values of the activation energy obtained previously [2-6] are practically equal to the data of the present study and do not depend on the shape and size of the sample. At frequencies below 10^5 Hz the real part of the impedance Z' is practically equal to ρ. At a frequency of 10^6 Hz the value of Z' in the peak region is somewhat lower. An example of the typical temperature dependence of the capacitance C for the $Pb_{1-X}Ge_XTe(Ga)$ ($x = 0.095$) sample measured at different frequencies is shown in Fig. 2. Since the crystals studied were not completely isolated, especially in the high-temperature region, in the processing of the experimental data the capacitance of the crystals was calculated from the values of the real Z' and imaginary Z'' parts of the impedance in the approximation of an equivalent circuit in the form of a parallel R-C circuit. As is seen in Fig.2, for $T = T_{ph}$ the $C(T)$ curves clearly exhibit a peak with a position that is practically
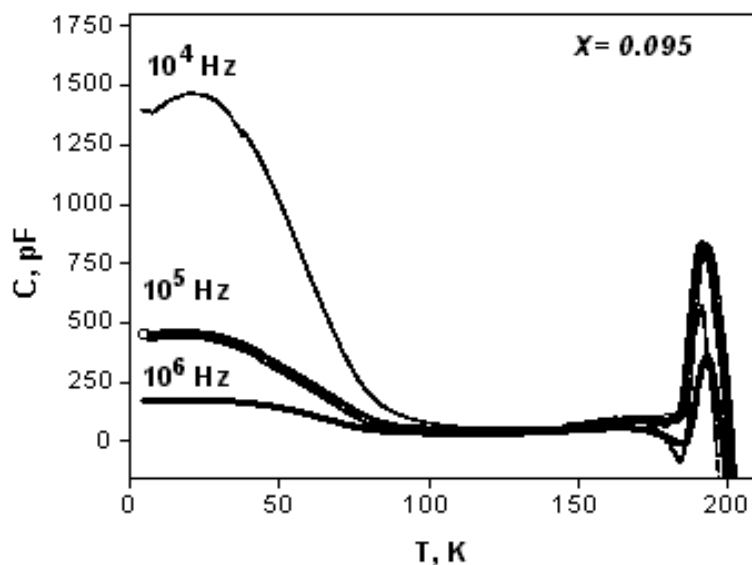

Fig.2. Temperature dependence of the capacitance for $Pb_{1-X}Ge_XTe(Ga)$ ($x = 0.095$). The reference signal frequency is shown at the curves.

independent of frequency. The Table also gives the values of the phase transition temperature for undoped $Pb_{1-X}Ge_XTe(Ga)$ crystals, according to published data (T_{ph} liter.) and according to the experimental data of the present study (T_{ph} exper.). The temperature at which the peak is observed on the $C(T)$ curve is somewhat lower than the temperature of the transition from the cubic to the rhombohedral phase for the undoped alloy of the same composition but is substantially higher than the temperature of the maximum on the $\rho(T)$ curves. It should be

noted that the lowering of the phase transition temperature by an amount that is quite comparable with the data of the present study has also been observed upon doping of $Pb_{1-X}Ge_XTe(Ga)$ alloys with indium [8].It is important that the peak on the $C(T)$ curves is rather sharp, indicating good homogeneity of the samples in respect to composition. In the temperature region $T < T_{cap}$ (T_{cap} is the temperature at which low-frequency anomalies appear) a strong frequency dependence of the capacitance is observed. At low frequencies ($f\sim10^3$ Hz) one observes a sharp increase in the capacitance by almost an order of magnitude. With increasing f the amplitude of the jump decreases, and at $f \sim 10^5$ Hz the $C(T)$ curve becomes rather smooth. In the temperature region $T < 70$ K the capacitance of PbTe(Ga) single crystals is practically independent of both temperature and the frequency f (see Fig. 3).
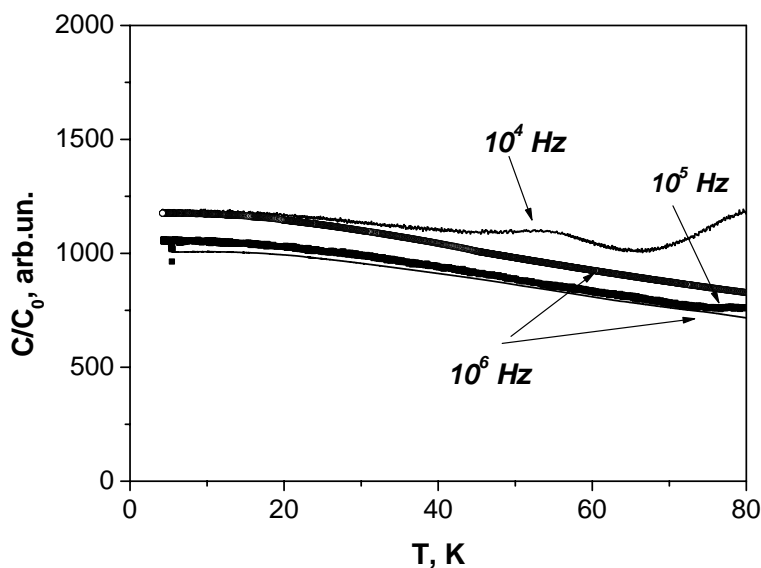

Fig.3. Temperature dependence of the capacitance of PbTe(Ga) samples in relative units (C_0 is the capacitance of the vacuum condenser of the same configuration). The reference signal frequency is shown at the curves. Two curves corresponding to the same frequency of 10^6 Hz are measured for samples with different shape and, consequently, C_0 values.

Figure 4 shows the temperature dependence of the ratio C/C_0 for $Pb_{1-X}Ge_XTe(Ga)$ samples of various composition (C_0 is the geometric capacitance, defined as the ratio of the area of the contacts on the sample to the distance between them). If it is assumed that the sample is a flat capacitor, then the value of C/C_0 corresponds to the permittivity ε. For all the $Pb_{1-X}Ge_XTe(Ga)$ samples studied we find ε ~ 1300 in the temperature interval $T_{cap} < T < T_{ph}$ for all $f < 10^5$ Hz and in the interval 4.2 K $< T < T_{ph}$ for $f > 10^5$ Hz. The additional contribution to the capacitance observed in $Pb_{1-X}Ge_XTe(Ga)$ in the low-frequency range for $T < T_{cap}$ cannot be attributed to processes due to polarization or resonance effects of the crystal lattice itself. The characteristic frequencies of such effects are many orders of magnitude higher than 10^6 Hz. The most probable cause of the increase in capacitance may be processes involving charge exchange between impurity centers. An analogous effect in the same frequency range has been observed previously in the heterojunctions of germanium-silicon diodes and was explained as being the contribution to the capacitance of the heterojunction from charge exchange between boundary states [9].
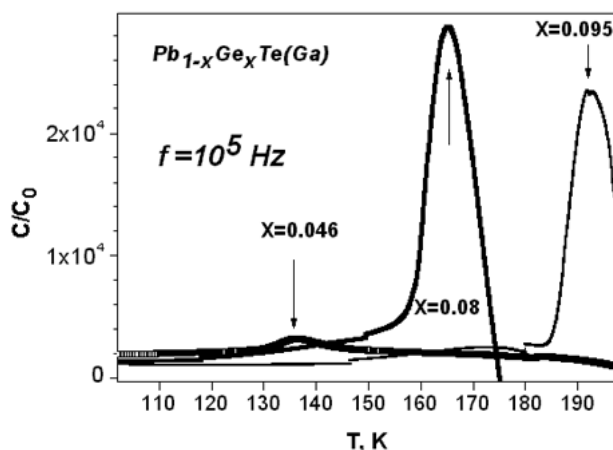
Fig.4. Temperature dependence of the capacitance of $Pb_{1-X}Ge_XTe(Ga)$ samples in relative units. The reference signal frequency is 10^5 Hz. Composition of the solid solutions x is shown at the curves.

4. Conclusion

In this study we have established experimentally that the phase transition temperature T_{ph} in $Pb_{1-X}Ge_XTe(Ga)$ is substantially higher than the characteristic temperatures for the appearance of persistent photoconductivity ($T_C \sim 80$ K), the temperatures of the maximum on the $\rho(T)$ curves T_m, and the temperatures at which the low-frequency anomalies appear on the temperature curves of the capacitance (T_{cap}). The data show that processes involving charge exchange between impurities are characterized by only a local reconstruction of the lattice, unaccompanied by the frequency-independent dielectric anomalies observed at transitions to the ferrophase.

References

[1] B.A. Volkov, L.I. Ryabova, and D.R. Khokhlov, Usp. Fiz. Nauk 172, 875 (2002).
[2] B.A. Akimov, A.V. Albul, I.I. Ivanchik, L.I. Ryabova, E.I. Slyn'ko, and D.R. Khokhlov, Fiz. Tekh. Poluprovodn. 27, 355 (1993). (Semiconductors 27, 194 (1993)).
[3] B.A. Akimov, V.V. Pryadun, L.I. Ryabova, and D.R. Khokhlov, Fiz.Tekh. Poluprovodn. 38, 293 (2004) (Semiconductors 38, 281 (2004)).
[4] E.P. Skipetrov, E.A. Zvereva, L.A. Skipetrova, V.V. Belousov, and A.M. Musaitin, J. Cryst. Growth 210, 292 (2000).
[5] E.P. Skipetrov, E.A. Zvereva, V.V. Belousov, L.A. Skipetrova, and E.I. Slynko, Phys. Status Solidi B 221, 549 (2000).
[6] E.P. Skipetrov, E.A. Zvereva, O.S. Volkova, E.I. Slynko, and A.M. Musaitin, Mater. Sci. Eng., B 91–92, 416 (2002).
[7] S. Nishi, H. Kawamura, and K. Murase, Phys. Status Solidi B 97, 581 (1980).
[8] A.I. Lebedev and Kh.A. Abdullin, Fiz. Tekh. Poluprovodn. 18, 624 (1984) (Sov. Phys. Semicond. 18, 388 (1984)).
[9] J.P. Donnelly and A.G. Milnes, IEEE Trans. Electron Devices ED-14, 63 (1967).

DEEP GALLIUM-INDUCED DEFECT STATES IN Pb$_{1-x}$Sn$_x$Te

E.P. Skipetrov[1], E.A. Zvereva[1], N.N. Dmitriev[1], A.V. Golubev[2], V.E. Slyn'ko[3]

[1]Physics Faculty, Moscow State University, 119992 Moscow, Russia
Tel: +7 (095)939 44 93, Fax: +7(095)932 88 76, email: skip@mig.phys.msu.ru
[2]Faculty of Material Science, Moscow State University, 119992 Moscow, Russia
[3]Institute of Material Science Problems, 274001 Chernovtsy, Ukraine

The galvanomagnetic effects in Pb$_{1-x}$Sn$_x$Te: Ga under variation of alloy composition were investigated. It was found for samples with tin content x≤0.06 the temperature dependences of resistivity and the Hall coefficient have a low temperature activation range of impurity ionization, while for samples with 0.09≤x≤0.21 they have a "metallic" character. The results were discussed assuming an appearance of two different deep impurity levels E_{Ga1} and E_{Ga} stabilizing the Fermi level in the energy spectrum. The activation energy for "insulating" samples as well as the Fermi level position for "metallic" samples were determined and used to build the energy level diagram.

1. Introduction

For a long time numerous studies of gallium impurity behavior in lead telluride based alloys did not yield any full unambiguous interpretation of its doping action due to a number of non-trivial effects observed [1, 2]. In particular it was incomprehensible how gallium-induced deep level revealed in the gap in PbTe: Ga changes its energy position in lead telluride based alloys. There was no reliable explanation of the mechanism of the Fermi level pinning by impurity level. It was also reported an existence of at least two ranges of the Fermi level pinning on the electron concentration versus gallium content dependence and drawn a hypothesis assuming the appearance of two different Ga-induced states in PbTe-based alloys [3-5]. Only recent studies performed on the Pb$_{1-x}$Ge$_x$Te: Ga alloys cleared up some of the peculiarities of the Fermi level pinning in gallium-doped materials [5, 6]. A model has been proposed according to which doping with gallium leads to the appearance of two different defect levels in the energy spectrum of alloys situated in the gap and on the background of the conduction band depending on the alloy composition and impurity concentration. At the same time we are still lacking of information about the energy position of these impurity levels in other PbTe based alloys.

In this article we report the results of our measurements of the galvanomagnetic effects in the Pb$_{1-x}$Sn$_x$Te: Ga alloys for various alloy composition. The main aims are to reveal gallium-induced defect states stabilizing the Fermi level in the energy spectrum of alloys and to construct the energy level diagram as a function of alloy composition. The variation of tin concentration over the wide range (0≤x≤0.21) was expected to alter the position of the impurity-induced levels relative to the principal band edges and to shift the Fermi level stabilization range from the energy gap to the conduction band.

2. Experimental Details

Single crystals of n-Pb$_{1-x}$Sn$_x$Te:Ga ($0 \leq x \leq 0.06$, C_{Ga}=0.3–0.7 mol. %) were synthesized from the vapor phase by sublimation and n-Pb$_{1-x}$Sn$_x$Te:Ga ($0.09 \leq x \leq 0.21$, C_{Ga}=0.2–2.2 mol. %) were grown by a modified Bridgman method. The tin ratio and impurity concentration in doped samples were determined from the initial amount of substance in the furnace charge, taking into

Table 1. Parameters of the n-Pb$_{1-x}$Sn$_x$Te:Ga samples used in this study at T=4.2 K.

Sample	x	C_{Ga} (mol%)	ρ ($\Omega \cdot$cm)	$|R_H|$ (cm^3/C)	μ_H (cm^2/V$\cdot$s)	n (cm^{-3})
Sn-0-3	0	0.5	2.4×10^4	$<4.2 \times 10^3$	$<1.8 \times 10^{-1}$	$<1.5 \times 10^{15}$
Sn-0-4	0	0.7	5.7×10^5	$<1.0 \times 10^5$	$<1.8 \times 10^{-1}$	$<6.3 \times 10^{13}$
Sn-6	0.06	0.5	3.3×10^5	$<1.8 \times 10^5$	$<5.5 \times 10^{-1}$	$<3.5 \times 10^{13}$
Sn-9	0.09	0.2	1.3×10^{-4}	9.7×10^{-1}	7.8×10^3	6.5×10^{18}
Sn-10	0.10	0.3	1.4×10^{-4}	9.0×10^{-1}	6.5×10^3	7.0×10^{18}
Sn-11	0.11	0.9	1.4×10^{-4}	9.4×10^{-1}	6.8×10^3	6.9×10^{18}
Sn-14	0.14	0.5	1.6×10^{-4}	8.0×10^{-1}	5.1×10^3	7.9×10^{18}
Sn-16	0.16	0.3	2.7×10^{-4}	5.2×10^{-1}	4.3×10^3	1.2×10^{19}
Sn-18	0.18	0.7	1.1×10^{-4}	4.1×10^{-1}	3.9×10^3	1.6×10^{19}
Sn-21	0.21	2.2	1.5×10^{-4}	2.7×10^{-1}	1.7×10^3	2.3×10^{19}

account the distribution of impurity along the ingot during the growth process according to the exponential law of impurity distribution in A^{4}B^6 solid solutions established in [7] and controlled by the energy dispersive X-ray fluorescence analysis. For each sample the temperature dependences of the resistivity ρ and Hall coefficient R_H ($B \leq 0.1$ T, $4.2 \leq T \leq 300$ K) were measured by four-probe technique. Table 1 summarizes the main parameters of the samples at T=4.2 K.

3. Galvanomagnetic Effects

The measurements performed for the samples with low tin content ($x \leq 0.06$) have shown that the temperature dependences of the resistivity ρ (Fig. 1a) and the Hall coefficient R_H have a low temperature activation range of the impurity ionization, indicating an existence of the deep gallium-induced level E_{Ga1}, which stabilizes the Fermi level in the forbidden band of the alloys. The temperature dependences of ρ (Fig. 1b) and R_H for the samples with tin content $0.09 \leq x \leq 0.21$ have a "metallic" character. However, the Hall coefficient is changed in anomalous manner: an absolute value of R_H increases by more than two times with increasing temperature. This behavior is thought to be associated with an existence of gallium-induced resonant level E_{Ga}, stabilizing the Fermi level on the background of the conduction band. The similar character of the R_H variation with temperature has been observed earlier for indium-doped PbTe alloys when the indium level was resonant with the conduction band [1, 8]. As the tin concentration in the alloys increases activation energy of deep gallium level ΔE_{Ga1} for the "insulating" samples decreases and free electron concentration for the "metallic" samples monotonously increases.
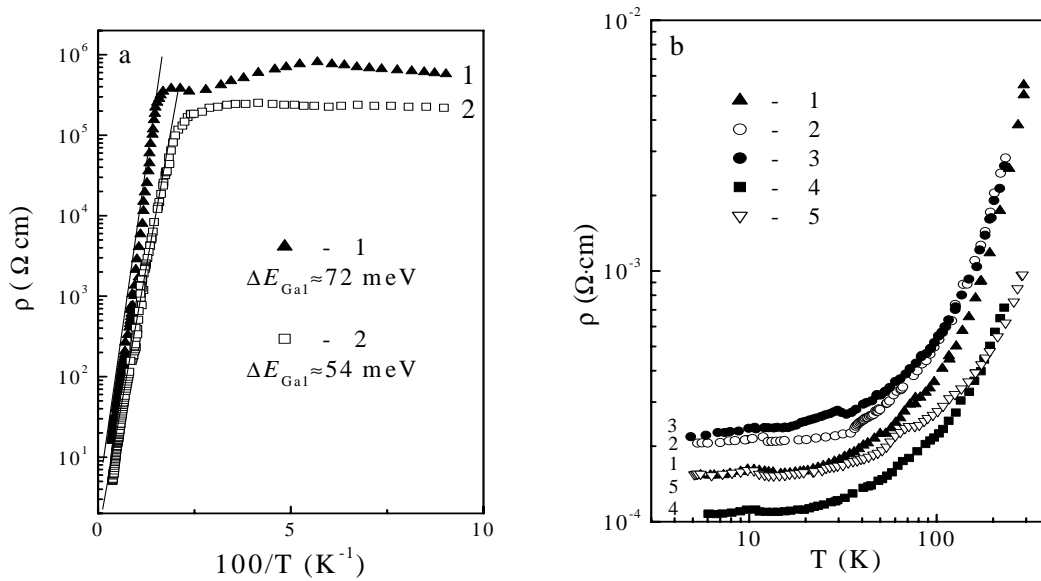
Fig. 1. Temperature dependences of the resistivity in the $Pb_{1-x}Sn_xTe$: Ga alloys upon varying tin content x: (a) 1 - 0; 2 - 0.06; (b) 1 - 0.10; 2 - 0.11; 3 - 0.14; 4 - 0.18; 5 - 0.21.
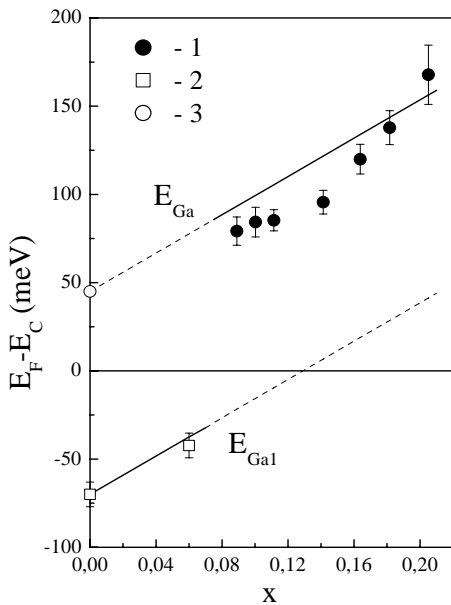

Fig. 2. Dependence of the Fermi level position in $Pb_{1-x}Sn_xTe$:Ga on the alloy composition.

1, 2 – results of the present work,

3 – an extrapolation of the data obtained for $Pb_{1-x}Ge_xTe$:Ga [5].

4. Determination of Activation Energy and Fermi Level Position

From the slope of the activation range on the $\rho(1/T)$ dependences in accordance with relation $\rho \propto \exp(\Delta E_{Ga1}/kT)$ we have determined an activation energy of gallium-induced level ΔE_{Ga1} for the alloys being in insulating state (x≤0.06). It was found that with increasing tin content in the alloys the activation energy of impurity level decreases. Its rate estimated from the slope of the $\Delta E_{Ga1}(x)$ dependence practically coincides with an average rate of the energy gap decreasing in the alloys under study [9] and is $d\Delta E_{Ga1}/dx \approx -5$ meV/mol.%, that means that the gallium level E_{Ga1} moves almost parallel to the valence band top.

Using the values of the Hall coefficient at helium temperature for the samples with higher tin content (in metallic phase) we have calculated the dependences of the free electron concentration and the Fermi level position E_F upon alloy composition in the frame of two-band dispersion law for A^4B^6 semiconductors [10, 11]:

$$\left(\frac{E_g}{2} - E\right) \cdot \left(-\frac{E_g}{2} - E\right) = E_\perp \cdot \frac{p_\perp^2}{2m_0} + E_\parallel \cdot \frac{p_\parallel^2}{2m_0} \quad (1)$$

where E_g is the energy gap, $p_\perp$ and $p_\parallel$ are transversal and longitudinal components of the quasi-impulse relative to the <111> axis, respectively, $E_\perp$ and $E_\parallel$ are the parameters characterizing an interaction between the valence and conduction bands ($E_\perp \approx 7.65$ eV and $E_\parallel \approx 0.73$ eV for $Pb_{1-x}Sn_xTe(x\approx0.2)$ [12]).

The concentration of the free electrons n was calculated using the following expressions:

$$n = 2 \cdot 4 \cdot V_{el} / (2\pi\hbar)^3 \quad (2)$$

$$V_{el} = \frac{4}{3}\pi p_\perp^2(E_F)p_\parallel(E_F) \quad (3)$$

where V_{el} is a volume of the Fermi surface ellipsoid in the p-space.

Then the Fermi energy was determined from the dispersion law (1):

$$E_F = \sqrt{\left(\frac{3}{4} \cdot \frac{n\pi^2\hbar^3 E_\perp\sqrt{E_\parallel}}{(2m_0)^{3/2}}\right)^{2/3} + \frac{E_g^2}{4}} \quad (4)$$

The Fermi level movement relative to the conduction band edge at the L-point of the Brillouin zone under variation of tin content in the alloys, calculated according to (4), is presented in Fig. 2. The Fermi energy value increases almost linearly with increasing tin concentration in the alloys. Solid lines in this figure represent the theoretical curves corresponding to the parallel movement of impurity levels E_{Ga} and E_{Ga1} relative to the valence band top L_6^+. One can see that the experimental dependences of the Fermi level position on tin content are in a good agreement with theoretical lines showing the impurity level movement on the energy scale.

5. Conclusion

The results obtained allow us to conclude that like in $Pb_{1-x}Ge_xTe$: Ga earlier investigated [5,6], doping of $Pb_{1-x}Sn_xTe$ with gallium leads to an appearance of two different impurity levels in the energy spectrum of the alloys: level E_{Ga1}, responsible for the Fermi level pinning in the gap for alloys in the insulating state, and resonant level E_{Ga}, stabilizing the Fermi level in the conduction band for alloys in the metallic state. The energy level diagram for $Pb_{1-x}Sn_xTe$: Ga alloys as a function of matrix composition was proposed and revealed that with increasing tin content in the alloy both levels move relative to the bottom of conduction band L_6^- with the rate approximately 5 meV/mol.%, while the energy position of the gallium levels relative to the valence band top L_6^+ remains practically unchanged.

References

[1] V.I. Kaidanov and Yu.I. Ravich, Sov. Phys. Usp. 28, 31 (1985).

[2] B.A. Volkov, L.I. Ryabova, D.R. Khokhlov, Physics-Uspekhi 45, 819 (2002).

[3] Z. Feit, D. Eger, A. Zemel, Phys. Rev. B 31, 3903 (1985).

[4] V. Tetyorkin, S. Movchan, Semicond. Phys., Quantum Electronics & Optoelectronics 3, 300 (2000).

[5] E.P. Skipetrov, E.A. Zvereva, L.A. Skipetrova, Belousov V.V., Mousalitin A.M., J. Cryst. Growth 210, 292 (2000).

[6] E.P. Skipetrov, E.A. Zvereva, O.S. Volkova, E.I. Slyn'ko, A.M. Mousalitin, Mater. Sci. Eng. B 91-92, 416 (2002).

[7] V.E. Slyn'ko, Visnyk Lviv Univ., Ser. Physic. 34, 291 (2001).

[8] V.I. Kaidanov, S.A. Nemov and Yu.I. Ravich, Sov.-Phys. Semicond. 26, 201 (1992).

[9] Butler J.F., Calawa A.R., Harman T.C., Appl. Phys. Lett. 9, 427 (1966).

[10] R. Dornhaus, G. Nimtz and B. Schlicht, Narrow-Gap Semiconductors, Springer-Verlag, Berlin, 1983.

[11] O. Kane, Phys. Chem. Sol. 1, 249 (1957).

[12] B.A. Akimov, R.S. Vadhva, S.M. Chudinov, Sov.-Phys. Semicond. 12, 1927 (1978).

INVESTIGATION OF OPTICAL HOMOGENEITY OF LANGASITE SAMPLES

O.A. Buzanov, I.S. Didenko, N.S. Kozlova, E.V. Zabelina

Moscow State Institute of Steel and Alloys, Leninskii Prospect, 4, 119049, Moscow, Russia

1. Abstract

In the work langasite (LGS, $La_3Ga_5SiO_{14}$) samples of different crystallographic orientations and forms were investigated to determine connection between optical heterogeneity and growing conditions. On the plates with two polished sides the interference pictures in bulk (IPB) of crystal were found. The main reason of IPB is heterogeneity of refractive indices. It was established by research of form of the plates' surfaces and absorption factor in various areas on a plate. The refractive index No and its dispersion were measured by method of a prism in range of wave lengths from 400 up to 800 nm, total measuring inaccuracy was less than 0,0001. It is possible to ascertain that heterogeneity of a refractive index along a direction of growth is much higher than in a perpendicular direction.

2. Introduction

Recently among the large quantity of piezoelectric materials for communication and connection devices, crystals of lantan-gallium silicate family (langasite (LGS), langatate, langanate) were found to be of increasing application. These materials were sure to become promising materials for application in devices of stabilization and selection of frequency on bulk and surface acoustic waves (SAW and BAW) due to thermostable cuts, high coefficient of electromechanical coupling and absence of structural phase transitions.

Most of physical properties of these materials (refractive indices and their dispersion, parameters of a lattice, propagation velocities of SAW and BAW, electrical conductivity and dielectric losses) strongly depend on structure and homogeneity of crystal. Apparently this affects stability of operational characteristics of acoustic filters.

In this work LGS samples of different crystallographic orientations and forms were investigated to determine relations between optical homogeneity, growth conditions and peculiarities of LGS application in SAW and BAW (surface and bulk acoustic wave) devices.

All samples were cut from the crystal grown by the Czochralski method in the iridium crucibles. Growing method is well known and is described in many works [1, 2].

We used yxlt/48,5^o/26,6^o cuts – two plates with thickness 0,5 mm both prepared as the wafer for SAW devices, with both polished sides, but one with colored banding (sample №1 and sample №2), also we had two z-cuts – plates with both polished sides and thickness 4,75 mm: sample №3 cut from the middle part of the boule and sample №4 cut from the upper part of the boule. And two prisms: sample №4 – cut along the axis of growth, basic surface $\left[01\bar{2}0 \right]$ and sample №6 cut perpendicular to the axis of growth, basic surface $\left[01\bar{1}0 \right]$.

3. Experiment

Shapes of surface of the LGS plates were investigated using the *interference method* and determined that inteferogrammes of the surfaces of samples for SAW devices have an

essential deviation from flatness – a complex relief. Superposition of interference pictures in the bulk and on the surface of the plate can be seen on these photos.

a)   b)

c)   d)
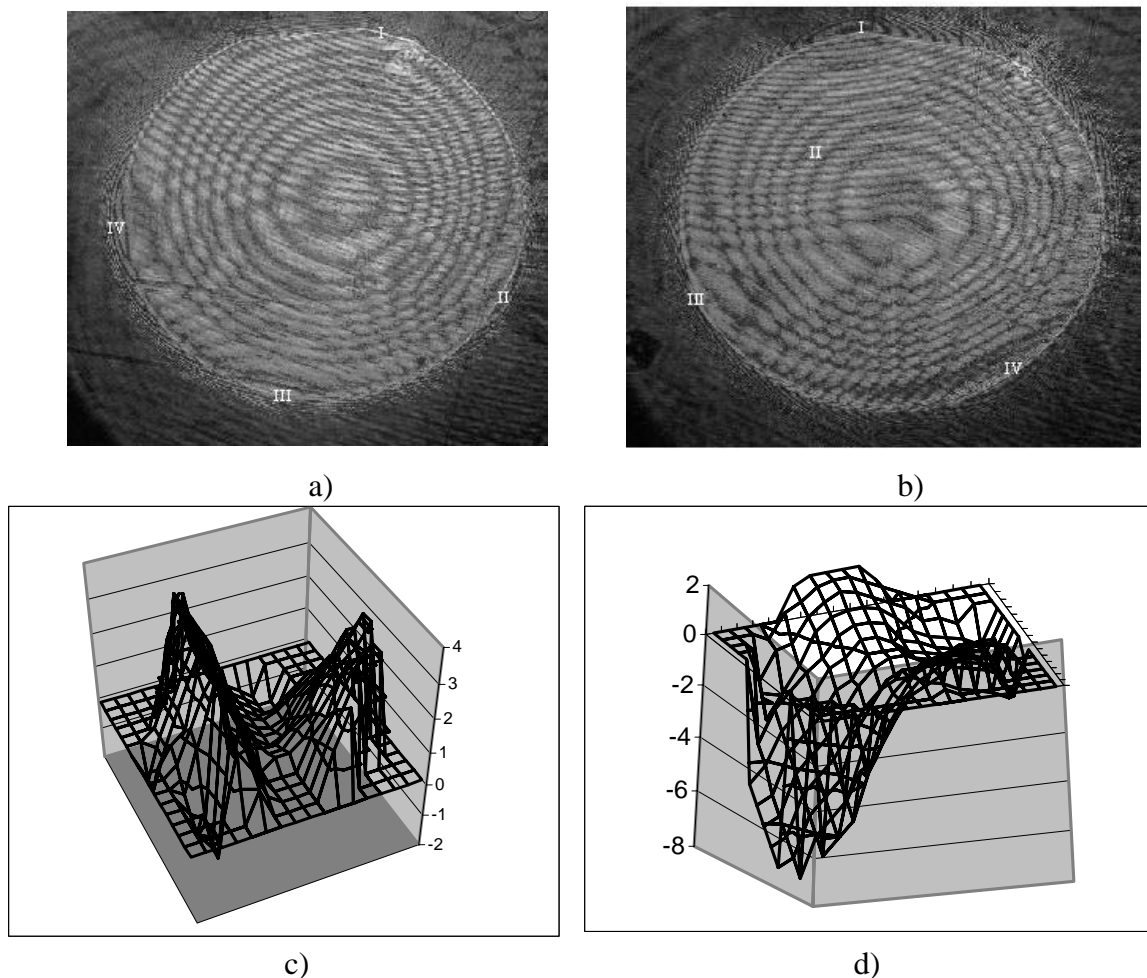
Picture 1 - Deviation from flatness of the sample № 1 with two polished side (a, b). The scheme of sample's №1 relief (c, d).

While examining deviation from flatness of sample 1 with two polished sides in addition to the surface interference pictures (IPS) on the plate with two polished sides we found the interference pictures in bulk (IPB) of crystal. We observed this IBP when the plate was in free state and when the plate was in the stressed state both. In picture 1 (a, b) the superposition of IPS and IPB can be seen. Also IPB were observed on other plates with two polished sides (picture 2).

a)   b)
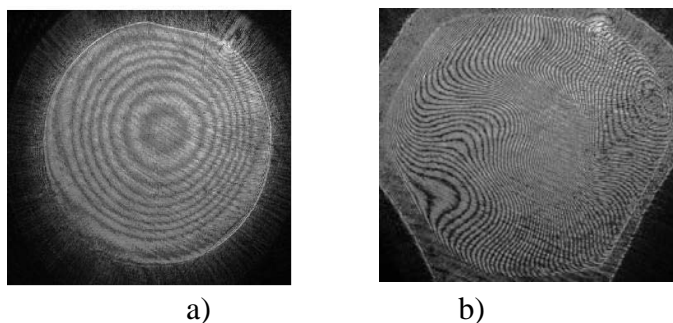
Picture 2 - IPB on the plates with two polished sides. a) sample №1, b) sample №3.

Location of IPB does not vary with the change of position of an interferometer's table. Also we found that circle IBP observed by us on the plates prepared according to the demands of the SAW preparations (but with two polished sides) correlates with SAW velocity distribution on plates used for filter manufacturing. Thus, investigating of IBP becomes of vital importance.

It is well-known that interference phenomenon in plates can be described by [3]:

$$\delta = 2 \cdot h \cdot n \cdot \cos r + \lambda/2$$

It means that path-length difference (δ) changes in consequence of several reasons – heterogeneity of the plate's thickness (h), heterogeneity of the refractive index (n) and variation of the hade (r).

The sample №2 was investigated by the method of the optical spectroscopy. The absorption factor in various areas on the plate is not connected with IPB. So, this kind of a banding can't be the reason of IPB appearing. It was established by research of the plate with both polished sides and colored banding.

We have analyzed results of investigations (pic. 1, 2) and carried out research of the plate's surface form and absorption factor in various areas on a plate, so we could prove that the main reason of IPB is heterogeneity of refractive indices.

The refractive index No and its dispersion were measured by method of a prism in a range of wave lengths from 400 up to 800 nm (table 1, picture 3), total measuring inaccuracy was less than 0,0001. Investigation of uniformity of refractive index No was carried out on bulk of the prisms on wavelength 587,5nm. The prisms were cut perpendicular and along the axis of growth $\left[01\overline{1}1\right]$ from single crystal. IPBs of these prisms were compared with distribution of refractive index.

Table №1 – Dispersion of the refractive indices of the prisms.

Wave-length, nm	Lamp	No	
		Sample №5	Sample №6
435,8	Hg	1,9340	
447,1	He	1,9306	
467,8	Cd	1,9248	1,9248
492,1	He	1,9194	
501,6	He	1,9176	1,9180
508,5	Cd	1,9160	1,9163
521,8	Cu	1,9138	
546,0	Hg	1,9099	1,9096
578,9	Hg	1,9055	1,9055
587,5	He	1,9046	1,9044
643,8	Cd		1,8984
667,8	He	1,8967	1,8970

Taking into the consideration the arrangement of prisms and the direction of measurements of a refractive index with respect to a crystal growth direction, it is possible to ascertain that heterogeneity of a refractive index along the direction of growth is much higher than in perpendicular direction.

a)   b)
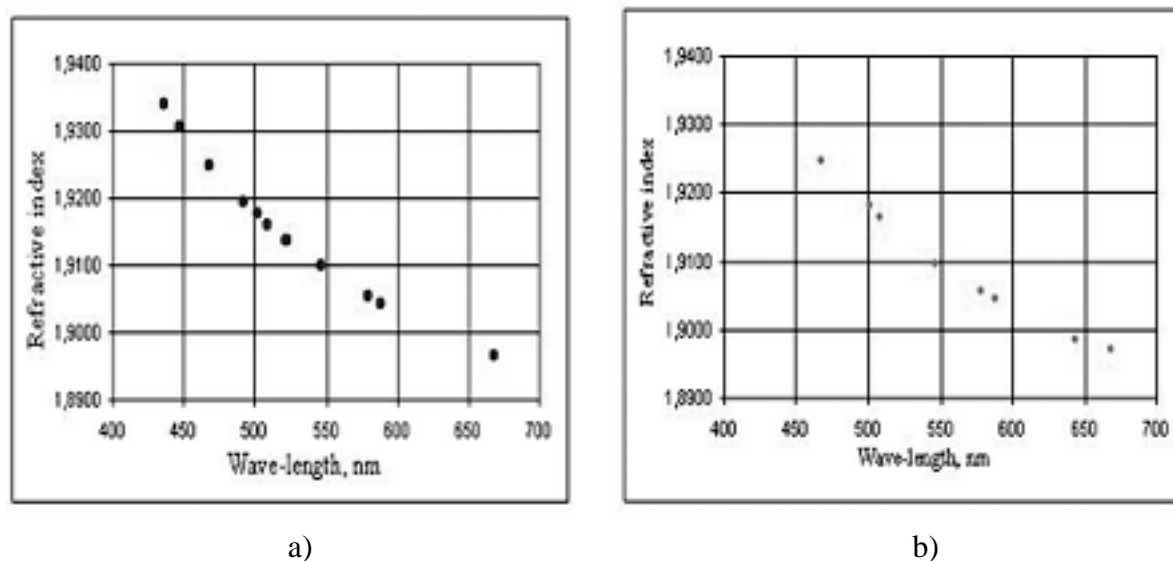
Picture 3 - Dependence of refractive index on wavelengths. a) sample №5, b) sample №6

As we had a z-cut plates we could use the method of optical polarization to show causal relationship between IPB and areas of the sample with maximum optical heterogeneity. Investigation was carried out on sample №4. Research was carried out using test stand with main parts including He-Ne laser (wave-length 0,63μm), polarizer (P), analyzer (A) and fixing device.

During the investigation we confirmed that specific coefficient of optical activity – it is 3 deg/mm for wavelength 0,63 μm.

Also we measured minimal light-stream intensity over ten and twenty points in two perpendicular directions. We found out that the observed phenomena are not equal in different parts of one plate – valuation of minimal light-stream intensity differs greatly. Also we revealed that maximal optical heterogeneity correlates with the parts of a plate with cercal and clear IPB.

IPB were observed also in other materials: sapphire, lithium niobate, melted quartz. IPB observing can be used as an express method for investigation of optical material homogeneity.

4. Conclusion

1. It was established by the interference method that surfaces of samples for SAW devices have essential deviation from flatness - a complicated profile.
2. In addition to the surface interference pictures (IPS) on the plates with two polished sides the interference pictures in bulk (IPB) of crystal were found.
3. It is determined that the main reason of IPB is heterogeneity of refractive indices.
4. Dispersion of refractive index was investigated and its orientation heterogeneity was found.
5. Causal relationship between IPB and areas with maximum optical heterogeneity was found by the method of optical polarization.
6. IPB are observed also in other materials: sapphire, lithium niobate, melted quartz, etc.
7. Observation of IPB can be used as an express method for investigation of optical materials homogeneity.

References

[1] A.N. Gotalskaya, D.I. Drezin, V.V. Bezdelkin, Aspects of growing langasite crystals and their properties // Journal de physique 4, Coloque C2, Supplement au journal de physique III. – 1994. - V. 4 – P. C2-201 – C2-210;

[2] S. Uda, O. Buzanov, Growth of 3" langasite crystal with clear faceting // Journal of Crystal Growth. – 2000 – V. 211 – 318-324;

[3] M. Born, E. Wolf, Principles of Optics - Oxford: Pergamon Press, 1959.

QUANTUM EFFICIENCY OF YTTRIUM AND TERBIUM GARNETS

M. Nazarov, Chulsoo Yoon, Chang Hoon Kwak, Jong Rak Sohn

Samsung Electro-Mechanics Co, LTD. 314, Maetan3-Dong, Yeongtong-Gu, Suwon, Gyunggi-Do, Korea, e-mail: nazarov.mihail@samsung.com

Abstract

A measurement system and mathematical procedure are developed for determining the quantum efficiency of luminescent materials. This technique based on standard photoluminescence DARSA PSI 5100 system (Diode Array Rapid Scan Analysis, Professional Scientific Instrument Co, Korea) or any other that allows measure the emission and excitation spectra, is applied to conventional phosphor powders. The system described is tested for excitation in the near-UV and visible regions, but can be applied to higher energy excitation (UV), as well as lower energy excitation to near-IR, with the appropriate photodetectors and optical filters. The system was tested on standard phosphors and on the new compositions. The accuracy of this measurement technique is acceptable for express analysis of quantum efficiency of luminescent materials.

1. Introduction

There is a need for a simple and accurate method to determine the quantum efficiency of luminescent materials. Ideally, such a technique for express analysis should require minimal sample preparation and should be simple in application. In this paper we report a technique that satisfies these criteria. The quantum efficiency (QE) of a luminescent material is defined as the ratio of the number of photons emitted to the number of photons absorbed. This ratio is also termed quantum yield (QY). In contrast, the radiant efficiency (RE) is the ratio of the output power to the input power. Quantum efficiency has long been used as a criterion for the selection of luminescent materials for application in fluorescent lighting [1-3], at panel displays [4,5], and more recently, solid-state lighting. A problem with some QE measurement techniques described in the literature is the lack of an acceptable calibration standard. For example, QE measurements of powder samples are often made in a system that cannot accommodate liquid fluorescence standards. There are three predominant techniques in the literature for measuring QE: absolute optical; relative optical; and photocalorimetric. In optical approaches, a primary challenge is determining precisely the amount of incident light absorbed by the phosphor. The amount of incident light absorbed can be determined directly,

or calculated from the sample reflectance. Most of the QE values in the literature for powder phosphors use the latter method and the reflectivity of standards such as MgO or $BaSO_4$. Photocalorimetry and photoacoustic spectroscopy have been investigated as alternatives to optical methods for QE measurements [6–8]. In photoacoustic spectroscopy (PAS), a black absorbing standard is used. The method is based on the optoacoustic effect where modulated light incident on a sample will produce a temperature rise in the sample that manifests itself by a periodic pressure wave that can be measured with a microphone transducer. The magnitude of the temperature wave depends on the sample absorption and the efficiency of non-radiative transitions. In this technique, the thermal energy of the Stokes shift contributes to the PAS signal, as any other non-radiative processes do, but the luminescence energy does not. PAS and photocalorimetry are difficult because good thermal contact is critical, small temperature fluctuations (mK) are difficult to detect, and thermal isolation from the surroundings is a challenge.

The technique described herein is very simple and can be applied effectively to powder phosphors, all of which we are interested in characterizing.

2. Experimental

The luminescence spectrum is obtained by plotting the relationship between the wavelength and the intensity of the emitted light from a sample excited by an appropriate excitation source of constant energy. The excitation source can be light, an electron beam, heat, X-rays, or radiation from radioactive materials. The spectrum is obtained using a monochromator equipped with an appropriate light detector.

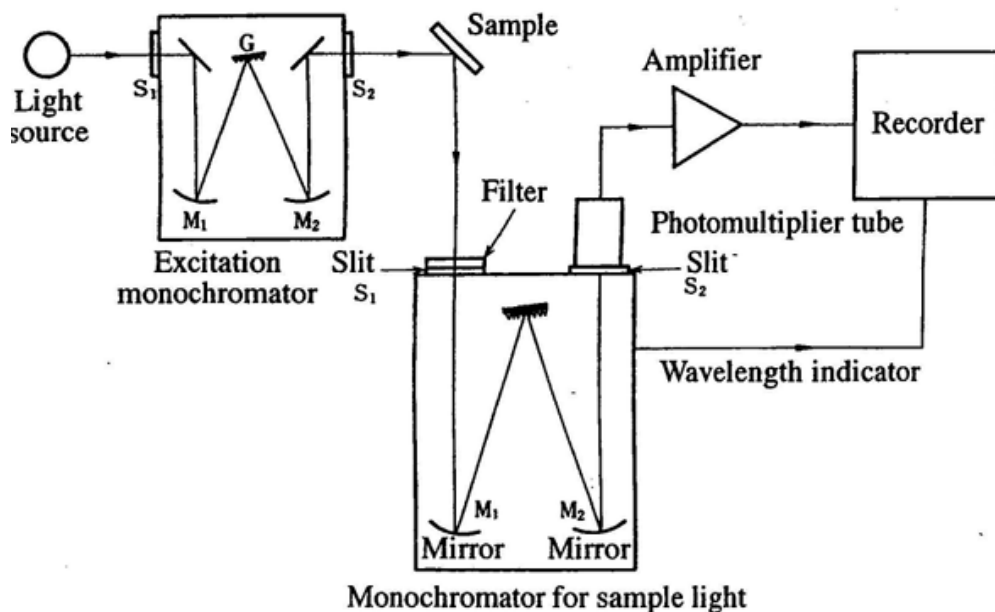The apparatus for measuring the spectral characteristics of phosphors is shown in Fig.1

Fig.1. Spectroscopic measurement apparatus

The excitation source consists of the light source and a monochromator, which selects a specific wavelength range from the incoming light. The light emitted from the sample is analyzed by a monochromator equipped with a light detector.

Emission, excitation, and reflection spectra have to be measured for calculation of the quantum efficiency of phosphors. Two monochromators and Xe lamp as excitation source are necessary. $(YGd)_3Al_5O_{12}$:Ce (YAG) phosphor with known QE could be proposed as standard test sample.

Spectral photon irradiance is expressed as:

$$E_p(\lambda) = \frac{dE_p}{d\lambda}; \quad E_p = \int_0^\infty E_p(\lambda)d\lambda \qquad (1)$$

For quantum efficiency of the investigated sample and the standard one we have:

$$\frac{\alpha_x q_x}{\alpha_{st} q_{st}} = \frac{E_{p_x}}{E_{p_{st}}}; \qquad (2)$$

where q_x and q_{st} are the quantum efficiencies of the specimen investigated and the standard (commercial YAG material, for example), and α is an absorption coefficient

$$q_x = \frac{(1-R_{st})\int_0^\infty E_{p_x}(\lambda)d\lambda}{(1-R_x)\int_0^\infty E_{p_{st}}(\lambda)d\lambda} q_{st} \qquad (3)$$

The following formula is applied in the calculations:

$$q_X = \frac{(1-R_{ST})}{(1-R_X)}\frac{\Phi_X}{\Phi_{ST}} q_{ST} \qquad (4)$$

R_X and R_{ST} are the reflectance of the specimen and the standard, and Φ_X and Φ_{ST} are the total measured luminescence efficiency (the integrated area under the emission spectrum) of the specimen and the standard, respectively.

The reflectance R_X and R_{ST}, respectively, of the investigated and standard samples are calculated from the formula

$$R_N = \frac{A_{RN}}{A_{RB}} 0.97 \quad , \qquad (5)$$

where R_N stands for a sample reflectance (N = X and ST for investigated powders and the YAG standard, respectively), and A_{RN} and A_{RB} are total areas under the measured reflection spectra for the sample investigated and the MgO, respectively. In this formula the number 0.97 represents the reflectance of the MgO powder. (Instead of MgO, $BaSO_4$ with index 0.91 can be used).

3. Results and discussion

In figure 2 we show the scheme of experiment, which is realized with photoluminescent DARSA system for reflectance measurements:
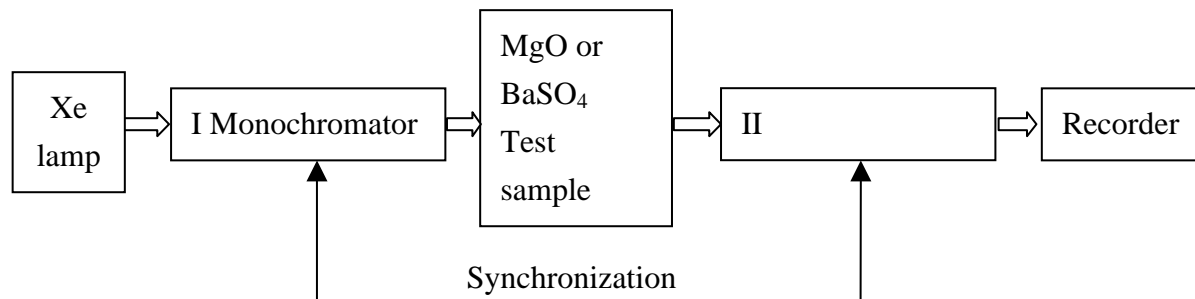

Fig.2 The scheme of QE measurement with DARSA system

If the spectroscopic system doesn't have a special integrated sphere (ISO40-SF/IG, for example), and does not allow to measure the guantum efficiency directly, the reflectance spectra measurements have to be carried out. Two monochromators are need to be synchronized at the excitation wavelength. At the fixed excitation wavelength of the first monochromator the emission spectra around this wavelength are measured by the second monochromator for the reference sample (MgO) and examined phosphors. Because of the Stock's shift (phosphors emit the light at the other wavelength that excite) the measured spectra are the reflectance spectra. The emission and excitation spectra of examined and standard samples are also registered.

Figure 3 compares excitation and emission spectra of investigated samples $Tb_3Al_5O_{12}:Ce^{3+}$ (TAG) and a double activated $Tb_3Al_5O_{12}:Ce^{3+},Eu^{2+}$ with commercial $(YGd)_3Al_5O_{12}:Ce^{3+}$ (YAG)
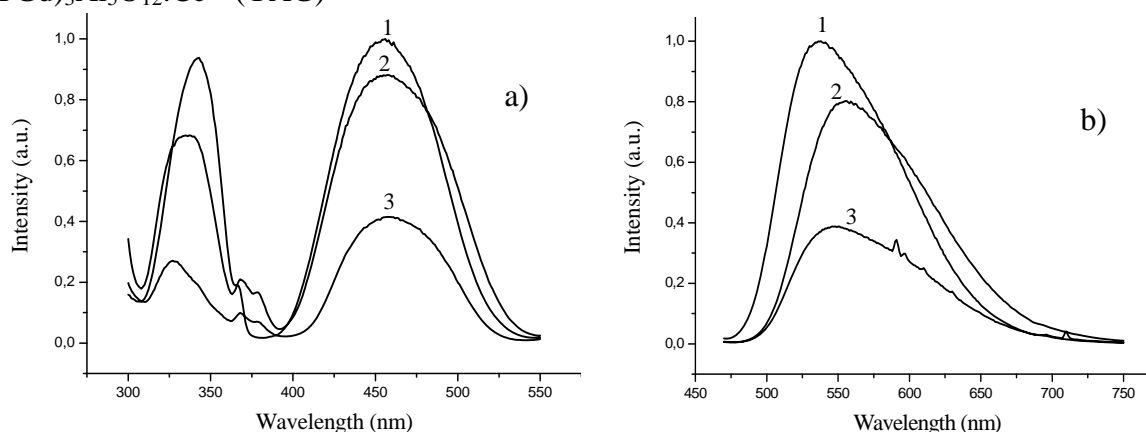

Fig.3. Excitation (a) and emission (b) spectra of investigated samples $Tb_3Al_5O_{12}:Ce^{3+}$(2) and double activated $Tb_3Al_5O_{12}:Ce^{3+},Eu^{2+}$(3) with commercial $(YGd)_3Al_5O_{12}:Ce^{3+}$ (1)

It is seen from Fig.3 that the luminescence spectra of specimens are very similar in the

shape and vary in intensities. The 2 broad bands from 310 to 380 nm in the long-wavelength UV region and from 400 to 520 nm in the blue spectral region correspond to the 4f-5d transitions of Ce^{3+} in YAG. The comparison of the luminescence spectra of the TAG -based phosphors with the emission of the commercial YAG convinces us that the latter can serve as a very convenient reference material against which the emission efficiency of our phosphors can be judged. Since the emissions of all materials investigated fall within exactly the same spectral region, there is no need to correct the emission spectra for the photomultiplier response to make a reasonable calculation of the quantum efficiencies of the emissions of the various TAG powders. Reliable judgment of the real efficiencies of the emissions from the various specimens requires an accurate determination of the amount of light absorbed by each of the phosphors investigated. This is especially important in our case, since the various specimens are characterized by different microstructures and the activator concentration. To compare the amount of light absorbed by an actual specimen, we measured reflection spectra for each of them and related them to the reflectivity of our standard commercial YAG phosphor and to the reflectivity of MgO. Equation (5) shows the relationship between the reflectance of the specimen investigated and the reflectance of the standard powder MgO.
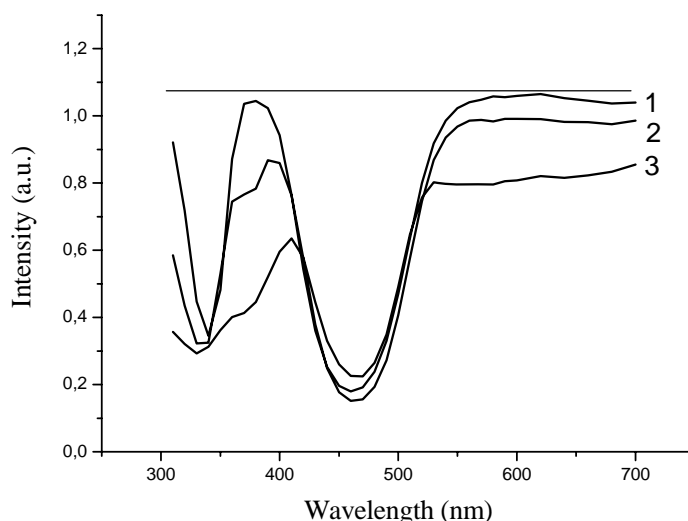

Fig.4. Diffuse reflection spectra of the $Tb_3Al_5O_{12}:Ce^{3+}$(2), double activated $Tb_3Al_5O_{12}:Ce^{3+},Eu^{2+}$(3) and commercial $(YGd)_3Al_5O_{12}:Ce^{3+}$ (1) in comparison with MgO.

In figure 4 we show reflection spectra for the commercial YAG and all the TAG samples (one of them (2) is doped with 6 mol % of Ce^{3+} and the other (3) with 3 mol % of Ce^{3+} and 3 mol % of Eu^{2+}), together with the spectrum of MgO. The results leave no doubt that, for reliable estimation of the quantum efficiency of an emission, it is definitely not enough to compare just the luminescence efficiency - it is also necessary to take into account the variations in the amounts of light absorbed by each of the samples. Despite the fact that all TAG specimens presented in figure 4 have the same host lattice, their capabilities for

reflecting the incident light vary strongly. It can be explained by the different Ce^{3+} activator concentration in the samples (2) and (3), as well as influence of Eu^{2+} on the luminescence properties of the sample (3). Thus the amount of light accessible for absorption by the Ce^{3+} ions (able to excite the phosphor) must also alter. Generally, as expected, with rising Ce content (6 mol % in the sample 2 and 3 mol % in the sample 3) less and less light is being reflected, what means that a still increasing amount of the light is being absorbed by the phosphor.

On the basis of the excitation (Fig. 3) and reflection (Fig.4) spectra, we decided that for the measurements of the quantum efficiencies of our phosphors, the most convenient excitation wavelength would be 460 nm. The diffuse reflection spectra at this wavelength are presented in Fig.5.
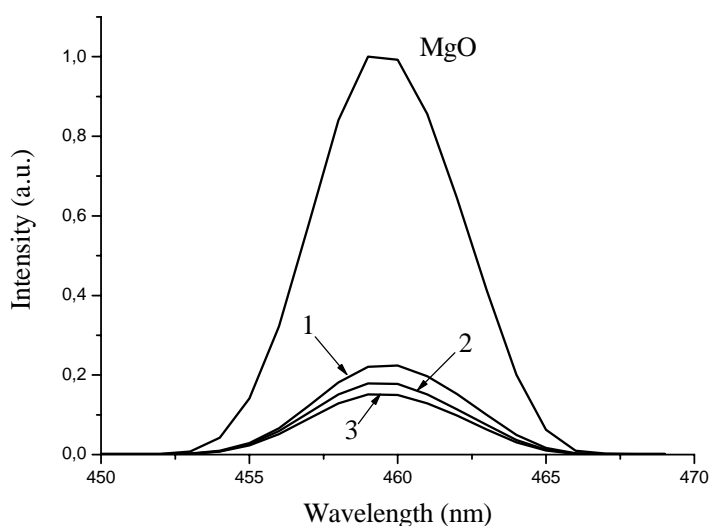

Fig.5. Diffuse reflection spectra of the $Tb_3Al_5O_{12}:Ce^{3+}$(2), double activated $Tb_3Al_5O_{12}:Ce^{3+},Eu^{2+}$(3) and commercial $(YGd)_3Al_5O_{12}:Ce^{3+}$ (1) in comparison with MgO at 460 nm excitation.

The quantum efficiency of phosphors calculated according to equations 4 and 5 and by using the experimental data from Fig.5, gives us the 76% for $Tb_3Al_5O_{12}:Ce^{3+}$ (6 mol % Ce) and 40% for $Tb_3Al_5O_{12}:Ce^{3+}$, Eu^{2+} (3 mol % Ce and 3 mol % Eu) relatively 90% $(YGd)_3Al_5O_{12}:Ce^{3+}$. It is not astonishing, because the main reason for a low intensity of the last sample is a lack of Ce activator and weak emission intensity in comparison with standard sample. The quantum efficiency practically does not depend on excitation wavelength in the large excitation area. It is good seen from Fig.6 for our samples and could be explained by the same processes of energy absorption, energy transfer and emission at different excitations. The quantum efficiency strongly depends on the sample structure and activator concentration.
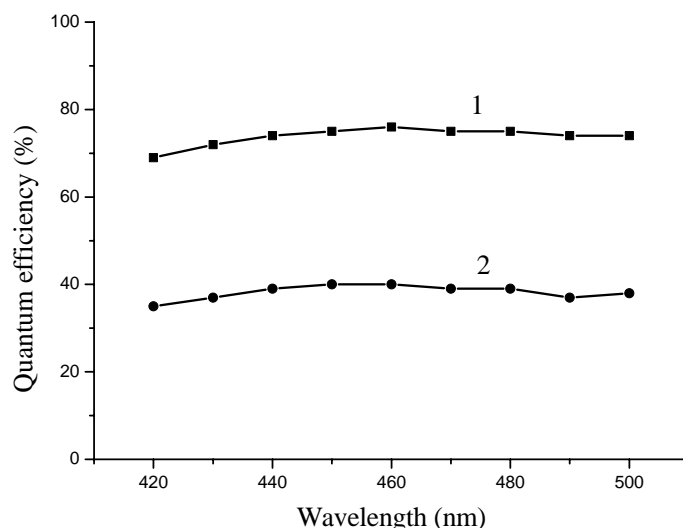
Fig.6. The quantum efficiency of (1) $Tb_3Al_5O_{12}:Ce^{3+}$ (6 mol % Ce^{3+}) and (2) $Tb_3Al_5O_{12}:Ce^{3+},Eu^{2+}$(3 mol % Ce^{3+} and 3 mol % Eu^{2+}) in dependence on excitation wavelength.

Energy absorption does not necessarily take place at the activator ion itself but can occur at a random place in the lattice. This implies that energy transfer of the absorbed energy to the luminescent center takes place before emission can occur. The migration of the energy absorbed by the lattice can take place through one of the following processes:

- migration of electric charge (electrons, holes),
- migration of excitons,
- resonance between atoms with sufficient overlap integrals,
- reabsorption of photons emitted by another activator ion or sensitizer

The occurrence of energy transfer within a luminescent material has far-reaching consequences for its properties as a phosphor. On the one hand the absorbed energy can migrate to the crystal surface or to lattice defects where it is lost by radiationless deactivation. As a consequence the phosphor energy yield, that is the quotient of emitted light energy to initially absorbed energy, drops. In the same phosphor structure with the same defect concentration the energy loss is also the same and emission is determined by the activator concentration.

4. Conclusion

Simple express method of quantum efficiency measurement and calculation using PL spectroscopy system is proposed and the experimental scheme compatible with DARSA system is suggested.

The methodology of calculation of quantum efficiency from reflection spectra is discussed. The obtained results show that it is definitely not enough to compare just the

luminescence efficiency - it is also necessary to take into account the variations in the amounts of light absorbed by each of the samples.

Reference

[1] A. Bril, G. Blasse, J.A.A. Bertens, J. Electrochem. Soc. 115 (4) 395 (1968).

[2] G. Alexander, P. Ramakrishnan, T.K. Mukherjee, K.S.V. Nambi, Ind. J. Pure Appl. Phys. 31 531 (1993).

[3] J. Tregellas-Williams, J. Electrochem. Soc. 105 (3) 173 (1958).

[4] T. Juestel, J. Krupa, D.U. Wiechert, J. Lumin. 93 179 (2001).

[5] Y.R. Do, J.W. Bae, J. Appl. Phys. 88 (8) 4660 (2000).

[6] M.J. Adams, J.G. High.eld, G.F. Kirkbright, Analyst 106 850 (1981).

[7] M. Zachau, J. Lumin. 72–74 792 (1997).

[8] M.J. Adams, J.G. High.eld, G..F. Kirkbright, Anal. Chem. 52 1260 (1980).

MAGNETIC AND XPS STUDIES ON RNi$_5$ (R=La, Nd, Tb, Dy)-BASED COMPOUNDS

E. Burzo[1], S. Chiuzbaian[2], L. Chioncel[3], A. Takacs[1,2], M. Neumann[2], I. Creanga[1]

[1])*Faculty of Physics, Babes-Bolyai University, 400084 Cluj-Napoca, Romania*
[2])*Fachbereich Physik, Universitat Osnanbrück, D-49069 Osnanbrück, Germany*
[3])*Department of Physics, University of Nijmegen 6500 GL, Nijmegen, The Netherlands*

Abstract

Magnetic measurements and XPS studies were performed on LaNi$_{5-x}$Al$_x$, TbNi$_{5-x}$Al$_x$, DyNi$_{5-x}$Al$_x$, LaNi$_{5-x}$Cu$_x$ and NdNi$_{5-x}$Cu$_x$ systems. In addition, band structure calculations were also performed. The nickel moments in RNi$_5$ (R=Nd, Tb, Dy) compounds are of $\cong 0.17$ μ_B and $\cong 0.25$ μ_B at 2c and 3g sites, respectively. The nickel moments, in low temperature range, decrease when increasing Al or Cu content and are practically nil for x > 1. The 4f-5d-3d exchange interactions were analyzed and the contributions of local 4f-5d and short range 5d-3d exchange interactions to 5d band polarization are estimated. An effective field of the order of (30-40) T is necessary to induce a nickel moment, at 1.7 K. Above the Curie temperatures, the effective nickel moments were determined. The LaNi$_{5-x}$Cu$_x$ and LaNi$_{5-x}$Al$_x$ systems, show, at T $\leq$ 10 K, a T^2 dependence of the magnetic susceptibilities, while above a characteristic temperature T*, a Curie-Weiss contribution was evidenced. The magnetic behaviour of nickel is analyzed in models, which take into account electron correlation effects in d bands.

1. Introduction

The RNi$_5$ based compounds, where R is a rare-earth or yttrium were intensively studied in correlation with their use as hydrogen storage materials [1]. The RNi$_5$ compounds crystallize in a hexagonal structure of CaCu$_5$-type, having P6/mmm space group. In this structure the R atoms occupy 1a-type site, while nickel ones are distributed on 2c and 3g positions. The analysis of the magnetic properties of RNi$_5$ end series compounds evidenced interesting properties. The Curie temperatures, T$_c$, are very low, the maximum value, T$_c$ = 35 K, being reported for GdNi$_5$. In earlier studies it was suggested that nickel is non-magnetic in RNi$_5$-series. This fact was correlated with the paramagnetic behaviour of LaNi$_5$ and YNi$_5$ compounds. Later on, analyzing the magnetic properties of (Gd$_x$Y$_{1-x}$)Ni$_5$ [2] and (Gd$_x$La$_{1-x}$)Ni$_5$ [3] pseudobinary compounds, it has been shown that the mean magnetic nickel moment, at 1.7 K, in GdNi$_5$ is of $\cong 0.17$ μ_B/atom, antiparallel oriented to gadolinium moment. The nickel saturation moments decrease when substituting Gd by La or Y and are nil in LaNi$_5$ and YNi$_5$. In the RNi$_5$ (R=La,Y) [4,5], the magnetic susceptibilities, χ, at T $\leq$ 10 K follow a T^2 dependence. Above a characteristic temperature, T*, the χ^{-1} vs T shows a linear dependence as described by the Curie-Weiss law. The magnetic behaviour of these systems was analyzed in the spin fluctuation model [6].

The RNi$_{5-x}$Cu$_x$ with R = La [4], Nd [7] for x $\leq$ 2 crystallize in a CaCu$_5$ type structure. In case of RNi$_{5-x}$Al$_x$ with R = Nd, Gd [8], R = Dy [9, 10], R = La [11] systems for x$\geq$2, the structure changes from CaCu$_5$-type to HoNi$_{2.6}$Ga$_{2.4}$ type, having also P6/mmm space group.

In this paper we analyze comparatively, the crystal structures and magnetic properties of $RNi_{5-x}Cu_x$ systems with R = La,Nd and $RNi_{5-x}Al_x$ with R = La, Tb, Dy. In addition to magnetic measurements, X-ray photoelectron spectroscopy studies (XPS) and band structure calculations were also performed.

2. Experimental and Computing Method

The samples were prepared in induction or arc furnaces, in purified argon atmosphere. The samples were thermally treated in vacuum at temperatures between 900 and 1000^oC during 5 up to 6 days. The X-ray analyses show the presence of only one phase. The composition dependences of the lattice parameters for $DyNi_{5-x}Al_x$ and $NdNi_{5-x}Cu_x$ systems are given in Fig.1.
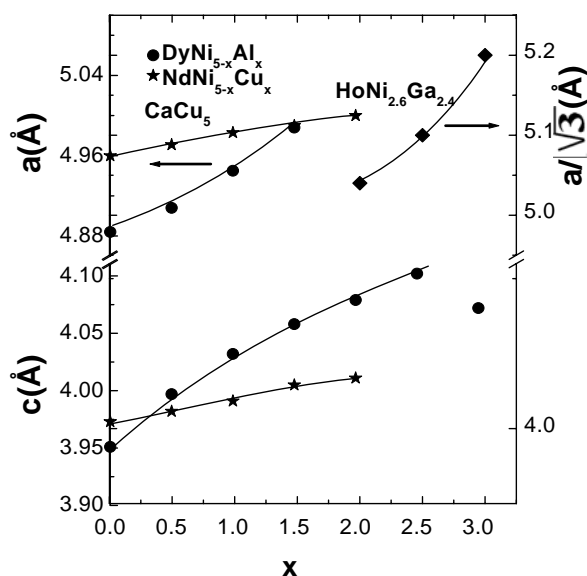

Fig.1 Composition dependences of the lattice parameters for $NdNi_{5-x}Cu_x$ and $DyNi_{5-x}Al_x$ compounds.

For $RNi_{5-x}Cu_x$ with R = La, Nd the presence of $CaCu_5$-type structure was shown for $x \leq 2$. In case of $RNi_{5-x}Al_x$ (R = La, Tb, Dy) having $x \leq 1.5$ also a $CaCu_5$-type structure was observed. For $2 \leq x \leq 3$ the structure changes to a $HoNi_{2.6}Ga_{2.4}$-type. This structure is also hexagonal (P6/mmm space group), but having a larger unit cell than $CaCu_5$-type. The unit cell parameters of the two types of structures are related by $a_{HoNi_{2.6}Ga_{2.4}} = \sqrt{3} a_{CaCu_5}$ and $a_{HoNi_{2.6}Ga_{2.4}} = c_{CaCu_5}$ [8]. In $CaCu_5$-type structure, the aluminum substitution takes place at the 3g site, situated in the z = 1/2 plane which does not contain R atoms. These sites allow greater Ni-Al distances. The total filling of the 3g site by Al is not possible since Ni(2c)-i(3g), Al(3g)-Al(3g) or Ni (3g)-Al(3g) distances are smaller than the sum of metallic radii $r_{Ni}+r_{Al}$ or $r_{Al}+r_{Al}$ [8]. The occurrence of $HoNi_{2.6}Ga_{2.4}$ superstructure induces an increase of the distances Al(3g)-Ni(6k) and Al(3f)-Al(6k) making the possibility to locate aluminum in 3f and 6k sites. In this structure nickel occupies completely 6l sites and aluminum 3f sites. The 6k sites are statistically occupied by Ni and Al.

Magnetic measurements were performed in the temperature range 1.7 – 300 K and fields up to 9 T. The saturation magnetizations, M_s, were determined from magnetization isotherms, according to approach to saturation law M = M_s (1-b/H), by extrapolating the

measured values at $H^{-1} = 0$. By b we denoted the coefficient of magnetic hardness. The paramagnetic contribution of conduction electrons was neglected. The errors introduced by the above assumption ware of the order of 0.1 μ_B/f.u. In the paramagnetic range, the susceptibilities, χ, were determined from their field dependences, according to the relation $\chi = \chi_0 + dM_0 H^{-1}$, by extrapolating the measured values to $H^{-1} \rightarrow 0$. By d we denote a presumed magnetic ordered impurity content and M_s is their saturation magnetization. By this method any possible alteration of magnetic susceptibilities, as a result of the presence of small quantities of magnetic ordered phase, is avoided. For all compositions, when exist, the estimated content of magnetic ordered phase, at $T > T_c$, is smaller than 0.1 %.

The XPS measurements were performed by using a PHI 5600 ci Multitechnique system. The spectra were recorded, at room temperature, using monochromatized Al K_α radiation (1486.6 eV). The total resolution, as determined at the Fermi level of a gold foil, was about 0.3-0.4 eV. Binding energies are given with reference to the Fermi level. The $4f_{7/2}$ level of gold was found at 84.0 eV binding energy. The samples were fractured in the preparation chamber and then moved into the main chamber. All spectra were recorded in a vacuum below 5×10^{-10} mbar.

Band structure calculations for $LaNi_{5-x}M_x$ (M = Cu, Al) and $DyNi_{5-x}Al_x$ were carried out by using the ab initio tight binding linear muffin-tin orbitals method in the atomic sphere approximation (TB-LMTO-ASA). The procedure of calculation was described elsewhere [12-14]. In the framework of the local density approximation (LDA), the total electronic potential is the sum of external, Coulomb and exchange–correlation potentials [15]. The functional form of the exchange–correlation energy used in the present work was the free-electron gas parametrization of von Barth and Hedin [16]. Relativistic correlations are included. For $NdNi_{5-x}Cu_x$ and $TbNi_{5-x}Al_x$ systems, band structure calculations were performed by using TB-LMTO within LDA + U approach [17,18]. The LDA + U scheme is based on the Anderson impurity model in mean field (Hartree-Foch) approximation, that analyzes the s and p electrons as noncorrelated, described by an orbital independent potential and d and f electrons are described by an orbital dependent potential [19]. When applied to transition metal and rare-earth compounds, the LDA + U method gives a quantitative improvement compared with LDA for ground state properties such as magnetic moments and interchain exchange parameters [14]. We note that this approach describes well the parallel coupling of Nd and Ni moments. In case of $RNi_{5-x}Cu_x$ systems the Cu atoms, for x=1, was supposed to occupy the 3g sites while for higher Cu concentrations both 2c and 3g positions. In case of $RNi_{5-x}Al_x$, for band structure calculations, the Al was introduced in 3g sites. For $HoNi_{2.6}Ga_{2.8}$ superstructure one Al atom was located in 3f sites and one or two aluminum atoms were distributed in 6k sites.

3. Band Structures

The total density of states as well as the Ni3d bands projected DOS, for some RNi_5 and RNi_4M (R = La, Nd, Tb, Dy and M = Cu or Al) compounds are plotted in Fig.2. In case of RNi_5 compounds the nickel at 0 K, has a magnetic ordered moment in compounds with magnetic rare-earths. The Ni moments are antiparallel aligned to R moments in heavy rare-earths (Tb, Dy) compounds and parallel oriented in light rare-earth (Nd) compounds.

The composition dependences of the magnetic moments at 2c and 3g sites in heavy rare-earth compounds are plotted in Fig.3.
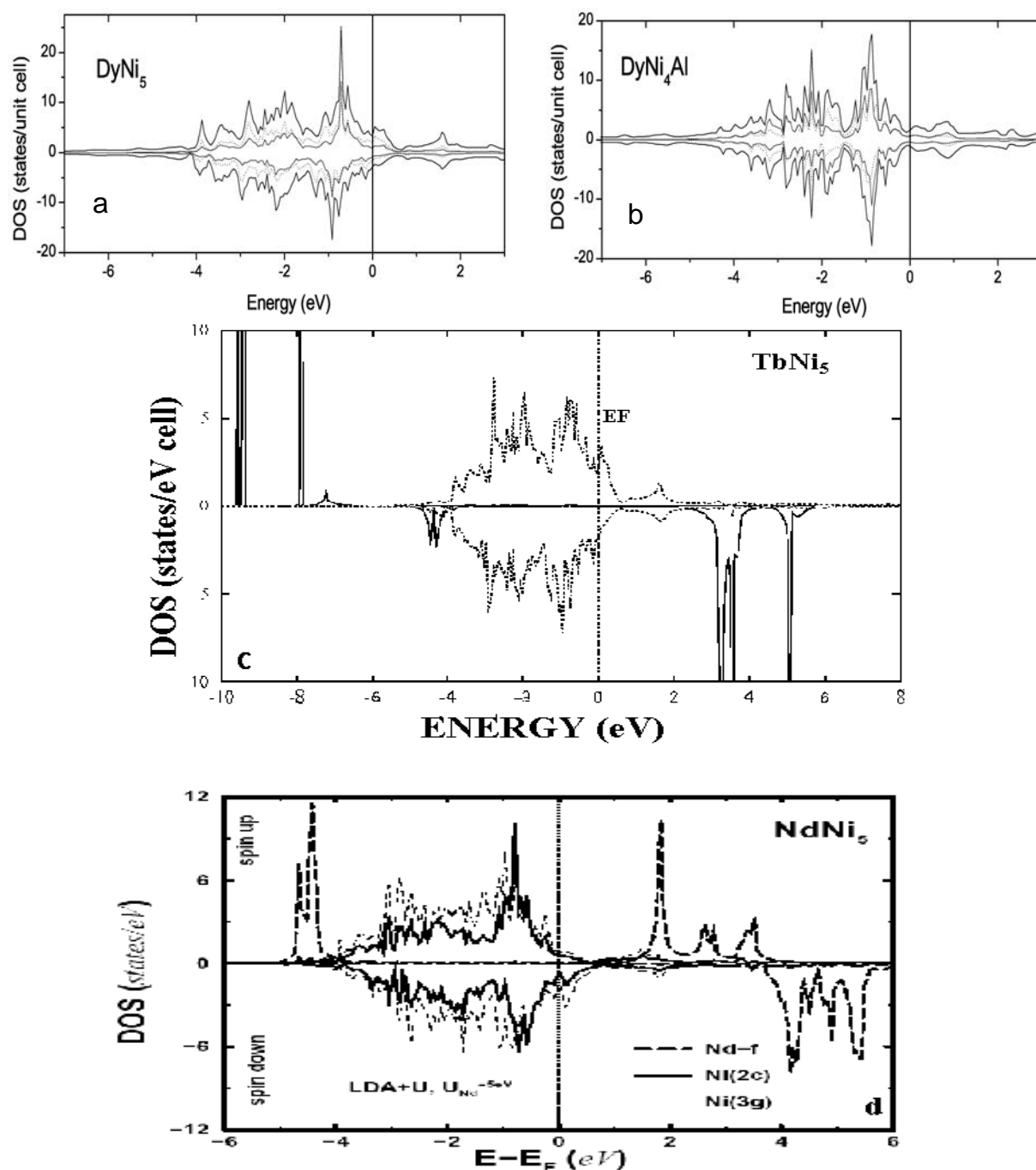
Fig.2 Projected densities of states for $DyNi_5$(a), $DyNi_4Al$(b), $TbNi_5$(c), and $NdNi_5$(d).

The magnetic moments at Ni(3g) sites are higher than those at 2c sites. This behaviour can be attributed to different local environments. The 2c sites in RNi_5 compounds have 6Ni(3g) and 3Ni(2c) atoms as well as 3R ones, while 3g sites have 4Ni(2c), 4Ni(3g) and 4R as nearest neighbours. The strength of the exchange interactions between nickel and magnetic R atoms is more important than between nickel ones, the Ni moments being essentially induced by R atoms. Thus, the exchange splitting of Ni3d(3g) band is greater than
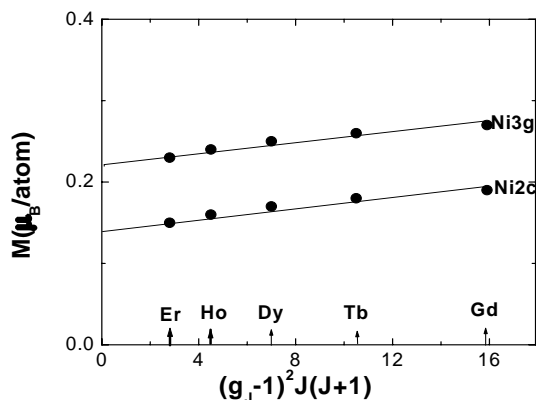
Fig.3 The dependences of Ni(2c) and Ni(3g) moments in RNi_5 compounds as function of De Gennes factor

for Ni3d(2c) one, since of the higher number of R atoms as nearest neighbours. For example, in $NdNi_5$, the exchange splitting of Ni3d(3g) band (0.01 eV) is greater than that at Ni3d(2c) sites (0.0066 eV). We note that the total contribution of Ni atoms to the magnetization is relatively small, particularly in heavy rare-earth compounds.

When replacing nickel by aluminium, the nickel moments, at 0K, decrease rapidly. For example in $DyNi_4Al$, values of 0.03 and 0.04 μ_B were determined at 2c and 3g sites, respectively. Values $M_{Ni}(2c) = 0.02$ μ_B and $M_{Ni}(3g) = 0.03$ μ_B were computed in $TbNi_4Al$ [10]. A somewhat smaller decrease of nickel moments was shown in $NdNi_4Cu$. Values of $\cong 0.06$ μ_B were determined both at 2c and 3g sites. These data suggest a strong hybridization of Ni3d and Al3p bands in aluminium substituted compounds. The variations of the magnetic moments at 2c and 3g sites in Al doped compounds can be correlated with the positions of the center of gravity of various bands [10]. The substitution of one Ni atom by Al in $DyNi_{5-x}Al_x$ decreases the degree of superposition of Ni3d(2c) and Ni3d(3g) bands as evidenced by an increase of the distances between their centers of gravity from $8.5.10^{-3}$ eV to $12.9.10^{-3}$ eV. The difference between the centers of gravity of Ni3d(3g) and Al(3p) bands (0.126 eV) is smaller that between Ni3d(2c) and Al(3p) (0.140 eV) suggesting a higher degree of Ni3d(3g)-Al(3p) bands hybridization. This may account for a higher decrease of the Ni3d(3g) moment (from 0.244 μ_B at x = 0 to 0.04 μ_B (x = 1) than for Ni3d(2c) (from 0.169 μ_B (x = 0) to 0.03 μ_B (x = 1)). The degree of hybridization of Dy5d – Ni3d(3g) bands is not changed for compound with x = 1 as compared to that having x = 0, while that of Dy5d–Ni3d(2c) decreases when replacing Ni by Al. Thus, the exchange interactions decrease as a whole, as evidenced by the diminution of Curie temperature from $T_c = 13$ K (x = 0) to 8 K (x = 1.0). The exchange interactions in R-M (M = Co or Ni) compounds are of 4f-5d-3d type [10]. Using this model we analyze in the following the 5d band polarization.

The R5d band polarizations for RNi_5 and RCo_5 compounds, where R is a heavy rare-earth, as function of De Genness factor, $G = (g_J-1)^2 J(J+1)$ are plotted in Fig.4.

The R5d band polarizations are linearly dependent on the De Gennes factor and can be described by the relation

$$M5d = M_{5d}(0) + \alpha G \qquad (1)$$

The slope α is the same for both series of compounds suggesting that it is characteristic of a given type of structure. We analyzed also this matter in RCo_4B compounds, whose crystal structure is derived from the $CaCu_5$ type. The same slope was evidenced, with $\alpha = 1.4 \times 10^{-2}$ μ_B, as in case of RNi_5 and RCo_5 compounds.
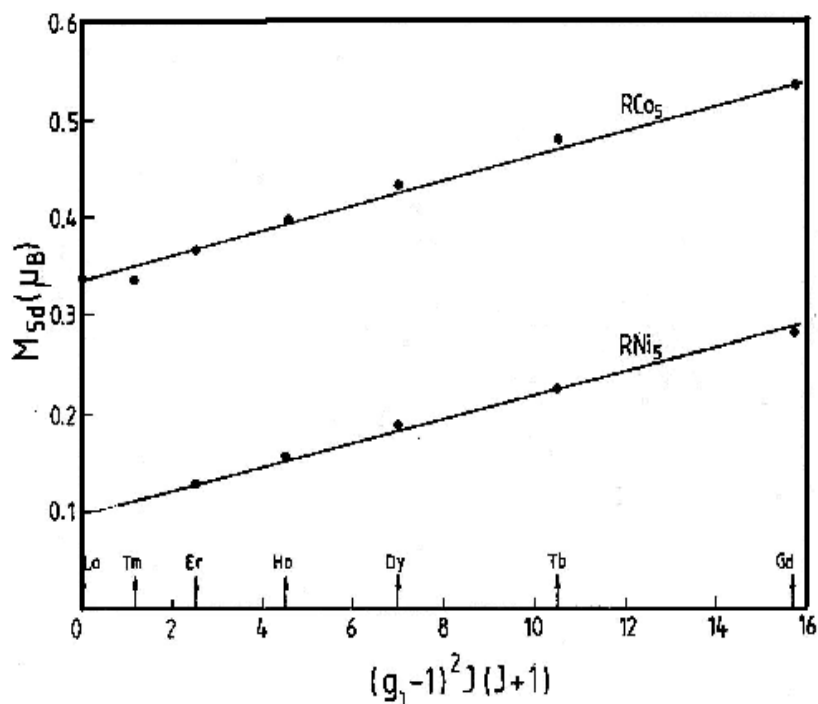
Fig.4 The R5d band polarizations in RNi_5 and RCo_5 compounds.

When increasing the magnetic contributions of transition metals, for a similar rare-earth compound, the R5d band polarization is translated to higher values. Thus, the composition dependence of 5d band polarization, described by relation (1) suggests the presence of two contributions. The first one, αG, is related to the local 4f-5d exchange interactions and seems to be essentially determined by rare-earth moment. The second one, $M_{5d}(0)$, can be attributed to the induced polarization by short range 5d-3d and 5d-5d exchange interactions. The $M_{5d}(0)$ value may be identified by the extrapolation of M_{5d} vs G variation to G = 0. The dominant contribution to $M_{5d}(0)$ is given by the exchange interaction of R5d with neighbouring transition metal atoms. A small contribution is also expected from R5d-R5d exchange interactions, which take place mainly through d_{3z^2-1} orbital with lobes oriented along the **c**-axis. Thus, the short range exchange interactions may be described by the Hamiltonian

$$H = -2\sum_i J_{3d_i-5d} S_{5d} \sum_{n_i} S_{3d_i,n_i} - 2\, J_{5d-5d} S_{5d} \sum_j S_{5d_j} \qquad (2)$$

We denoted by i the number of 3d atoms situated in the first coordination shell to an R atom, n_c is the number of atoms occupying a given i site and j is the number of R nearest neighbour atoms to a given R site.

The 5d-3d and 5d-5d exchange interactions act as an internal field, H_{exch}, on the 5d band and induce an additional polarization to that given by the local 4f-5d exchange. In the molecular field approximation the exchange field may be written as: $H_{exch} = N_{5d-3d}M_{3d} + N_{5d-5d}M_{5d}$, where N_{5d-3d} and N_{5d-5d} are the molecular field coefficients describing the R5d-M3d and R5d-R5d exchange interactions, respectively. In RCo_5 compounds, the contribution of second term in (2) may be neglected since $S_{3d} \gg S_{5d}$. For RNi_5 compounds the 5d band polarization is of the order of Ni3d moments, and consequently the last term in (2) cannot be neglected. In this case a reasonable approximation is $N_{5d-3d} \cong N_{5d-5d}$. As a result, the exchange field is proportional to total d magnetization, $M_d = M_{3d} + M_{5d}$, namely $H_{exch} = \xi M_d$. Previously [20], we showed that the induced 3d band polarization in rare-earth-transition

metal compounds is proportional to the exchange field, $\Delta M_d \propto \Delta H_{exch}$. Consequently, we have $M_{5d}(0) = \gamma M_d$. According to the above relation, as well as the Hamiltonian (2), the polarization is proportional to the $\sum n_k M_k$, where n_k is number of R and M atoms situated in first coordination shell having M_k magnetic moments. The $M_{5d}(0)$ values are plotted in Fig. 5 as function of $\sum n_k M_k$. In addition to data obtained for RNi_5 and RCo_5-based compounds, the 5d polarization for R(1a) and R(1b) sites in RCo_4B compounds is also given. As seen in Fig. 5, there is a linear dependence of $M_{5d}(0)$ on $\sum n_k M_k$. The slope is $\gamma = 0.04$. The same value was obtained for the ratio $M_{5d}(0)/M_d$ in RNi_5 and RCo_5 compounds. In the above discussion we considered the contributions to 5d band polarization as additive. In reality these values are reciprocal influenced and can be determined self consistently. The errors introduced by this approximation were estimated to be smaller than 8 %.
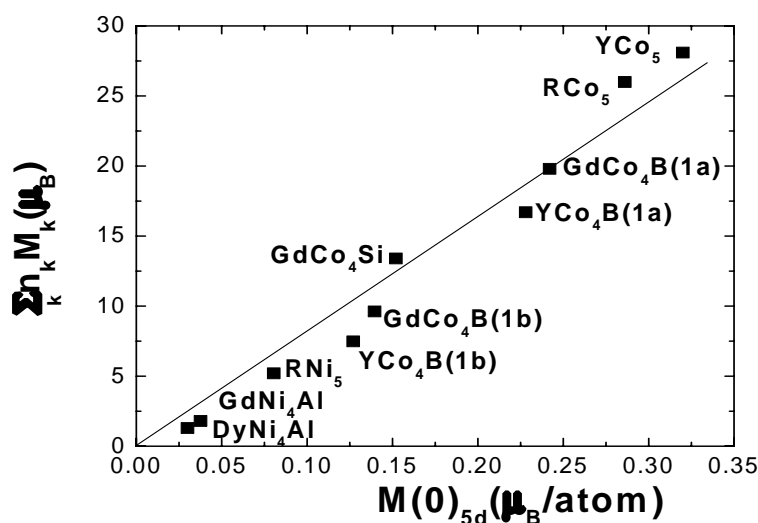

Fig.5: The $M_{5d}(0)$ contributions to 5d band polarization as function of $\sum n_k M_k$, the d magnetic moments of atoms situated in first coordination shell.
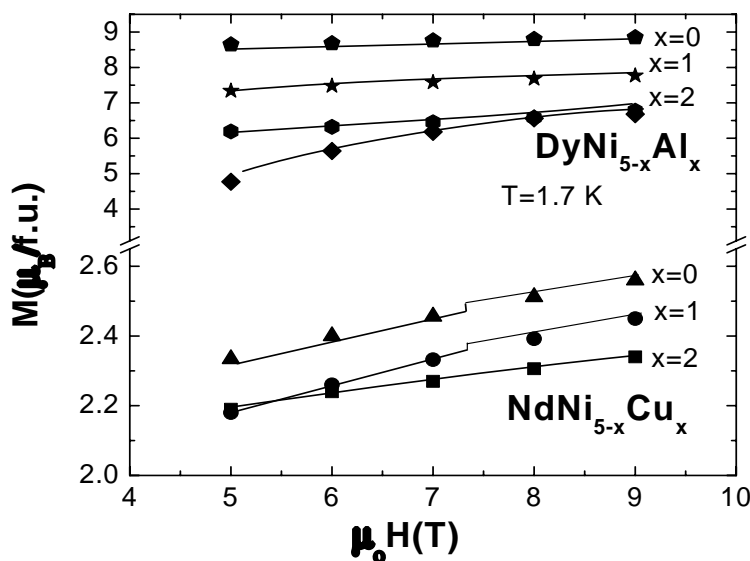

Fig.6 Magnetization isotherms, at 1.7 K, for $NdNi_{5-x}Cu_x$ and $DyNi_{5-x}Al_x$ compounds.

4. Magnetic Data

Representative magnetization isotherms, at 1.7K, for $DyNi_{5-x}Al_x$ and $NdNi_{5-x}Cu_x$ compounds are plotted in Fig.6. The saturation is more hardly to be obtained for higher aluminum substitution in $DyNi_{5-x}Al_x$ compounds. In addition, the magnetizations decrease when increasing the Al content. This behaviour is different from that expected considering an antiparallel alignment of Dy and Ni moments. As the Ni moments decrease, as shown from band structure calculations, the saturation magnetization must increase. Analyzing also the magnetization isotherms for sample with x = 2,3 we attribute the above unexpected behaviour to a micromagnetic type contribution superposed on an essentially ferromagnetic type ordering. We note that for compounds with x ≤ 1, the experimentally determined magnetizations are close to those obtained from band structure calculations. The Curie temperatures, T_c, decrease form 13K (x=0) to 8K (x=1) and 5K (x=2). High decrease of T_c values was also shown in $TbNi_{5-x}Al_x$ system. Values T_c = 23 (x=0), 20K (x=1) and 11K (x=2) were evidenced [21].

The magnetization isotherms for $NdNi_{5-x}Cu_x$ system, at 1.7 K, show for x = 0, the presence of a relatively high anisotropy. The M = f (H) curves saturate at lower field as the copper content increases. Thus, the coefficient of magnetic hardness decreases from a = 0.92 (x=0) to 0.32 (x=1) and 0.03 for x=1.5. These data suggest that Cu substitutes also nickel sites having high anisotropy. The largest orbital moment was seen in cobalt isomorphous compounds, at 2c site, which can be connected with a higher contribution to the anisotropy. This shows that a fraction of copper is located also in 2c sites. The saturation magnetizations experimentally determined are by 0.2-0.3 μ_B/f.u. smaller than those obtained from band structure calculations. The magnetization isotherms for compounds with x=0 and 0.5 show small discontinuities between 7 and 8 T. This behaviour cannot be seen for higher copper content. This may be correlated with a possible itinerant metamagnetic transition at some Ni sites. The Curie temperature of $NdNi_5$ is T_c = 9 K and decreases at 6 K for x = 1.0.
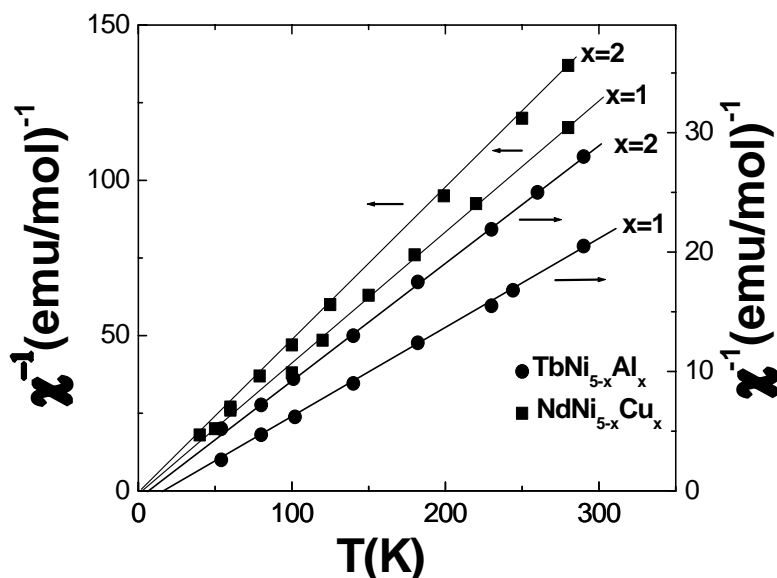

Fig.7. Thermal variations of reciprocal susceptibilities for $TbNi_{5-x}Al_x$ and $NdNi_{5-x}Cu_x$ compounds with x = 1 and 2
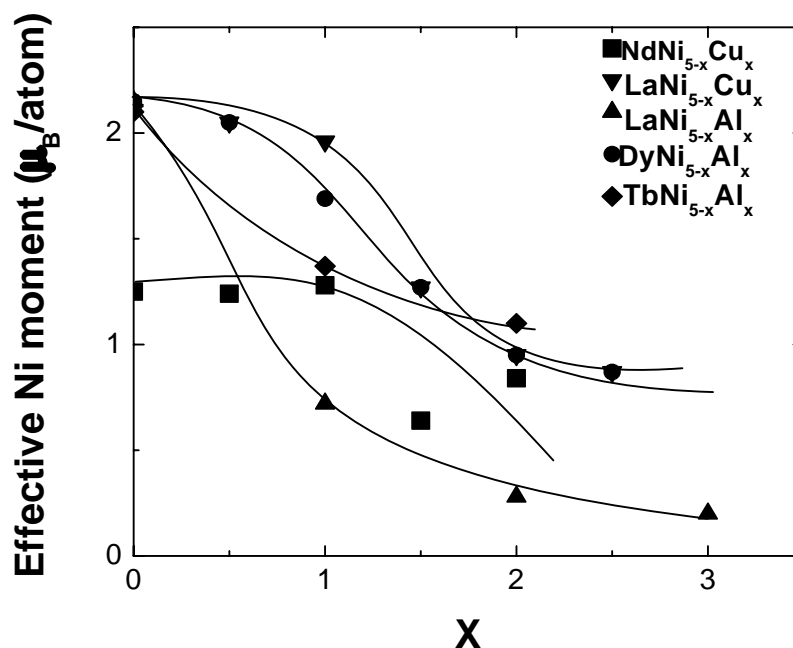
Fig.8 Composition dependences of the effective nickel moments.

The thermal variations of reciprocal susceptibilities for some representative compounds with magnetic rare earths are plotted in Fig 7. Curie-Weiss type dependences are shown, as described by the relation

$$\chi = \chi_0 + C(T-\theta)^{-1} \tag{3}$$

We denoted by C the Curie constant, θ is the paramagnetic Curie temperature and χ_0 a Pauli type term. In the above systems, the χ_0 contribution can be neglected.

The Curie constants are somewhat higher than those of free R^{3+} ions. Consequently, a contribution from nickel to C values is also suggested. According to addition law of magnetic susceptibilities and supposing that the effective moments of R ions are given by free R^{3+} values we determined the contributions of nickel to the Curie constants and the effective nickel moments, respectively. These values are plotted in Fig.8. The effective nickel moments in doped aluminium systems decrease more rapidly than in case of cooper ones, suggesting a strong hybridization of Ni3d and Al3d bands.

The magnetic behaviour of $LaNi_{5-x}M_x$ with M = Cu or Al were also studied – Fig.9 [4,11].

The magnetic susceptibilities increase up to a characteristic temperature, T_{max}. The T_{max} values are shifted to lower temperatures when increasing copper or aluminum content. Above a characteristic temperature, T^*, the reciprocal susceptibilities follow a Curie-Weiss type dependence, described by relation (3). The χ_0 contribution is important in Al substituted compounds and can be connected with the strong Ni3d-Al3p band hybridization. The Pauli type contributions increase from 1.0×10^{-4} emu/f.u. (x = 1) to 1.80×10^{-4} emu/f.u. (x = 2) and 1.85×10^{-4} emu/f.u. at x = 3.
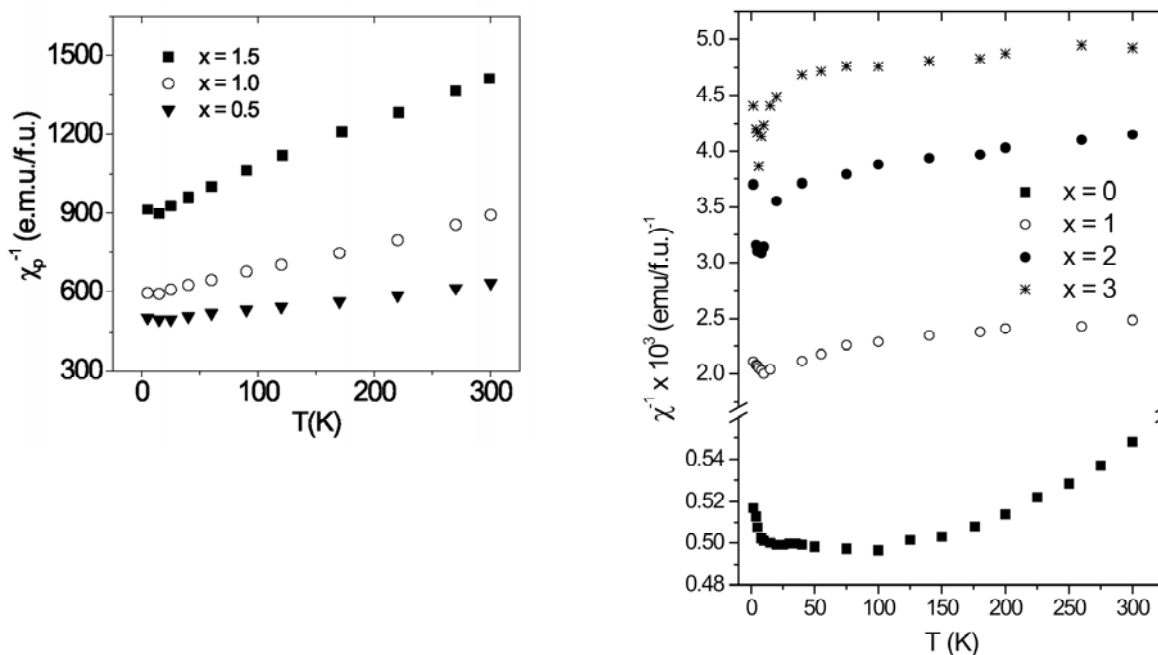
Fig.9 Thermal variations of reciprocal susceptibilities for $LaNi_{5-x}Cu_x$ (a) and $LaNi_{5-x}Al_x$ (b) compounds.

For copper doped systems the χ_0 values are of the order of 10^{-5} emu/f.u. and can be neglected as compared to second term of relation (3). The effective nickel moments determined from Curie constants are plotted in Fig. 8. These follow the same trend as for compounds with magnetic rare-earths. A stronger decrease of $M_{eff}(Ni)$ in aluminium compounds was shown. The paramagnetic Curie temperatures are negative and decrease in absolute magnitude as the Al or Cu content increases.

The calculated magnetic susceptibilities from band structures, at 0 K, and those experimentally determined, at 1.7 K are plotted in Fig. 10. There is a good agreement between two sets of data. A higher decrease was shown for aluminium substituted samples than for copper doped ones.

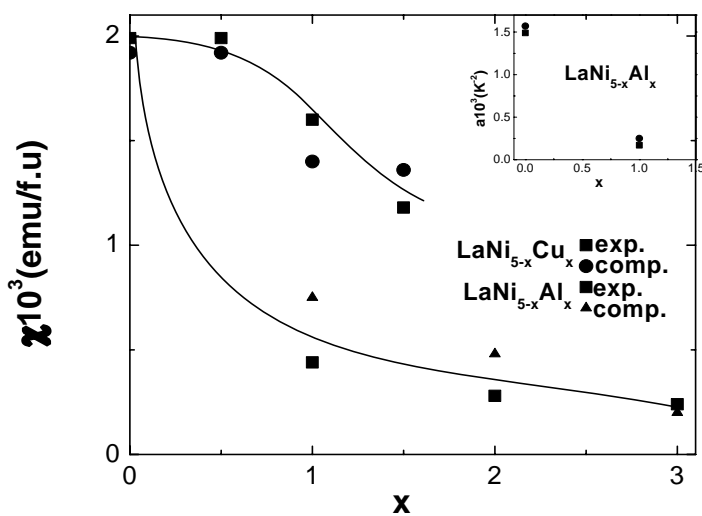Fig.10. Composition dependences of the susceptibilities, determined at 1.7 K, in $LaNi_{5-x}Cu_x$ and $LaNi_{5-x}Al_x$ and those obtained from band structure calculations. In the inset the determined and computed values for $LaNi_{5-x}Al_x$ with x = 0 and 1.0 are given.

In the low temperature range (T≤10 K), the magnetic susceptibilities follow a dependence described by the relation – Fig. 11:

$$\chi = \chi_0(1 + aT^2) \qquad (4)$$

with

$$a = \frac{\pi^2}{6}\left[\left(2\frac{N''(E_F)}{N(E_F)} - 1.2\left(\frac{N'(E_F)}{N(E_F)}\right)^2\right)\right] \cdot s^2 \qquad (5)$$
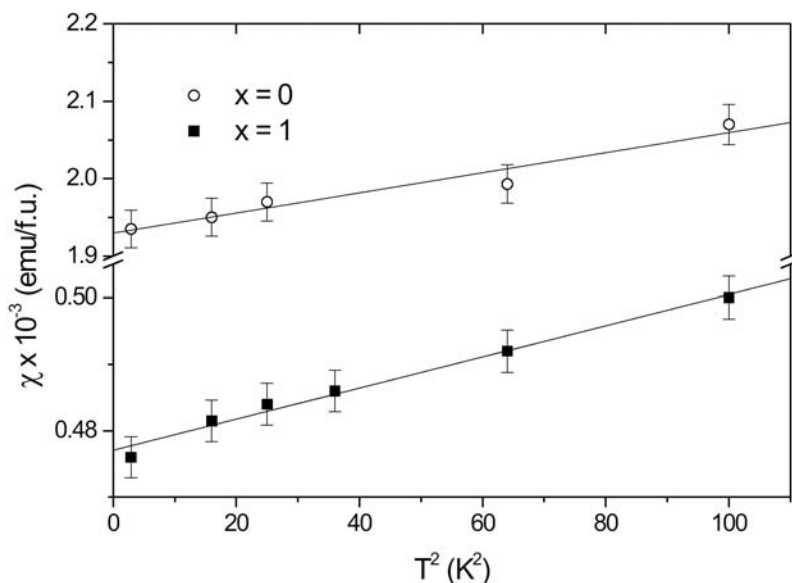
as determined considering the paramagnon model [22].

Fig.11 Temperature dependences of the magnetic susceptibilities for LaNi$_{5-x}$Al$_x$ system with x=0 and 1, at T≤10 K.

We denoted by s the Stoner enhancement factor and $N(E_F)$, $N'(E_F)$, $N''(E_F)$ are the density of states at the Fermi level and their first and second derivatives, respectively. We selected a symmetric energy interval around the self-consistent value of the Fermi level, and we used a mean square interpolation scheme in order to analytically evaluate the energy dependence of the density of states. This approach allowed us to evaluate the first and the second derivative of the DOS at the Fermi level. The values a, thus determined, according to relation (5), agree reasonably with those experimentally determined – inset Fig.11.

5. XPS Measurements

The Nd3d core level spectra in NdNi$_{5-x}$Cu$_x$ are plotted in Fig. 12a. The Nd3d$_{3/2}$ line is situated at 1003.6 ± 0.2 eV and that of Nd3d$_{5/2}$ at 981.2 ± 0.2 eV. The apparently small shift to higher binding energy ($\cong$ 0.4 eV) as compared to pure neodymium lines was attributed to the presence of small Nd$_2$O$_3$ content. The Dy4d core level spectra in DyNi$_{5-x}$Al$_x$ compounds were decomposed in four lines located at 152.3 ± 0.2 eV, 153.6 ± 0.2 eV, 155.0 ± 0.2 eV and 157.0 ± 0.2 eV – Fig. 12b. These are similar as those observed in Dy metal. We conclude that there are no changes in the positions of Nd3d and Dy4d core lines, as compared to pure metals, in both series of compounds.
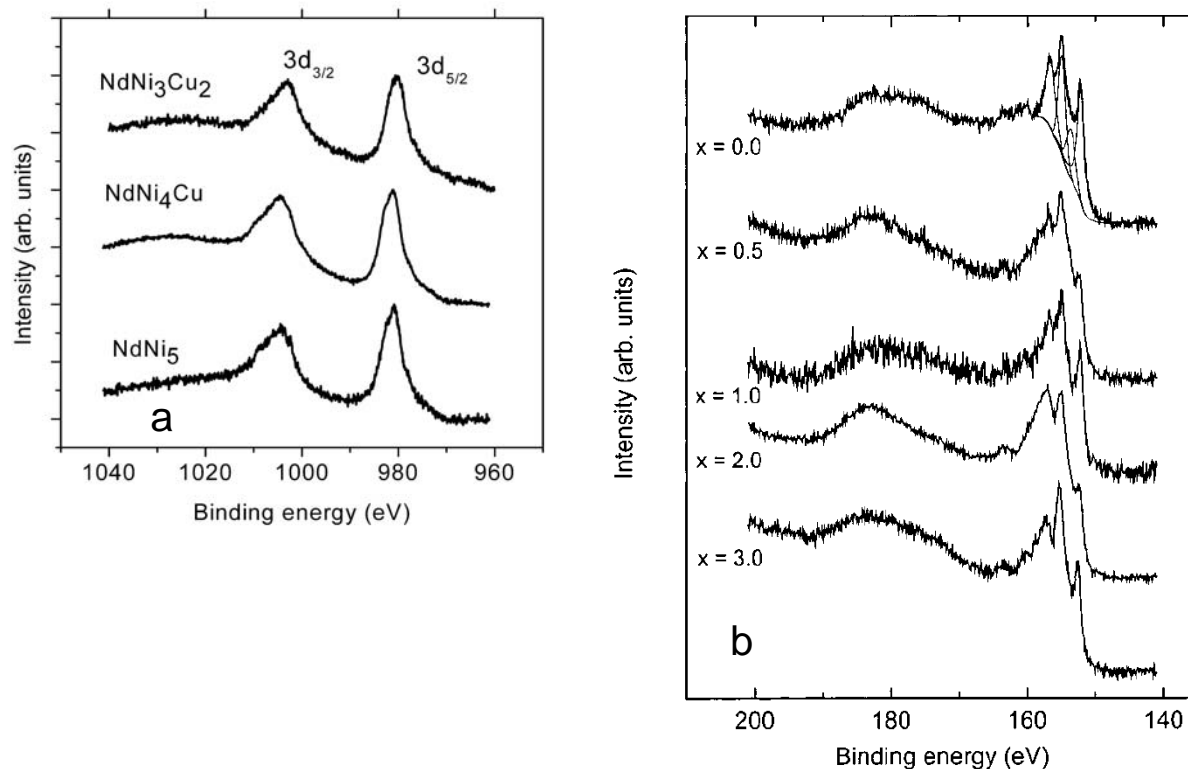
Fig.12. The Nd3d (a) and Dy4d (b) XPS spectra in $NdNi_{5-x}Cu_x$(a) and $DyNi_{5-x}Al_x$(b) compounds.

The $Ni2p_{3/2}$ and $Ni2p_{1/2}$ core level lines for some representative compounds are plotted in Fig.13. For comparison, the Ni2p spectrum of pure nickel is also given. The spectra were decomposed, as for pure nickel, considering the main lines and satellites. For example in $NdNi_{5-x}Cu_x$ system, the positions of the $2p_{3/2}$ and $2p_{1/2}$ line are situated at 852.5 ± 0.1 eV and 826.9 ± 0.1 eV, respectively and do not change with composition. These lines are located at the same binding energies as for pure nickel (852.7 ± 0.1 eV and 869.97 ± 0.1 eV, respectively). The 6 eV satellite is located at 858.5 ± 0.1 eV in $NdNi_{5-x}Cu_x$ system. The same behaviour was shown in other copper substituted compounds. Thus, the positions of the main and satellite lines are not changed with composition, in copper substituted system. A slight shift to higher binding energies was shown when Ni is replaced by Al. Thus, in $DyNi_{5-x}Al_x$ compounds the shifts of the Ni2p lines are of 0.1 eV (x = 0.5), 0.25 eV (x = 1.0), 0.3 eV (x = 2.0) and 0.6 eV (x = 3.0). There is also a more pronounced decrease of the Ni6 eV satellite intensities, when increasing Al content, than in Cu system. These features can be correlated with changes in nickel band structures, as a result of filling 3d band due to hybridization effects.

The Cu2p core lines, for $NdNi_{5-x}Cu_x$ system, are plotted in Fig. 14. The binding energies for $Cu2p_{3/2}$ states are situated at 932.5 ± 0.1 eV [7]. This value is close to that characteristic of pure copper located at 932.7 eV [23]. The $2p_{1/2}$ core lines for all compositions are situated at 952.3 eV, close to the value characteristic of pure copper (952.5 eV). Similar behaviour was shown in $LaNi_{5-x}Cu_x$ system. Taking into account that for Cu core level spectra, there are no satellite structures and in addition the lines are narrow, we conclude that the electronic configuration of copper is $3d^{10}$ (in atomic notation).
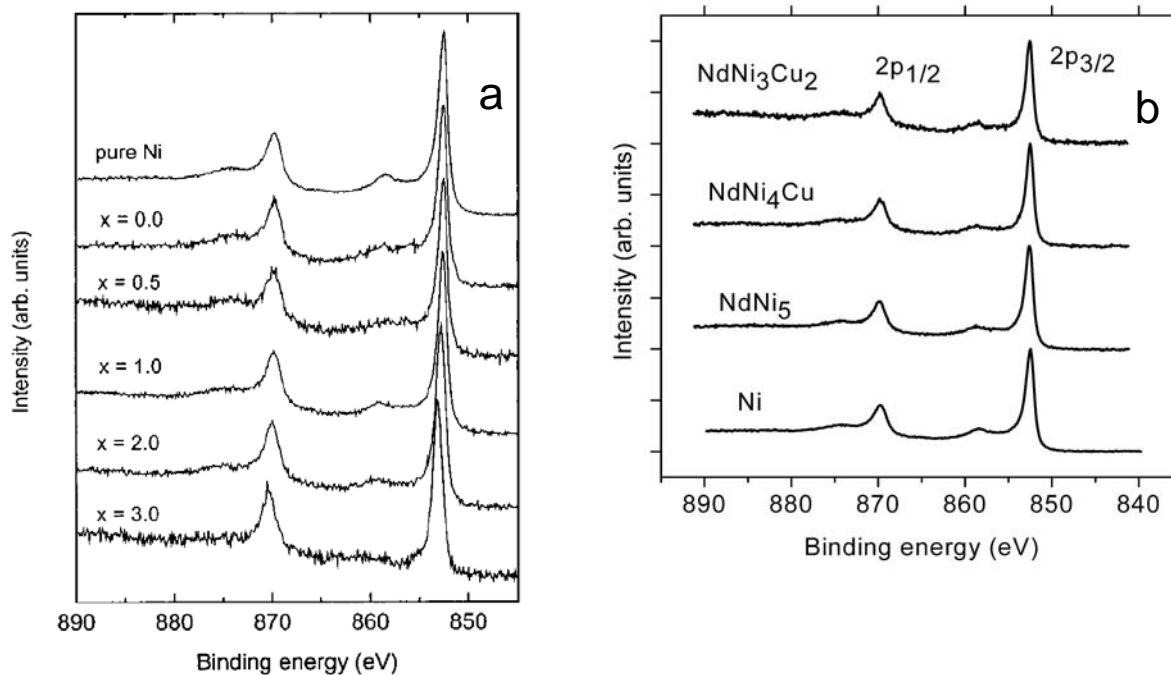
Fig.13. The Ni2p$_{3/2}$ and 2p$_{1/2}$ core lines for some DyNi$_{5-x}$Al$_x$ (a), NdNi$_{5-x}$Cu$_x$ (b) and LaNi$_{5-x}$Cu$_x$ (c) representative compounds.
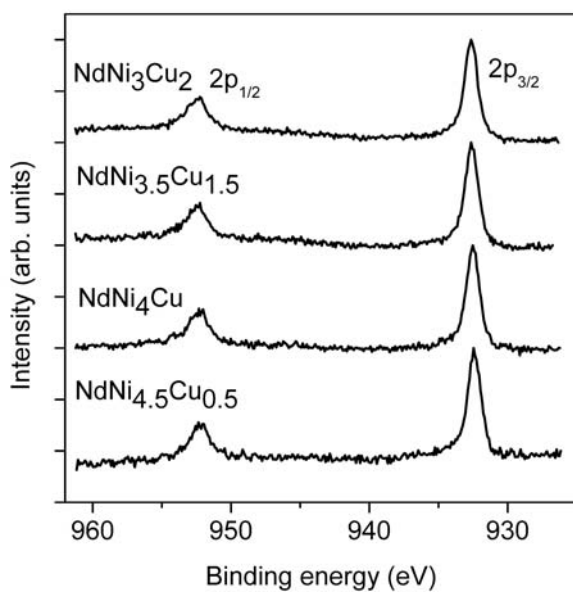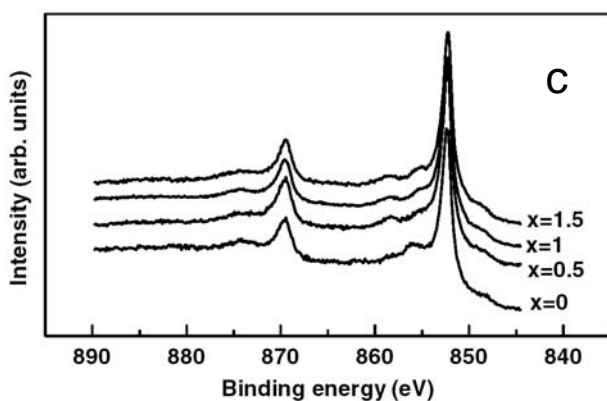

Fig.14. Cu2p core lines in NdNi$_{5-x}$Cu$_x$ system.

The XPS valence bands of $LaNi_{5-x}M_x$ with M = Al and Cu are plotted in Fig. 15, together with that of pure nickel.
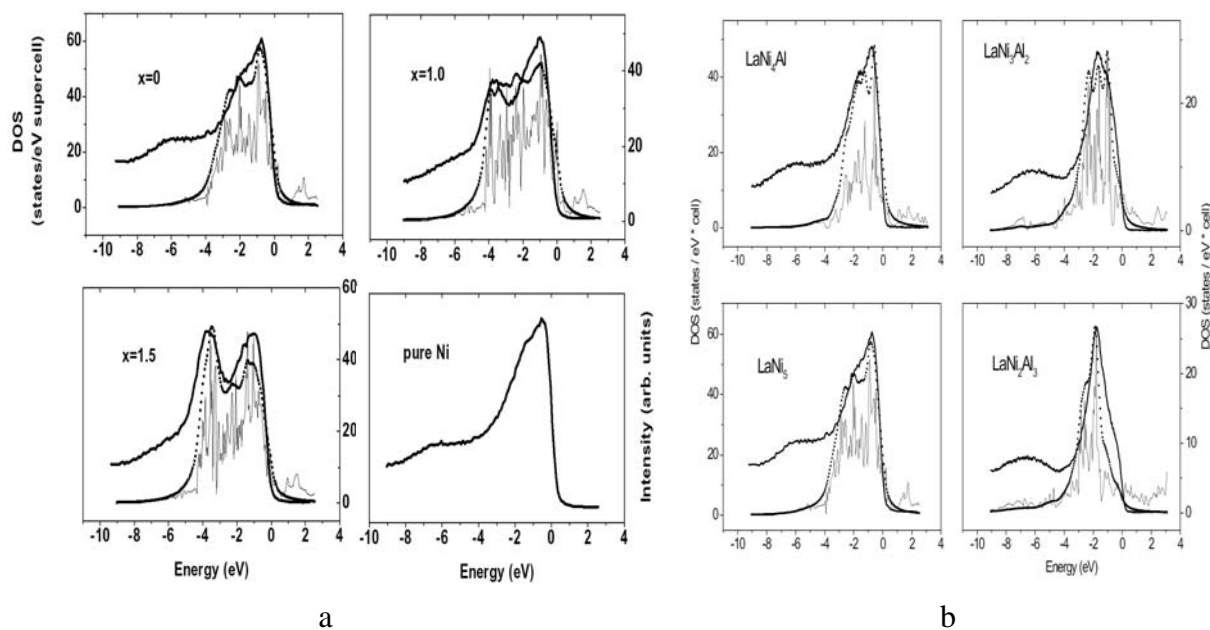

Fig.15. Comparison of the measured XPS valence bands (thick solid line), the calculated total DOS (solid line) and the convoluted DOS (with Lorentzian of half-width 0.4 eV and taking into account appropriate cross-sections for partial bands with different l-symmetry; dashed line) for $LaNi_{5-x}Cu_x$ (a) and $LaNi_{5-x}Al_x$ (b) series.

There is a similarity of the Ni3d bands for pure Ni with those for $LaNi_5$. This fact evidences that the valence band of $LaNi_5$ is mainly derived from Ni d states. There is also present the 6.0 eV Ni satellite. The intensity of satellites decreases when increasing Al content. In addition, the density of states at the Fermi level is diminished as compared with that of pure nickel and the maxima of the valence bands are shifted to higher binding energy. The positions of the maxima, as compared to Fermi level, are 0.59 eV for pure Ni, 0.67 eV in $LaNi_5$ and 0.80 eV in $LaNi_4Al$. In $LaNi_3Al_2$ the shift is by 1.60 eV and in $LaNi_2Al_3$ by 1.74 eV. The states at the Fermi level have mainly d character in $LaNi_5$. On alloying with aluminium, the s-p contribution to the DOS, at the Fermi level increases. In $DyNi_{5-x}Al_x$ the maxima in the valence band spectra are located at 0.65 eV (x = 0), 0.72 eV (x = 0.5) and 0.77 eV (x = 1.0) [10] near the same positions as shown in $LaNi_{5-x}Al_x$. Due to complexity of the spectra, the 6 eV satellite cannot be observed since of superposition with Dy bands.

The computed density of states in $LaNi_{5-x}Al_x$ describes rather well the general features of experimental spectra-Fig.15 [11]. The orbital-projected partial densities of states were multiplied with approximate cross-sections for 1486.6 eV incident radiation and their sum was then convoluted with Lorentzians of half-width 0.4 eV. There are also some differences between the two sets of spectra. These can be attributed to the fact that band structures were computed at 0 K and those obtained by XPS were recorded at room temperature. In addition, the correlation effects were not considered in computing the density of states. Also, the inelastic scattering background present in the XPS spectra was not substracted.

Alloying with Cu in $LaNi_{5-x}Cu_x$ system does not induce visible changes in the Ni d-band – Fig.15. A rather independent Cu d-band is formed at around 3.3 eV binding energy. By increasing Cu content, the relative intensity of Cu d band is increased. The width of Cu

line is not changed when increasing the Cu content. These Cu states are probably completely filled with electrons.

The XPS valence bands of $NdNi_{5-x}Cu_x$ samples are plotted in Fig. 16.
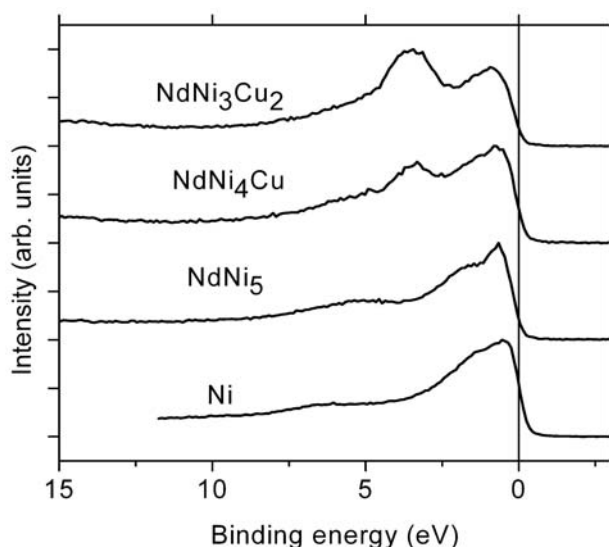

Fig.16. XPS valence band spectra of some $NdNi_{5-x}Cu_x$ compounds.

The 4f orbitals of Nd keep their localized character and therefore the XPS spectra show multiplet structures. These correspond to transitions between the ground state of configuration $4f^n$ and the accessible final states $4f^{n-1}$. The spectrum can be considered as a finger of the number of 4f electrons in the initial state. Thus, the XPS valence band spectrum of neodymium [24] evidences the presence of Nd4f contribution to the valence band at $\cong 4.65$ eV binding energy corresponding to $^3H_4$ state and those of Nd5d states at about 1 eV binding energy, the latter being spread up to Fermi level. In the valence band spectra of $NdNi_{5-x}Cu_x$, the the Nd lines are rather difficult to be observed since of their low intensity as well as due to the superposition with copper lines. Due to 5d-3d hybridization, the shape of nickel spectrum in $NdNi_5$ is somewhat modified around the Fermi level, as compared to pure Ni. Thus, although the valence band spectrum is similar to that of pure nickel, the density of states at the Fermi level is diminished. In addition, the valence band of Ni in $NdNi_5$ is shifted to higher energy. This may be correlated with an increase of d-state occupancies. When substituting Ni by Cu, rather independent Cu d band is formed at around 3.3 eV binding energy. As in case of $LaNi_{5-x}Cu_x$ system, the relative intensities of Cu d bands increase but their positions and the linewidths are not changed when composition is modified.

6. Magnetic Behaviour of Nickel and Rare-Earths

The XPS measurements, at room temperature, on $DyNi_{5-x}Al_x$ and $NdNi_{5-x}Cu_x$ systems on Nd4f and Dy4f show that the crystal field is well shielded by the valence electrons and is small compared with the separation of the multiplet states. This is in agreement with the results of magnetic measurements, which show that the rare-earth moments are close to the g_JJ values.

The exchange interactions in compounds with magnetic rare-earths can be well described by the Campbell model [25] which considers the 4f-5d-3d exchange interactions. The R4f electrons polarize the R5d band through local exchange interactions. The induced 5d polarization in heavy rare-earth compounds is parallel to the 4f moments. There are also short

range exchange interactions of 5d-3d and 5d-5d types which induced additional 5d band polarization.

The band structure calculations show that Ni moments at 0 K decrease very fast in the composition range $0 \leq x \leq 1$ and are near nil for higher Al or Cu substitutions. This behaviour can be attributed to hybridization effects and diminution of electron correlations between d electrons. There is a linear dependence of nickel moments at 2c and 3g sites on the exchange splitting of their 3d band. The extrapolation to nil nickel moment suggests a critical field for the appearance of a nickel moment of $\mu_0 H_{exch} = 30 - 40$ T.

In the paramagnetic range, for all studied composition, an effective nickel moment, $M_{eff}(Ni)$, is present. The $M_{eff}(Ni)$ values decrease when increasing the content of Cu or Al. The presence of unoccupied Ni3d states is also suggested by the XPS measurements, at room temperature. The Ni 6 eV satellite lines were shown in the whole composition range although their intensities decrease when increasing Cu or Al content.

The $LaNi_{5-x}M_x$ with M = Cu or Al compounds show an interesting behaviour. The magnetic susceptibilities, χ increase up to a temperature T_{max}. In low temperature range, $T \leq 10$ K, a T^2 dependence of χ values was shown. Above a characteristic temperature, T^*, a Curie-Weiss behaviour was evidenced. Thus, the nickel, at 0 K, has a weak moment or shows an enhanced magnetic susceptibility. In the high temperature range, the linear χ^{-1}vsT dependences suggest the presence of localized nickel moments. The above behaviour may be analyzed in models, which take into account the electron correlations effects in d-band, as spin fluctuation model [6] or dynamical mean field theory [26]. These models reconcile the dual character of electron, which as particle requires a real space description and as a wave, a momentum space description. The spin fluctuation model considers the balance between the frequencies of longitudinal spin fluctuation, which are determined by their lifetime and of transverse fluctuations, which are of thermal origin. These effects lead to the concept of temperature induced moment. For a weak ferromagnet as Ni in $RNi_{5-x}M_x$ (R = Nd, Tb, Dy) with $x \leq 1$ or an exchange enhanced paramagnet as for compositions $x \geq 2$ or Ni in $LaNi_{5-x}M_x$ (M = Cu, Al), systems, the wave number dependent susceptibility, χ_q, has a large enhancement due to electron-electron interaction for small q-values. The χ_q shows a significant temperature dependence only for q values close to zero. The average amplitude of spin fluctuations $\left\langle S_{loc}^2 \right\rangle = 3k_B T \sum \chi_q$ increases with temperature and reaches an upper limit at a temperature T^*. For $T > T^*$, a Curie-Weiss behaviour is predicted, similar as in systems having local moments. The moments are localized in q-space. If the spin fluctuations are saturated, feature, which characterizes the systems having high exchange enhancement factors or are weak ferromagnets, the effective moments reflect the electronic configuration of the given 3d ion. The effective nickel moments in RNi_5 are somewhat lower ($\cong 2.15 \mu_B$) than the value expected for Ni^{2+} ion ($2.82 \mu_B$). This decrease may be attributed to the diminution of electron correlations due to 3d-5d hybridization. We note that in spin fluctuation model, the effective Ni moments and those obtained at 0 K are not correlated [6].

The magnetic behaviour of nickel in the studied compounds, may be also analyzed in the dynamical mean field theory DMFT [26] combined with the standard LDA band calculations (LDA + DMFT) [27]. In a strongly correlated system, leading Curie-Weiss behaviour, at high temperatures, is predicted. For an itinerant electron system, the time dependence of the correlation function results in a temperature dependence of $\left\langle S_{loc}^2 \right\rangle$.

Fluctuating moments and atomic-like configurations are large at short time. The moments are reduced at larger time scales, corresponding to a more band like less correlated electronic

structure near the Fermi level. By using a numerically exact quantum scheme, in the LDA + DMFT, it was possible to reproduce the 6 eV satellite in DOS spectrum of nickel at $T = 0.9T_c$. This satellite was shown to have substantially more spin-up contribution. The diminution of the 6 eV satellite intensity, as evidenced by XPS measurements, in samples where Ni was substituted by Al or Cu is in agreement with partial filling of Ni3d band due to hybridization effects. The above data are also in agreement with magnetic measurements which show a decrease of the effective nickel moments when increasing the content of substituting elements.

7. Conclusions

The $RNi_{5-x}Cu_x$ series with R = La, Nd form solid solutions having $CaCu_5$ type structure in the composition range $x \leq 2.5$. In $RNi_{5-x}Al_x$ systems with R = La, Tb, Dy, the structure changes to $HoNi_{2.6}Ga_{2.4}$ type for $x \geq 2$.

Band structure calculations on RNi_5 compounds with magnetic rare-earths show the presence of nickel ordered magnetic moments at both 2c and 3g sites. The nickel moments are antiparallel aligned to rare-earth for R = Tb, Dy and parallel oriented for R = Nd. The values of the nickel moments were correlated with their local environments. The nickel moments decrease when replacing Ni by Cu or Al and are practically nil for $x \geq 2$. Above the magnetic ordering temperatures, Curie-Weiss dependences were shown. The Curie constants are higher than those of free R^{3+} ions suggesting the presence of nickel contributions. The effective nickel moments decrease when increasing Al or Cu content, but have finite values in the whole studied composition range.

The $LaNi_{5-x}Cu_x$ and $LaNi_{5-x}Al_x$ compounds, where La is not magnetic, show at low temperatures ($T \leq 10$ K), a T^2 dependence of the magnetic susceptibilities χ. The χ values obtained from band structure calculations agree with those experimentally determined at 1.7 K. Above a characteristic temperature T^*_g, a Curie-type contribution is evidenced. The effective nickel moments follow the same composition dependence as that evidenced in compounds with magnetic rare-earths. The XPS studies, at room temperature, show in all cases the presence of 6 eV satellite suggesting that there are unoccupied Ni d states, the intensity of the satellite decreasing when increasing the content of substituting elements. The magnetic behaviour of nickel is described in models, which take into account the electron correlation effects in d bands as spin fluctuation model or dynamical mean field theory.

References

[1] E. Burzo, A. Chelbowski and H.R. Kirchmayr, Landolt Börnstein Handbuch, vol. III/19d2, Springer Verlag, (1990)
[2] D. Gignoux, D. Givord and A. del Moral, Solid State Commun. 19, 891 (1976)
[3] E. Burzo, L. Chioncel and I. Costina, Mat. Sci. Forum 373-376, 669 (2001)
[4] E. Burzo, S.G. Chiuzbaian, L. Chioncel and M. Neumann, J. Phys.: Condens. Matter 12, 5897 (2000)
[5] E. Burzo, V. Pop and I. Costina, J. Magn. Magn. Mater. 157-158, 615 (1996)
[6] T. Moriya, J. Magn. Magn. Mater. 100,201 (1991)
[7] E. Burzo, T. Crainic, M. Neumann, L. Chioncel and C. Lazar, J. Magn. Magn. Mater. (in press)
[8] J.L. Bobet, S. Pechev, B. Chevalier and B. Darriet, J. Alloys Compounds 267,136 (1998)
[9] S. Sorgic, A. Dasner and Z. Blazine, J. Phys.: Condens. Matter. 7, 7209 (1995)

[10] E. Burzo, S.G. Chiuzbaian, M. Neumann, M. Valeanu, L. Chioncel and I. Creanga, J. Appl. Phys. 92,7362 (2002)

[11] E. Burzo, S.G. Chiuzbaian, M. Neumann and L. Chioncel, J. Phys.: Condens. Matter. 14, 8057 (2002)

[12] O.K. Anderson, Phys. Rev. B12, 3060 (1975)

[13] O.K. Anderson and O. Jepsen, Phys. Rev. B53, 2571 (1984)

[14] O.K. Anderson, O. Jepsen, and D. Glötzel, Highlights of Condensed Matter. Theory, Ed. F. Bassani, F. Fumi and M.P. Tossi, New York, North-Holland, 1985

[15] R.O. Jones and O. Gunnarson, Rev. Mod. Phys. 61, 689 (1989)

[16] U. von Barth and L. Hedin, J. Phys. C.: Solid State Phys. 5, 1629 (1972)

[17] V.I. Anisimov, J. Zaanen and O.K. Anderson, Phys. Rev. B44, 943 (1991); A.I. Lichtenstein, J. Zaanen and V.I. Anisimov, Phys. Rev. B52, R 5467 (1995)

[18] V.I. Anisimov, I.V. Solovyev, M.A. Korotkin, T.H. Cyzyk and G.A. Sawatzky, Phys. Rev. B48, 16929 (1993)

[19] V.I. Anisimov, F. Aryasetiavan and A.I. Lichtenstein, J. Phys.: Condens. Matter. 9, 767 (1997)

[20] E. Burzo, Solid State Commun. 14, 1295 (1974)

[21] E. Burzo, A. Takacs, M. Neumann and L. Chioncel, Phys. Stat. Solidi (in press)

[22] M.T. Béal-Monod, Physica B 139-140, 1837 (1982)

[23] B. Vincent Crist, Handbook of Monochromatic XPS Spectra, vol. I, XPS International Inc., 1999

[24] J.K. Lang, Y. Bauer and P.A. Cox, J. Phys. F.: Metal Phys. 11, 121 (1981)

[25] I.A. Campbell, J. Phys. F.: Metal Phys. 2, L149 (1972)

[26] A. Georges, G. Kothar, W. Krauth and M.J. Rosenberg, Rev. Mod. Phys. 68, 13 (1996)

[27] A.I. Lichenstein, M.I. Katsnelson and G. Kothar, Phys. Rev. Letters 87, 672205 (2001)

THERMOELECTRIC EFFECTS IN ALLOYS Bi-Sn

P. Bodiul, O. Botnari, E. Moloshnik, Gh. Para, V. Ciorbă

Institute of Applied Physics, Academy of Sciences of Moldova, Academiei str.,5, Chisinau, MD-2028, Republic of Moldova

Changes of thermopower temperature changes (77-300 K) in bulk Bi-Sn crystals and thermopower of wire crystals Bi-0,07 at%Sn and Bi-0,05at%Sn were measured from the liquid helium temperature to the room one. The dependence $\alpha^2\sigma$ on temperature for both bulk and wire samples is given.

Introduction

Wide possibilities of practical use of thin (with the thickness $10^{-4} \div 10^{-5}$ cm) wire crystals in various devices and apparatus favour their comprehensive experimental and theoretical research. In thin wire crystals there appears a number of specific effects, which are not observed in bulk samples and even in films. These effects are determined by the electron movement limitation in two directions of wire crystal. The electron state in the wire crystal due to the limitation of the latter in two directions is determined by two discrete and one continuous quantum numbers. Therefore, quantum size effects in a sense are analogous to the phenomena characteristic of bulk crystal located in the magnetic field.
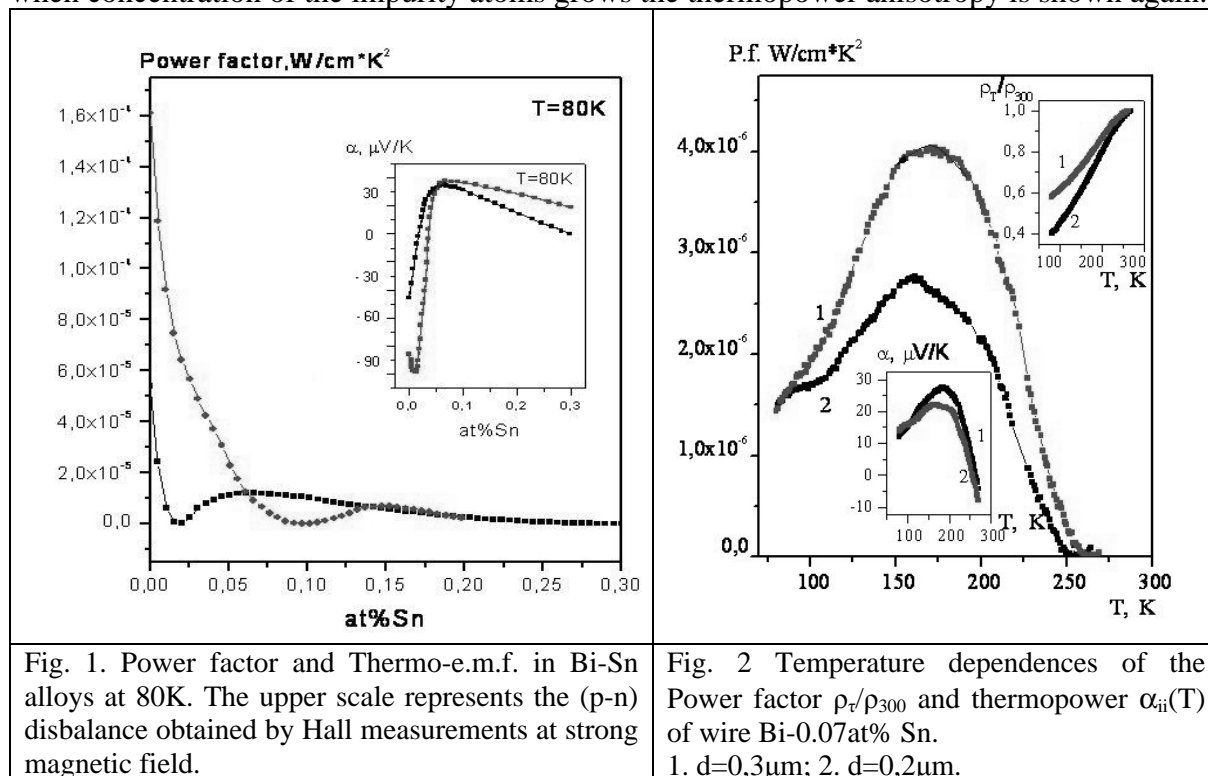
Experiment and Discussion of Results

Single crystal samples of alloys Bi-Sn were grown by the multiple zone recrystallization. Homogeneity of the impurity distribution along the sample was controlled by the microroentgen phase analysis. Maximal deviation of the sample composition from the set one does not exceed 10%. Samples of rectangular form (10x3x4 mm) were placed into a cryostat for measurements between two bulk copper blocks, with a furnace wound on one of them for creation of the temperature gradient ΔT. The temperature gradient along the sample is determined with the help of copper constantan thermocouples soldered to butt-ends of the blocks.

We measured the thermopower on glass insulated Bi-Sn whiskers with diameter of $\geq 0,3\mu m$ in the temperature range 80-300K. The crystals were obtained by liquid phase casting by the Ulitovsky method [5]. The crystal diameter was measured by the optical microscope MIM-8 (1350 x) with precision of about $0,1\mu m$. The crystal length was 4-5 μm, it was measured by a MI-1 microscope with precision of about $20\mu m$.

Electrical and thermal contacts were formed by In-Ga eutectics. The X-ray analysis proved the monocrystallinity of all the whiskers with preferential <4041> orientation (in hexagonal peaking) along a whisker axis. The third order axis (C_3) is inclined to the whisker axis at the angle of about 80º, and one of the second order axes (C_2) is at right angle to the whisker axis. With respect to the orientation of crystallographic axes such whiskers are similar to bulk crystals of the second type (the crystal axis coincides with the bisector axis C_s).

Fig. 1 shows the concentration dependence α_{11} and α_{33} for bulk Bi-Sn samples at 80 K. When the doping degree increases both components of the thermopower tensor decrease in

the absolute value, pass through zero and achieve maximal positive value $\alpha_{11}=\alpha_{33}=40$ μV/degree. In this region the thermopower is approximately isotropic, however when concentration of the impurity atoms grows the thermopower anisotropy is shown again.

Fig. 1. Power factor and Thermo-e.m.f. in Bi-Sn alloys at 80K. The upper scale represents the (p-n) disbalance obtained by Hall measurements at strong magnetic field.	Fig. 2 Temperature dependences of the Power factor ρ_τ/ρ_{300} and thermopower $\alpha_{ii}(T)$ of wire Bi-0.07at% Sn. 1. d=0,3μm; 2. d=0,2μm.

Further doping leads to the thermopower sign inversion and disappearance of the thermopower (at the carrier concentration $1,7 \bullet 10^{19}$ cm^{-3}). At the carrier concentration $2,5 \bullet 10^{19}$ cm^{-3} the thermopower component α_{33} achieves its maximal negative value, and the thermopower anisotropy appears again.

Fig. 2 shows temperature dependences of thermopower $\alpha(T)$ for different concentrations of Sn in the wire and fig. 1 shows the temperature dependence of Power factor in the Bi-0,07at%Sn wire with different diameter: 1. d=0,3μm; 2. d=0,2μm.

For explanation of thermopower behavior in weakly doped alloys Bi-Sn the thermopower was theoretically calculated taking into account the phonon drag effect,

This effect was taken into account due to peculiarities of the thermopower temperature change. They are shown at low temperatures, when as it is known favourable conditions for the phonon drag effect manifestation are created [1]. The phonon component in the thermopower in both non-degenerated semiconductors and semimetals may exceed the diffusion component by hundreds and even thousands times. In [2] it is shown that these results are true for space-limited crystals too.

Numerical calculation of the thermopower dependences on temperature and diameter in bismuth wire crystals shows that all the peculiarities of behaviour of $\alpha(T)$ and $\alpha(d)$ at low temperatures are determined by the phonon drag effect. At low temperatures (T<30 K) the phonon drag effect contribution to the thermopower is significant. At the presence of the temperature gradient in the sample the phonon drift from the hot end to the cold one takes place. Existence of this drift leads to the fact that electrons and holes being scattered on phonons obtain additional energy along the phonon drift. The energy of the current carriers obtained from the directed flow of phonons is considerably higher than their diffusion energy along the wire.

For a valuable analysis of thermoelectric efficiency $Z = \dfrac{\alpha^2 \sigma}{\xi}$ it is necessary to know heat conductivity ξ. However, measurement of heat conductivity in wires of bismuth and its alloys is a complicated and labour-consuming problem, which is not solved yet. Available data for bulk crystals of various sizes show that heat conductivity decreases with size reduction [6].

Peculiarities of the temperature dependence $\alpha_{ii}(T)$ in thin wires can be qualitatively understood in the frames of simplified classical approximations. As it is known, when two types of the charge carriers are available for bulk bismuth crystal:

$$\alpha_{ii}(T) = \frac{\alpha_0^h \sigma_{ii}^h + \alpha_0^e \sigma_{ii}^e}{\sigma_{ii}^e + \sigma_{ii}^h} \quad ,$$

where $\alpha_0^{h,e}$ are partial thermopowers of electrons and holes, and $\sigma_{ii}^{e,h}$ are their partial electric conductivities.

As it is seen from the Figure, single crystal wires of bismuth doped with tin at the temperatures below 200 K may be used as a material for p-branch with the parameters close to those of bulk bismuth.

Changing the wire diameter and the doping degree one can shift the interval of maximal value of $\dfrac{\alpha^2 \sigma}{\xi}$ from (30-50) K in pure bismuth wires to (130-220) K in alloys Bi-0,07at%Sn.

References

[1] A.L. Natadze, A.L. Efros, Vlianie vzaimnogo uvelicenia electronov i fononov na termoeds i efect Nernsta, FTT, 1962, vip. 10, ctr. 2931-2939.
[2] L.E. Gurevici, I.I. Korenblit, Vlianie uvelicenia elektronov i ih vzaimnogo uvlecenia na kineticeskie koefitienti polumetalov , FTT, 1964, 6, vip. 3, str. 856-863.
[3] M.E. Kuznetov, S.S. Shalit, Fononoe uvlechenie v vismute – Pisima v JETF, 1967, 6, vip. 7, str. 745-747.
[4] E.S. Medvedev, V.N. Kopilov, L.P. Mejov-Degmin, Vlianie effecta vzaimnogo uvlecenia na kineticeskie koefitienti vismuta pri nizkih temperaturah – FTT, 1975, 1, vip. 9, str. 1192-1202.
[5] E.Ya. Badinter, N.R. Berman, I.F. Drobenko, Litoi mikroprovod I ego svoistva, Shtiinta, Kishinev, 1973.
[6] A. Balandin, K.L. Wang, J. Appl. Phys., (1998), v.84, p.6149.

NONUNIFORM SUPERCONDUCTING STATE IN SUPERCONDUCTOR/FERROMAGNET NANOSCALE LAYERED SYSTEM

A. Prepelitsa, V. Zdravkov, E. Molchanova, A. Sidorenko

Institute of Electronics Engineering and Industrial Technologies ASM, MD-2028, Chisinau, Republic of Moldova

Superconducting Nb/Ni bilayers, prepared by magnetron sputtering are investigated in the range of temperatures 1.3-10K. For specimens with constant Nb layer thickness a non-monotonic behavior of the critical temperature upon increasing of the Ni layer thickness with distinct oscillations of $T_c(d_{Ni})$ of the Ni layer is found. The results are interpreted in terms of Larkin-Ovchinnikov-Fulde-Ferrell (LOFF) inhomogeneous superconducting state in the ferromagnetic Ni layer.

Introduction

The coexistence of two antagonistic orderings, superconductivity (SC) and ferromagnetism (FM), seems to be very doubtful, because SC requires Cooper-pairing between electrons with antiparallel spin, whereas FM favors a parallel alignment of the electron spins. Nevertheless, the coexistence of both phenomena was theoretically considered by A. Larkin, Yu. Ovchinnikov, and P. Fulde, R. Ferrell [1,2]. Under strong restricted conditions for the exchange field,

$$0.71\Delta_0 < E_{exc} < 0.76\Delta_0 \tag{1}$$

where Δ_0 is the superconducting gap, they predicted an nonuniform superconducting state in the ferromagnet with a spatially modulated pair amplitude and nonzero pairing momentum, δp. This state, called „3D-LOFF state", is very difficult to realize experimentally because the value of the exchange field for most ferromagnets is much higher than Δ_0 ($E_{exc}\sim$ 1000 K, $\Delta_0 \sim$ 10K) .
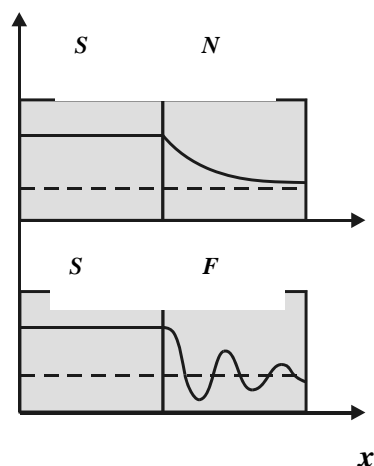

Figure 1. Proximity effect in a superconductor/normal metal (S/N) bilayer with an exponential decay of pairing function, $F_F \sim e^{-x/\xi_N}$ in the N-layer, and in a proximity coupled superconductor/ferromagnet (S/F) bilayer with oscillating $F_F \sim cos(x/\xi_F)$ within the F-layer.

A more realistic system for observation of LOFF-like state was proposed by A. Buzdin and Z. Radovich [3,4] - a planar geometry, i.e. S/F layered system, where a quasy-1D LOFF-like state can appear. They proposed to separate superconductor and ferromagnet, then the strict limitation (1) for the exchange field will be not important. Such "proximity-coupled" S/F system is shown in Fig.1. For an S/N- proximity coupled system a monotonous decrease of the paring function, F, within the N-layer [5] leads to a monotonous decrease of the critical temperature of the S/N bilayers with the N-layer thickness increasing, as was confirmed in a lot of experimental works. In contrast to S/N systems, for the S/F coupled bilayers a very unusual phenomenon was predicted by A.Buzdin: an oscillating dependence of T_c as a function of the magnetic layer thickness, d_F. Due to the proximity effect, Cooper pairs diffuse from S-layer into the ferromagnetic layer where are subjected to the exchange field. A maximum of $T_c(d_F)$ occurs when the period of the Usadel function describing the pair amplitude, F, matches the thickness of the ferromagnetic layer. Further theoretical investigations [6] predict different behavior of $T_c(d_F)$: from a monotonic suppression of T_c and its saturation at some d_F up to re-entrant superconductivity depending on the interface transparency. In spite of the well developed theory of S/F layered systems, there exist only a few experimental investigations of $T_c(d_F)$ with reliable oscillations of $T_c(d_F)$ observed (see [7] and the References therein). Crucial difficulties arose in these experiments. We consider in the present work the experimental conditions necessary for reproducible observation of the LOFF-like 1D superconducting state in S/F layered system with distinct T_c-oscillations.

Sample preparation and characterization

Among different possible S/F–couples for sample preparation we have chosen Nb and Ni. The reason of the choice was a very small mutual solubility of these two metals, less than 4 at.% at ambient conditions [8], what leads to obtaining of a well resolved clean S/F-interface. On the other hand, we did not take absolute immiscible metals, like Nb and Gd, which could give an island-like growth of the F-layer and as a result, a poor quality rough S/F interface. The Nb/Ni samples have been prepared by DC magnetron sputtering on flame-polished glass substrates kept at room temperature. Pure Nb (99,99%, ') and Ni (99,99%) were used as sputtering targets.
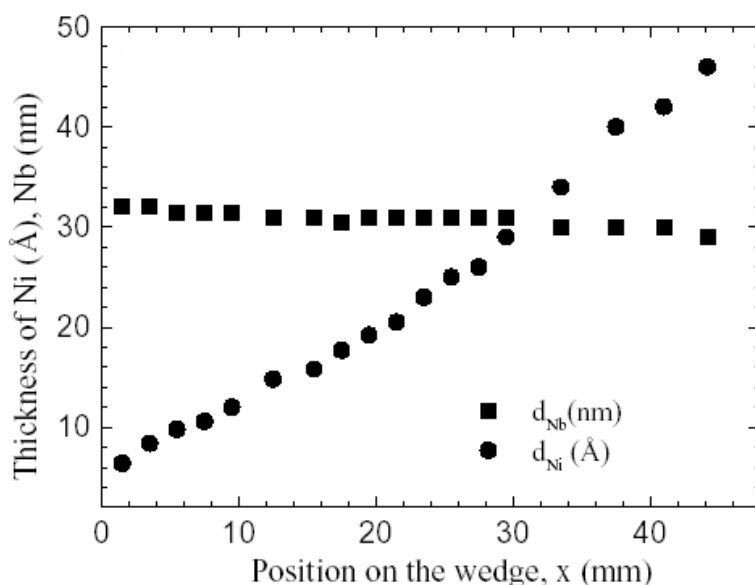

Figure 2. The results of RBS measurements for the thickness of Nb and Ni layers (sample set from Nb/Ni-wedge with d_{Nb}=const=31nm, d_{Ni}=variable).

The glass substrate of 10x75 mm^2 was put into the chamber symmetrically with respect to the centrum of the Nb target. Then, a wedge-shaped Ni layer was deposited by shifting the substrate away from the symmetry axis of the Ni target. The resulting wedge sample was cut across the wedge to 1.5 mm wide strips using a diamond cutter. Following this routine we obtained a batch of Nb/Ni samples with constant Nb layer thickness and variable Ni layer thickness. Platinum 50-μm wires were attached by silver paste for four-contact resistance measurements.

The X-ray small angle reflectivity scans (2θ <10^0, CuK$_\alpha$ radiation) were used to determine the layer roughness. Well resolved weakly damped oscillations of the reflectivity as a function of the angle with more than 15 periods of oscillations were detected, giving the evidence of high quality of the layers with smooth surfaces and interfaces. For a quantitative analysis of the X-ray data we used a simulation program, based on the Parratt formalism [9]. Fitting of the X-ray data gives the value of the layer thickness and the roughness σ$_{rms}$ as the mean square deviation of the layer thickness from an "ideally" smooth layer, the value of σ$_{rms}$ for the investigated samples was less than 0.3 nm.

For the precise thickness measurements we used Rutherford backscattering spectrometry, giving the possibility to determine the absolute thickness of Ni layers at the level of 1 nm with an accuracy of 0.03 nm. Details of the RBS measurements are described in [7]. The results of thickness determination by RBS for one of investigated Nb/Ni-wedge samples are presented in Fig.2.

Results and discussion

Resistive transitions for one batch of the Nb/Ni specimens are presented in Fig.3. The width of transition (0.1R$_N$-0.9R$_N$ criteria) for all investigated samples was less than 0.1 K, what allows determination of the critical temperature from the midpoint of the resistive transitions with a necessary accuracy. Figure 4 shows the dependence of the superconducting critical temperature T_c on the thickness of the ferromagnetic Ni layer for the samples with the thickness of Nb layer fixed at 31 nm. The critical temperature drops sharply when increasing d_{Ni} up to 1.2 nm, then it passes through a minimum and increases till the thickness d_{Ni} approaches ∼ 2.5 nm.
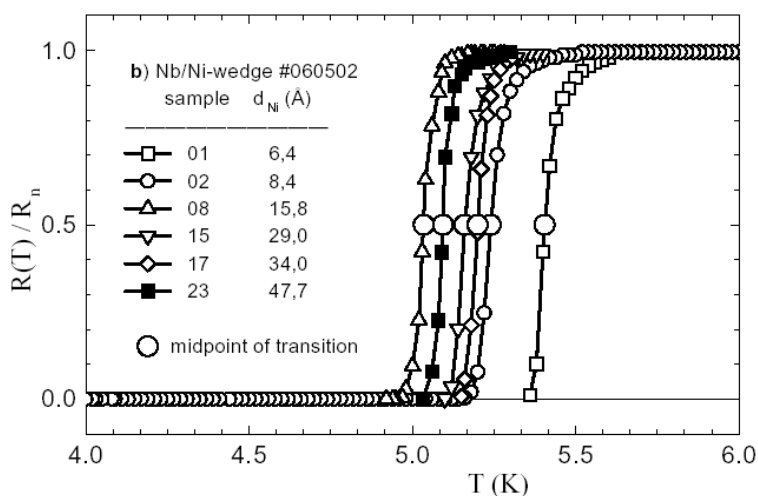

Figure 3. The resistive transitions R(T) normalized to R$_n$=R(T=10 K) for some of the measured samples from Nb/Ni-wedge with d$_{Nb}$=const=31 nm, d$_{Ni}$=variable.

T_c (d_{Ni}) demonstrates an oscillatory behavior as a function of the Ni layer thickness. This oscillatory behavior is the evidence of the 1D-LOFF-like superconducting state in the investigated Nb/Ni samples.

As it was mentioned above, the proximity effect in S/F system has a crucial difference from that of the superconductor/normal metal (S/N) system. In a usual S/N system the pairing function exponentially relaxes deep into the N-layer on the scale of the coherence length $\xi_N = (\hbar D_N /2\pi k_B T)^{1/2}$, here D_N is the diffusion constant of the normal metal, k_B is the Bolzman constant. In S/F layered system, in contrast to S/N proximity coupled layers, the pairing function in a pure ferromagnet ($l_F > \xi_F$) oscillates on a distance of the magnetic coherence length, $\xi_F = (\hbar v_F /E_{ex})$, and relaxes deep into the F-layer on the scale of electron mean free path, l_F. In strong ferromagnets like Ni, Fe the oscillation period of the pairing function can be a few times shorter than the decay length l_F. If the thickness of the F-layer is smaller than or comparable to the l_F, the weakly damped pairing function wave incident on the S/F interface, will interfere with the wave reflected from the opposite surface of the F-layer. Using an analogy with light, the F-layer works like a Fabry-Perot interferometer, which can be highly reflective or almost transparent depending on the relation between the wavelength and the thickness of the interferometer. Thus, due to the interference, the pairing function flux will be modulated as a function of ferromagnet layer thickness d_F. As a result, the coupling between S and F layers is modulated, and the
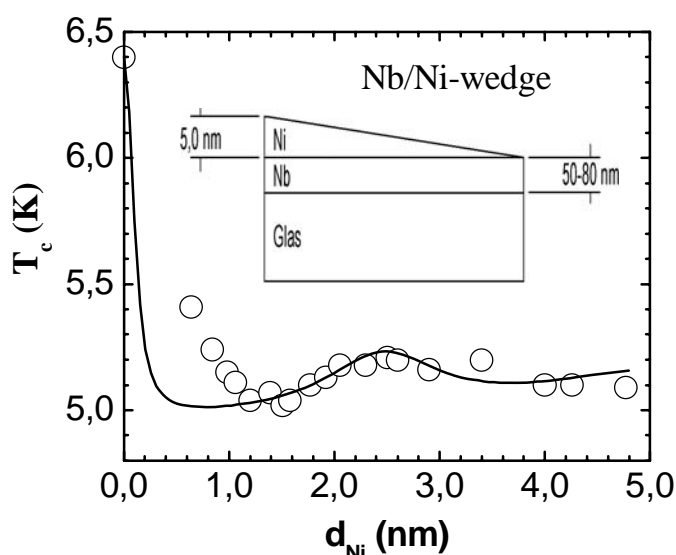
Figure 4. The dependence of the superconducting transition temperature T_c on the Ni layer thickness d_{Ni} for the sample set from the Nb/Ni-wedge with $d_{Nb} =31$ nm. The solid line demonstrates the best fit by the theory [6], the solid line is calculated using the parameters: $T_{c0} =6.4$ K, ξ_{BCS}(Nb)=42 nm, $\xi_S =6.2$ nm, $(N_F v_F)/(N_S v_S) =0.51$, $\xi_F/l_F =0.5$, $T_F =2.0$, $\xi_F =0.88$ nm.

superconducting T_c oscillates as a function of d_F. We have observed this type of oscillations in investigated Nb/Ni samples. For the quantitative comparison with the S/F-proximity theory we used the model developed by L. Tagirov [6] for bilayers with a finite S/F interface transparency T_F. In frame of the theory [6] superconducting transition temperature of the S/F-sandwich can be determined as a solution of equation

$$\ln t_c + Re\,\psi\,(1/2 + \rho/t_c) - \psi(1/2) \ , \qquad (2)$$

where $Re\,\psi$ is the real part of the digamma function, $t_c = T_c/T_{c0}$ is the reduced transition temperature, T_{c0} is the transition temperature of single superconducting layer . Here the complex-valued pair-breaking parameter ρ is defined as $\rho = (\ k_S\xi_S)^2/2,\ $ and k_S is the wave number of the pairing function propagation in the S-layer, which satisfy to the solution of equation:

$$(k_S d_S) tan(k_S d_S) =$$
$$= (N_F v_F d_S \xi_{BCS})/N_S v_S \xi_S^2)[tanh(k_F d_F)/\{(1-i\xi_F/l_F)^{1/2} + (2/T_F)tanh(k_F d_F)\ \}] \qquad , \qquad (3)$$

where N_F, N_S are the density of states at the Fermi level in F and S layers, respectively, v_F, v_S is the Fermy velocity, $\xi_{BCS} = (1.78\hbar v_S)/(\pi^2 k_B T_{c0})$, $\xi_S=(2/\pi)\xi_{GL}(0)$, Ginzburg-Landau coherence length $\xi_{GL}(0)$ is determined from the slope of the upper critical field, $\xi_{GL}(0)=[(-dB_{c2}(T)/dT)(2\pi T_c/\phi_0]^{-1/2}$, and T_F is the quantum mechanical interface transparency parameter, which equals infinity for the perfectly transparent S/F interface, or is equal to zero for the completely reflecting interface. It takes into account the reflection of electrons from the interface caused by a mismatch of the Fermi momentum of the contacting metals.

According to the S/F proximity theory [6] three main regimes for T_c behavior can be observed in S/F bilayers depending on the thickness of the superconducting layer: a) for a large thickness, $d_S >> \xi_S$ the superconducting T_c can oscillate as a function of the ferromagnetic layer thickness d_F [7]; b) for a thinner superconducting layer, when $T_c \sim (0.2\text{-}0.3)T_{c0}$ the regime of re-entrant superconductivity can be realized (preliminary attempt of such behavior reported in [10]); c) for thinner superconducting layers the superconducting T_c falls down to zero upon increasing d_F.

One can conclude, that our experimental data belong to the regime a), demonstrating distinct oscillations of T_c (d_F). Fitting of the experimental results to the S/F-proximity effect theory [6], shown by solid cure in Fig.4 (with mediate value of the adjust parameter of interface transparency $T_F = 2.0$), shows a rather good agreement in the relevant range of Ni layer thickness above 1nm, but there is a deviation in the range of small thickness below 1 nm. The possible reason responsible for this deviation may be the existence of the magnetically "dead" layer at the S/F interface. As demonstrated in [11] the Nb/Fe couple always has an interdiffused layer at the S/F interface, which is magnetically indifferent, i.e. the local magnetic moment disappears when increasing the number of Nb neighbors surrounding the Fe ion in the cluster. The same physical picture is realized also in V/Fe couples [12]. A magnetically "dead-layer" has also been observed at the V/Ni interface [13], where the vanishing of the Ni layer magnetic moment at d_{Ni} below 1 nm has been declared. Finally, from a detailed study of Nb/Ni multilayers prepared by magnetron sputtering on a sapphire substrate [14] the authors concluded that below a Ni layer thickness of 1.4 nm the magnetic momentum in the Ni layer disappears due to the interdiffusion of Nb - Ni and no ferromagnetic order is present. This thickness is close to the thickness of $d_{Ni} \sim 1.0$ nm in our study (see Fig.4), where the theory deviates from the experimental points. The suppression of superconductivity by a nonmagnetic dead-layer is weaker than by ferromagnetic Ni, and $T_c(d_{Ni})$ decreases slowly which meets our experimental observation.

Conclusion

The proximity effect in Nb/Ni bilayers prepared by DC magnetron sputtering on smooth glass substrates was investigated. We observed distinct oscillations of the superconducting critical temperature for specimens with constant Nb layer thickness upon increasing the thickness of the Ni layer as an evidence of 1D-LOFF- like inhomogeneous superconducting

pairing in the ferromagnetic Ni layer. We can formulate the necessary conditions for experimental realization of the 1D-LOFF like state in S/F layered structures:

- The sputtering technique with a high deposition rate has advantages in comparison with MBE process to fabricate S/F samples showing oscillating behaviour of $T_c(d_F)$;
- The S/F couples should not consist of immiscible metals, but of metals with restricted solubility and narrow composition ranges of intermetallic compound formation for obtaining of a smooth S/F interface;
- The substrate quality and deposition rate should ensure the S/F interface roughness less than the F-layer thickness.

S/F layered system prepared under those conditions will demonstrate 1D-LOFF-like superconducting state.

Acknowledgements

References

[1] A.I. Larkin, and Yu.N. Ovchinnikov, Nonuniform State of Superconductors, *Zh.Eksp.Teor.Fiz.* 47,1136-1146, (1964).

[2] P. Fulde, and R. Ferrell, Superconductivity in a Strong Spin-Exchange Field, *Phys.Rev.* 135, A550-A563, (1964).

[3] A.I. Buzdin, and L.N. Bulaevskii, Critical current oscillations as a function of the exchange field and thickness of the ferromagnetic metal (F) in an S-F-S Josephson junction, *Pis'ma Zh.Eksp.Teor.Fiz.* 35, 147-148, (1982).

[4] Z. Radovic, L. Dobrosavljevic-Grujic, A.I. Buzdin, and J. Clem, Upper critical fields of superconductor-ferromagnet multilayers, *Phys.Rev.*B38,2388-2393, (1988).

[5] P.G. de Gennes, Boundary Effects in Superconductors, *Rev.Mod.Phys.*36, 225-237, (1964).

[6] L.R. Tagirov, Proximity effect and superconducting transition temperature in superconductor/ferromagnet sandwiches, *Physica* C 307, 145-163, (1988).

[7] A.S. Sidorenko, V.I. Zdravkov, A.A. Prepelitsa, C. Helbig, Y. Luo, S. Gsell, M. Schreck, S. Klimm, S. Horn, L.R. Tagirov, and R. Tidecks, Oscillations of the critical temperature in superconducting Nb/Ni bilayers, Ann.Phys.(Leipzig) 12, 37-50, (2003).

[8] Th.B. Massalski, (ed.-chief), *Binary Alloy Phase Diagrams*, ASM International, Materials Park, Ohio, (1990).

[9] L.G. Parratt, Surface Studies of Solids by Total Reflection of X-Rays, *Phys.Rev.* 95, 359-369, (1954).

[10] L.R. Tagirov, I.A. Garifullin, N.N. Garif'yanov, S.Ya. Khlebnikov, D.A. Tikhonov, K.K. Westerholt, and H. Zabel, Re-entrant superconductivity in the V/Fe superconductor/ferromagnet layered system, *J. of Magnetism and Magnetic Materials* 240, 577-579, (2002).

[11] Th. Mühge, K. Westerholt, H. Zabel, N.N. Garifyanov, Yu.V. Goryunov, I.A. Garifullin, and G.G. Khaliullin, Magnetism and superconductivity of Fe/Nb/Fe trilayers, *Phys. Rev. B* 55, 8945-8954, (1997).

[12] J. Izquiero, R. Robles, A. Vega, M. Talanana, and C. Demangeat, Origin of dead magnetic Fe overlayers on V(110), *Phys. Rev. B* 64, 060404-1-060404-4, (2001).

[13] H. Homma, C.S.L. Chun, G.G. and I.K. Zheng, I.K. Schuller, Interaction of superconductivity and itinerant-electron magnetism: Critical fields of Ni/V superlattices, *Phys. Rev. B* 33, 3562-3565, (1986).

[14] J.E. Mattson, R.M. Osgood III, C.D. Potter, C.H. Sowers, and S.D. Bader, Properties of Ni/Nb magnetic/superconducting multilayers, *J. Vac. Sci. Technol.* A15, 1774-1779, (1997).

FLAT FLUIDICS: PROGRAMMABLE ON-CHIP NETWORKS FOR BIOLOGICAL AND CHEMICAL APPLICATIONS

A. Wixforth[1], Ch. Strobl[1], Ch. Gauer[2], A. Toegl[2], J. Scriba[2] and Z.V.Guttenberg[2]

[1]*University of Augsburg, Experimentalphysik I, D-86159 Augsburg, Germany*
[2]*Advalytix AG, Eugen-Sänger-Ring 4, D- 85649 Brunnthal, Germany*

Surface acoustic waves are used to actuate and process smallest amounts of fluids on the planar surface of a piezoelectric chip. Chemical modification of the chip surface is employed to create virtual wells and tubes to confine the liquids. Lithographically modulated wetting properties of the surface define a fluidic network, in analogy to the wiring of an electronic circuit. Acoustic radiation pressure exerted by the surface wave leads to internal streaming in the fluid and eventually to an actuation of small droplets along predetermined trajectories. This way, in analogy to microelectronic circuitry, programmable biochips for a variety of assays on a chip have been realized.

1. Introduction

The knowledge of the biochemical interior of living cells steadily increases and researchers dig deeper and deeper into the biomolecular world. Now the human genome is sequenced, scientists hope to find novel drug targets once the code is cracked. Analytical techniques like gene expression analysis or cell assays have become standard tools, used in large scale screening for new drugs. The very same technologies are the driving force behind a miniaturization of the laboratories, as parallel screening requires smallest amounts of sample for the single experiments. The resources of many of the precious ingredients are either very limited or prohibitively expensive.

In this article, we wish to report a novel way of tackling the need to scale chemical and biological laboratories down to the size of a thumbnail. We describe a technique which uses virtual beakers and channels to confine smallest amounts of liquids to the plane surface of a microchip, and tiny earthquakes (Surface Acoustic Waves, SAW) on this very chip to act as electrically adressable and programmable nanopumps. The combination of both can be viewed as a step towards the realization of a programmable microfluidic processor.

2. Experimental Details

2.1. Surface Acoustic Waves

Surface acoustic waves have been first described in combination with earthquakes [1]. Meanwhile, reduced to the significantly smaller nano scale, they found their way into much friendlier fields: SAW devices are widely used for RF signal processing and filter applications and became a huge industry in mobile communication [2]. SAW devices have been around for years in communication circuitry – every cell phone has filters using the effect. An electrical

signal fed into so-called transducers on the surface of a piezoelectric chip is converted into a deformation of the crystal underneath. Given the right frequency of the signal, a mechanical wave is launched across the chip. In Fig. 1, we sketch a snapshot of a SAW propagating on a solid. The SAW in this figure is characterized by subsequent regions of compressed and expanded material as indicated in gray scale.

In the recent past, SAW have also been used to act in a completely different way than for filtering and signal processing just by converting electrical signals into mechanical vibrations and vice versa. Excited on piezoelectric substrates, they are accompanied by large electric fields. Those electric fields are travelling at the speed of sound of the substrate (approx. 3000 m/sec) having the same spatial and temporal periodicity as their mechanical companions. Charges at or close to the surface are coupling to these electric fields, and currents are induced withing a conducting layer. Nearly twenty years ago we thus introduced SAW to study the dynamic conductivity $\sigma(\omega,k)$ of low-dimensional electron systems in high magnetic fields and at low temperatures.
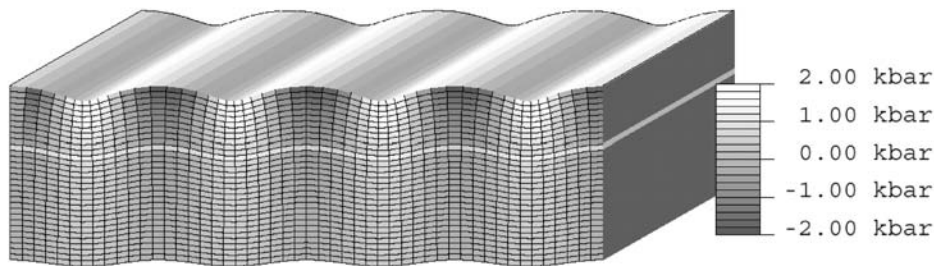

Fig. 1: Sketch of a Surface Acoustic Wave propagating on a piezoelectric substrate. Typical wavelengths are in the micrometer range, typical amplitudes less than a nanometer.

It turns out that the interaction between a SAW and the mobile charges in a semiconductor is strongest for very low sheet conductivities as they are observed, e.g., in the regime of the quantum Hall effect [3]. However, SAW can not only be used to probe the properties of quantum systems, but also to deliberately alter some of them as SAW represent a spatially modulated strain and stress field accompanied by strong electric fields in a solid, and propagating at the speed of sound. Such an interaction between SAW and the optical properties of a semiconductor quantum well led us to the discovery that photogenerated electron hole pairs in a semiconductor quantum well can be spatially separated under the influence of a SAW mediated electric field. This, in turn has an enormous impact on the photoluminescence (PL) of the semiconductor. We were able to show that the PL not only is quenched under the influence of a SAW, but also can be reestablished at a remote location on the sample and after a certain delay time [4]. Further studies include the acoustic charge transport and the creation of dynamically induced electron wires, as well as the study of nonlinear acoustic interaction with low dimensional electron systems in semiconductors [5].

However, the piezoelectric effect is usually only a small contribution to the elastic properties of a solid: Most of the energy propagating in a SAW (usually more than 95%) is of mechanical nature. Hence, not only electrical interactions as described above, but also mechanical interactions are a possible scope for experimental investigations. Having wavelengths of a few microns and amplitudes of about only a nanometer, however, the forces and electric

fields within the nanoquake are sufficient to have a macroscopic effect. Any piece of matter at the surface along the way of a SAW experiences their vibrating force: Viscous materials like liquids absorb a lot of their energy. It turns out that the interaction between a SAW and a liquid on top of the substrate surface induces an internal streaming, and, as we will point out below, at large SAW amplitudes this can even lead to a movement of the liquid as a whole.

The origin of such an acoustically induced internal streaming is depicted schematically in Fig. 2: A SAW is propagating from left to right along the x-axis. At x=0, it reaches the boundary of a liquid at the surface of the substrate. A SAW with a non vanishing amplitude in the z-direction, i.e. normal to the surface of the substrate, is then strongly absorbed by the fluid, as indicated by the decaying amplitude for positive x values.
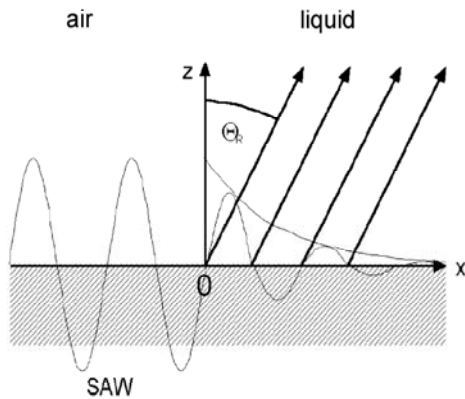

Fig. 2: Schematic illustration of the interaction between a SAW and a liquid at the surface of the SAW substrate. The SAW is propagating from left to right, and at x=0 hits the liquid. A longitudinal sound wave is radiated into the fluid under a refraction angle Θ_R.

Moreover, it creates a small but finite pressure difference $2\Delta p$ in the fluid between the ridges and the wells of the wave, which transforms into a small but finite difference $2\Delta\rho$ in the liquid density. Both quantities then spatially and temporally oscillate around their respective equilibrium value p_0, and ρ_0, respectively. The pressure difference directly above the surface of the substrate leads to the excitation of a longitudinal sound wave into the liquid. As the sound velocities for the liquid and the solid substrate are in general not equal, this wave is launched under a diffraction angle Θ_R, given by:

$$\Theta_R = \arcsin\left(\frac{v_s}{v_f}\right)$$

Here, v_s and v_f denote the sound velocities of the substrate, and the fluid, respectively. In addition, the SAW is responsible for the build-up of an acoustic radiation pressure [6]

$$P_S = \rho_0 v_S^2 \left(\frac{\Delta\rho}{\rho_0}\right)^2$$

in the direction of the sound propagation in the fluid. This leads to an internal streaming in a closed volume like a droplet, as the boundary of the droplet reflects the actuated fluid back to the source.

Such internal SAW driven streaming in a small droplet can be nicely visualized by dissolving a dried fluerescent dye under the influence of a SAW. In Fig. 3, we depict two

snapshots of such a fluorescence experiment, taken approximately one second apart from each other.
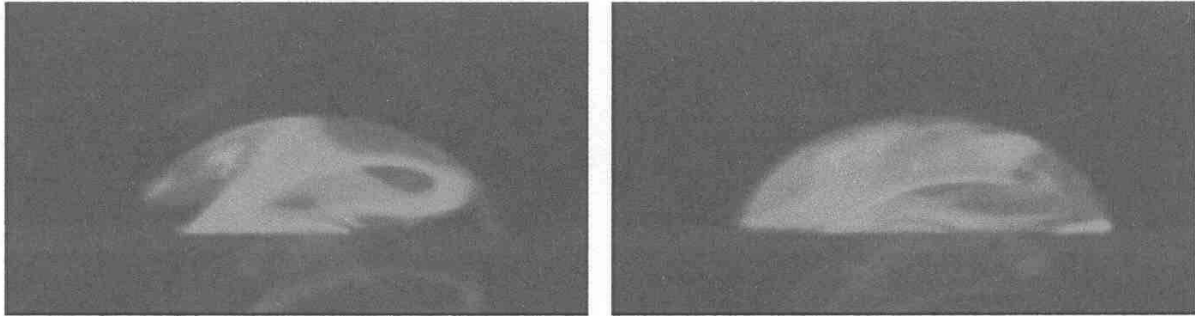

Fig. 3: SAW induced internal streaming in a small water droplet (side view, approx. 50 nl). A dried fluorescent dye on the surface of the chip is dissolved by SAW agitation, and rapidly fills the whole droplet volume.

For larger SAW amplitudes, the acoustic radiation pressure even deforms the droplet surface at the opposite side of the sound entrance. This can be seen in Fig. 4, where we show a droplet under the influence of a quite intense SAW, impinging from the left. As can be seen from the figure, the acoustic radiation pressure in this case is so high that it strongly deforms the droplet. At the same time, the wetting angles to the left and the right of the droplet (i.e. ‚luff and lee' of the SAW) are modified with respect to the equilibrium values. This acoustically driven deformation of the droplet is the main reason for the droplet actuation in our case.
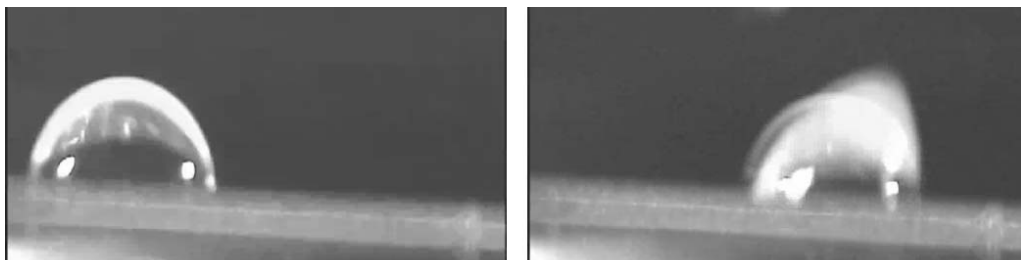
Fig. 4: Side view of a small droplet (ca. 50 nl) on the surface of a piezoelectric substrate. Left: Droplet in rest, note the wetting angle of about 90°, which has been obtained by a hydrophobic treatment of the surface. Right: droplet being „hit“ by a SAW impinging from the left. The acoustic radiation strongly deforms the droplet shape. This leads to a momentary asymmetry of the wetting angles of the droplet.

2.2.   Virtual Containers and Tracks for Liquids on a Chip

The next step towards an application of SAW in microfluidics in general is to create ‚flatland' [7] analogs to channels, tubes, reservoirs, mixing chambers and similar building blocks usually employed to guide, contain or process liquids in a fluidic network.

By a chemical modification of parts of the chip surface (e.g. silanization employing an OTS based surface chemistry) we are able to create patterns of preferred wetability (hydrophilic regions), being separated by regions of surface chemistry, where fluids are repelled (hydrophobic

areas). Employing lithographic techniques borrowed from semiconductor microelectronics, we thus can create completely flat, two-dimensional fluidic networks, where liquids are confined to virtual tracks, reservoirs and reaction chambers by surface tension alone. There is a whole variety of methods to modulate the wetting properties of the surface of a chip: the most common technique is to silanize the surface on specific areas, whereas other regions of the surface are protected by a laterally structured photo resist, that has been exposed using a mask an UV radiation and subsequently developed leaving the exposed areas etched through to the chip surface.

In Fig. 5, we depict some of such self assembled virtual potential wells for fluids on a surface. Photolithographic techniques have been employed to create ,containers' for smallest amounts of liquid, having predetermined shapes like a hexagon (left) or a ,tube' with a narrowing (acting as a pressure driven valve, by the way). Given this surface functionalization, either closed fluid volumes or single droplets may be acoustically guided along predetermined pathways along the surface of the chip.
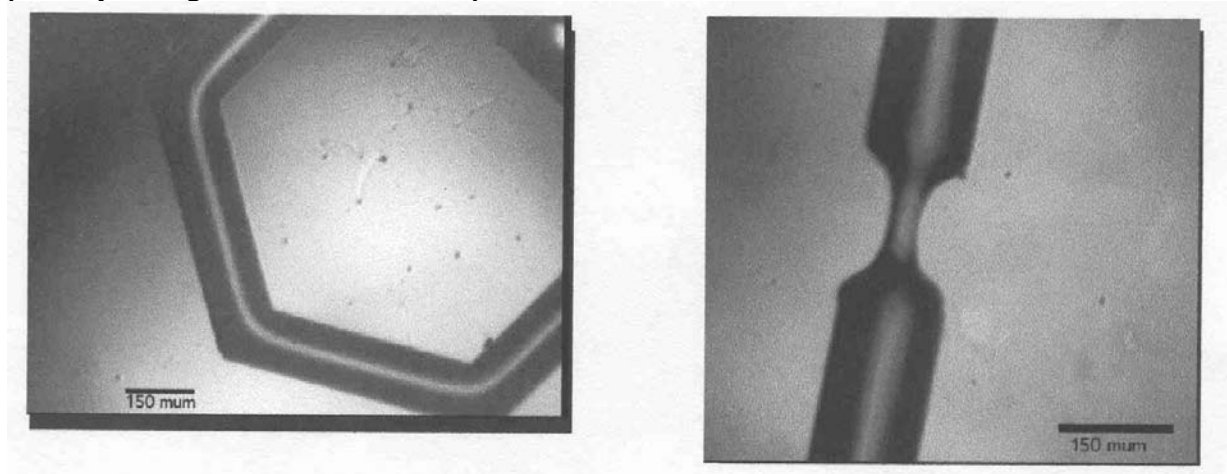
Fig. 5: Photolithografically defined surface modification to modulate its wetability. This way, ,virtual' fluidic tracks are created to confine smallest amounts of liquid to predetermined geometries or to guide a SAW driven droplet along a predetermined path on the chip surface.

Given such chemically defined virtual tracks and the SAW based actuation, we thus can move several droplets of different fluids (or generally different reagents) independently into any desired direction. In Fig. 6, we give a series of snapshots of one of our fluidic chips, where three droplets are actuated using SAW agitation. Depending on the actual layout of the chip, the droplets can be split into smaller ones, they can be merged, mixed and processed in most any fashion. As the SAW nanopumps are electrically adressable, a complete sequence of different steps of a chemical ,experiment' or a biological assay can be computer controlled. Moreover, the simplicity of the fabrication process of our ,programmable bioprocessors' makes them a serious candidate for truly miniaturized laboratories on a chip [8].
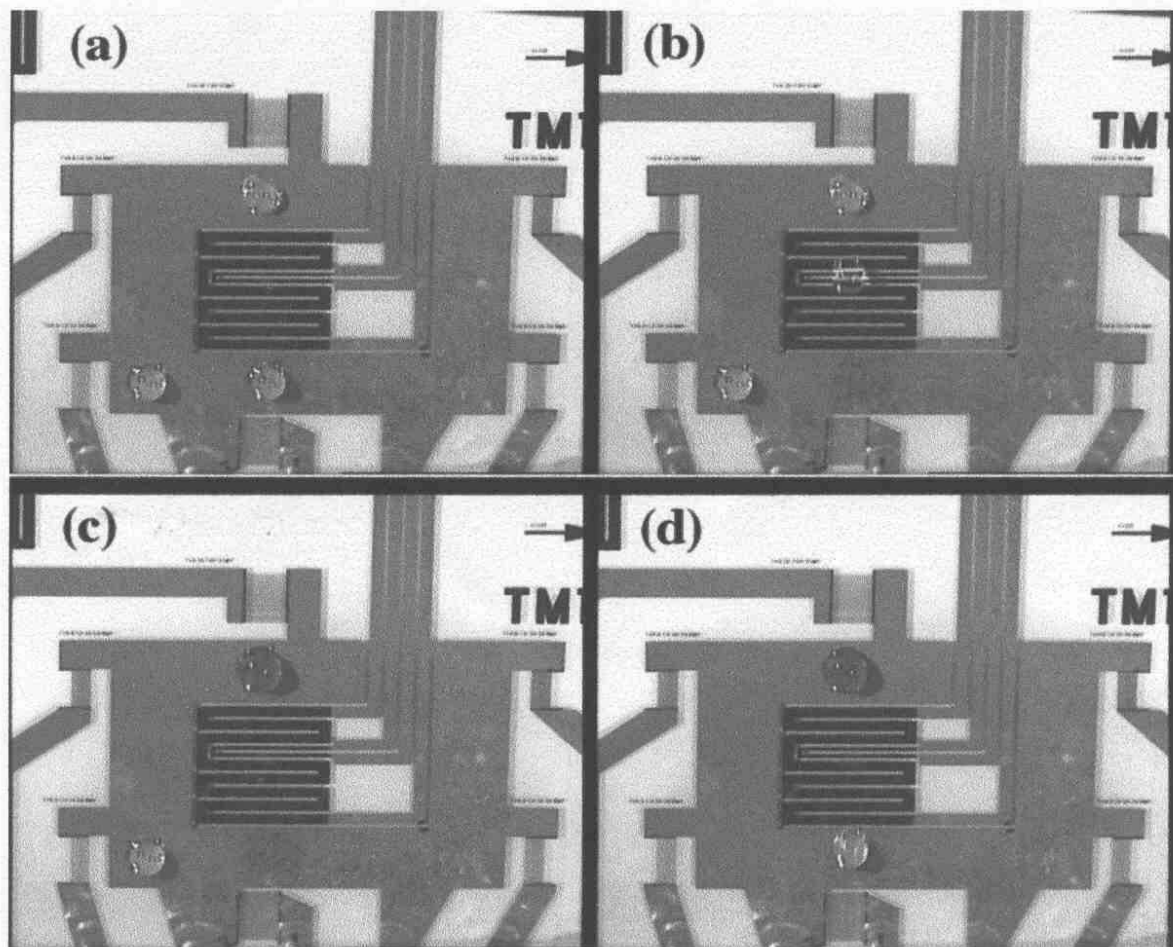
Fig. 6: A SAW driven microfluidic processor. Three droplets (approx. 100 nl each) are moved ,remotely controlled' and independently by the nanopumps. (a) through (d) represent a series of subsequently taken snapshots to visualize the movement, and the ,nanochemical reactions' ocurring when the droplets are merged and mixed by the action of the surface wave. The chip not only contains the nanopumps and the fluidic environment but in the center additional real estate like sensors, and heaters.

It turns out, that the interaction between a SAW and a droplet on a flat surface of a chip is strongly non-linear in terms of the ratio between the SAW wavelength and the droplet diameter. In other words, for a given SAW wavelength and power, only droplets of a certain volume can be effectively actuated along a fluidic track, whereas droplets of a smaller volume remain basically unaffected by the acoustic pressure in this case. This effect can be used to create very small droplets (approx. 50 picoliters) out of a larger one (approximately 50 nanoliters) by leaving them behind on a microstructured chemically modified surface. Such an array of ultrasmall droplets can be regarded as a special form of a microarray. For special applications, also a layer-by-layer build up of complex sandwich systems might be generated employing this scheme.

3. Applications

3.1. SAW Driven Agitation of Hybridization Assays

First applications of the SAW based fluidic actuation already exist and are presently commercialized (ArrayBooster[TM], SlideBooster[TM], Advalytix AG, Brunnthal, Germany): the ability of SAW to efficiently stir and mix smallest amounts of fluids is employed to enhance the results of biological hybridization assays. During hybridization, immobilized DNA fragments or oligonucleotides which are spotted on a microarray, are flooded by an unknown sample fluid, containing other oligonucleotides. Once hybridization occurs, fluorescence markers at the sample molecules accumulate at a specific spot. This fluorescent signal can then be detected and act as a measure for the hybridization efficiency, in other words, the degree of matching between sample and target molecule.

Usually, such micro array hybridizations are performed in a thin capillary fluid film (thickness approx. 50 μm), spread across the area of a conventional microscope slide (7.5cm*2.5cm). Here, the narrowness of the film again leads to a complete suppression of turbulent flow in the film, diffusion is the only driving force to move a sample molecule towards a target spot.

Table 1: Calculated diffusion times for different diffusion lengths and three different particle sizes. A DNA segment of only 100 nm lengths needs about 30 hours to diffuse over a distance of only 1 mm.

Diffusion length (μm)	Potassium ion (0.2nm)	Oligonucleotide (6nm)	PCR product (100nm)
1	0.2 ms	6 ms	100 ms
10	20 ms	600 ms	10 s
100	2 s	60 s	20 min
1000	200 s	100 min	30 h

In table 1, for instance, we have calculated the diffusion time needed to overcome a certain distance in such a thin liquid film. To cover a distance of only 1 mm, a 100 nm long DNA fragment needs already approximately 30 hours. This diffusion limit together with the then unavoidable depletion effects leads to a very slow hybridization process for microarrays. Obviously, mixing and stirring the fluid in the narrow slit would improve this process, as the diffusion limit can be overcome in this case. Although SAW mediated agitation in a thin liquid film is rather slow as compared to a free fluid surface, the diffusion limit can be definitely overcome as we show in Fig. 7. Here, we depict the result of the fluorescence analysis of a typical microarray assay for the diffusion only, and the mixed case. Not only do we observe a quite dramatic increase of the signal intensity in the latter case, also the homogeneity of the single spots on the microarray is much better for the agitated sample [8].
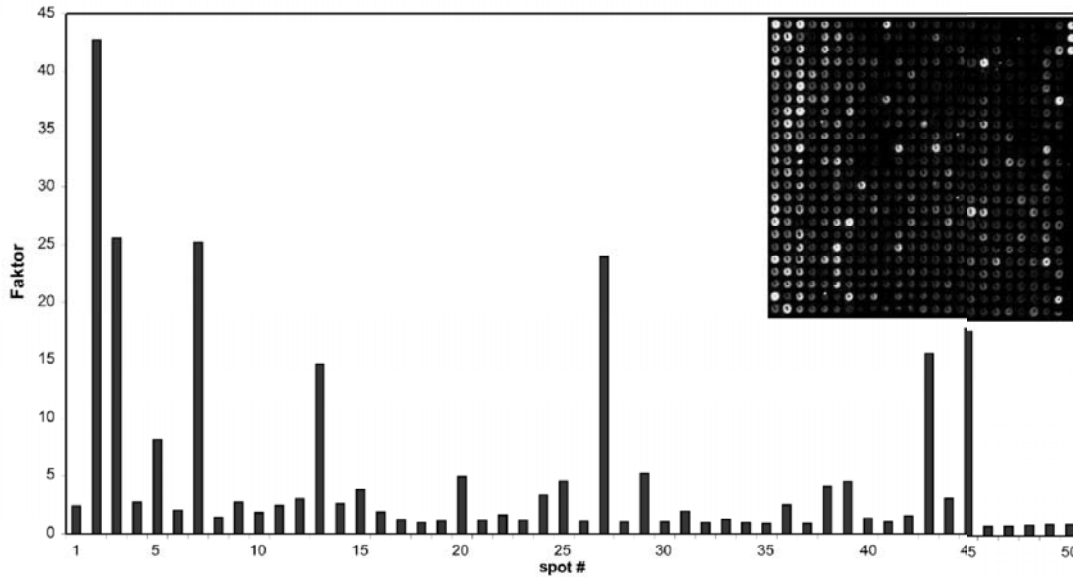
Fig. 7: Result of a flourescence labelled micro array experiment (rat chip with 50 oligos, three subarrays, two replicas each, overnight hybridization at 42°C). We show the intensity ehancement for different spots on the microarray for the agitated sample fluid as compared to the diffusion limited case. The inset shows a typical microarray.

3.1.1. PCR on a Chip

The ability of our novel, acoustically driven, programmable bioprocessors to actuate small liquid droplets, to stir them during hybridization, etc. led us to the attempt to perform a complete polymerase chain reaction (PCR) on a chip.

For this purpose, in co-operation with the Institute for Physical High Technology (IPHT) in Jena, Germany, we have integrated the fluid handling techniques as described above together with a micro heater and a thermometer on the planar surface of the chip. Heating and cooling rates of the order of 5K/sec have been achieved on this chip.

As a proof of concept, a standard PCR protocol (genomic DNA with STS primer, main product 150 base pairs) has been scaled down to a droplet size of less than 1 microliter. A PCR mix containing polymerase, primer, d-NTP, template DNA, and reaction buffer formed the sample droplet. To prevent this small droplet from evaporation, it has been covered by a small amount of mineral oil. Thus, the sample droplet and the oil cover formed a virtual micro reactor which could be actuated as a whole across the chip surface. The technological challenge behind this process was to simultaneously define hydrophobic and lipophobic areas and tracks on the chip surface. In the present case (see upper left inset of Fig. 8), we achieved a wetting angle of about 90° for both fluids.

Both on-chip microarray detection as well as a subsequent gel electrophoretic test showed that PCR on a chip is feasibe and that after 30 cycles even only three start copies in the droplet could be successfully amplified. As a very attractive addition to this on-chip PCR we were also able to show that a multi-spot PCR is also possible. For this purpose, up to four different sample droplets have been covered by oil, simultaneously (see Fig. 8, center).
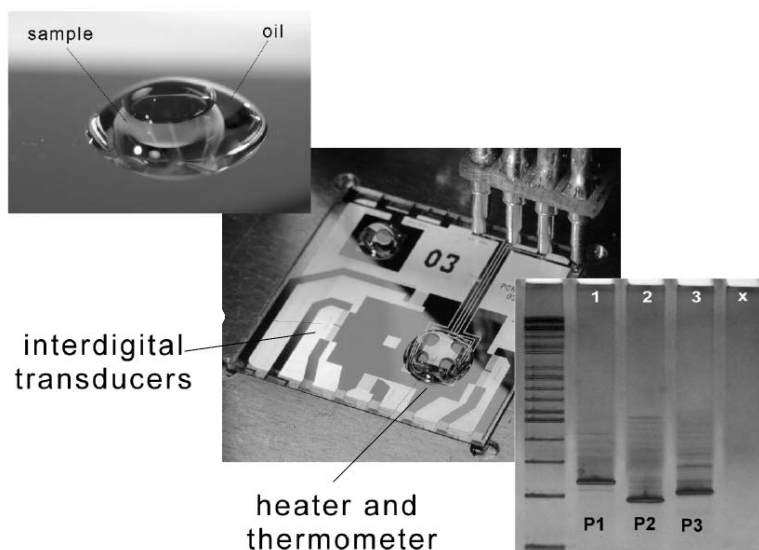
Fig. 8: Chip based polymerase chain reaction (PCR) as a proof of concept for a programmable bioprocessor. On the chip (center), interdigital transducers for the acoustic manipultion of the small droplets as well as a heater and a thermometer have been integrated simultaneously. Four different PCR protocols have been performed at the same time, employing a „multi-spot" technique as described in the text. To prevent the small sample droplets (less than a microliter) from evaporation during the PCR cycles, all four droplets have been covered simultaneously by an oil drop (see also upper inset). A subsequent gel electrophoresis shows, that no cross contamination between the droplets (samples P1 through P3 and a control droplet, lane X) occurs.

The PCR, too, was performed simultaneously for the four droplets. Subsequent analysis showed no cross contamination between the single droplets (see Fig. 8, lower right inset)!

A very important feature of the on-chip polymerase chain reaction is that we are able to monitor the progress of the amplification in situ – again mediated by the SAW driven agitation which favours the dynamic processes involved.

The on-chip PCR is still under evaluation but we anticipate a detailed description of the whole process in the near future.

4. Summary

In summary, we have described a novel and unconventional method for microfluidic fluid handling at very small sample volumes. Surface acoustic waves on a piezoelectric substrate strongly interact with a liquid at the surface of this substrate which leads to the build up of an acoustic radiation pressure in the fluid. This pressure is basically the origin for the SAW mediated internal streaming in the fluid as well as for the actuation of small droplets as a whole. Laterally patterned surface modification in addition enables the creation of fluidic tracks, containers, or functional elements for a planar microfluidic network. Programmable actuation of different small droplets together with a wealth of possible fluidic functional blocks denotes a step towards the realization of a programmable fluidic microprocessor.

5. References

[1] Lord Rayleigh, Proc. London Math Soc. 17, 4 (1885)

[2] B.A. Auld, „Acoustic Fields and Waves in Solids", John Wiley & Sons, New York, 1973

[3] A. Wixforth, J.P. Kotthaus and G. Weimann, Phys. Rev. Lett. 56, 2104 (1986)

[4] C. Rocke, S. Zimmermann, A. Wixforth, J.P. Kotthaus, G. Böhm and G. Weimann, Phys. Rev. Lett. 78, 4099 (1997)

[5] M. Rotter, A.V. Kalameisev, A.O. Govorov, W. Ruile and A. Wixforth, Phys. Rev. Lett. 82, 2171 (1999)

[6] M. Rotter, A. Wixforth, A.O. Govorov, W. Ruile, D. Bernklau and H. Riechert, Appl. Phys. Lett. 75, 965 (1999)

[7] Lord Rayleigh, Phil. Mag. 10 Series 6, 364–374 (1905).

[8] „Flatland: A romance of many dimensions" by Edwin A. Abbott (1894)

[9] A. Wixforth, J. Scriba and C. Gauer, mstNews 5/2002, 42 (2002).

[10] A. Toegl, R. Kirchner, C. Gauer and A. Wixforth, Journal of Biomolecular Techniques, 14:197–204 (2003)

LEAD CHALCOGENIDE IR-EMITTERS AND DETECTORS ON Si-SUBSTRATES

H. Zogg, M. Arnold, D. Zimin, K. Alchalabi, K. Kellermann

Thin Film Physics Group, Swiss Federal Institute of Technology, Zurich, Switzerland

Abstract

Narrow gap IV-VI (lead chalcogenide) compounds are employed since long time as mid-IR-detectors and -lasers. IV-VIs are tolerant to structural defects (dislocations). This allows lattice mismatched MBE-growth on foreign substrates like Si which offers significant advantages with respect to size, costs and thermal conductivities.

In addition, IV-VIs are unique as regards design of Bragg mirrors because of the very high index contrast between IV-VI materials ($n_H =$ 4-5) and BaF_2 (n_L=1.43). A few pairs of quarter wavelength n_H/n_L-stacks suffice to obtain very high reflectivities R>99%.

We review some of our results for different devices: Infrared sensor arrays for thermal imaging on active Si read-out chips, RCEDs (resonant cavity enhanced IR detectors), optically pumped $PbSe/Pb_{1-x}Eu_xSe$ edge emitting DH (double heterostructure) or QW (quantum well) lasers on Si substrates and "wavelength transformers", VCSEL (vertical cavity surface emitting laser) structures operated in sub-threshold.

1. Introduction

Narrow gap lead chalcogenide (IV-VI) materials offer interesting applications for infrared detector arrays as well as infrared emitters in the 3- >12 µm wavelength range [1]. Since the materials are rather tolerant to defects, devices with reasonable properties may be grown even in layers containing a rather high density of threading dislocations. This allows to grow the layers by MBE (molecular beam epitaxy) even on lattice mismatched substrates like Si. Si-substrates are most interesting because of availability, costs and ruggedness, and because one may grow even on Si-chips which contain integrated electronics.

The lattice constants of the lead chalcogenide materials are 8-20% larger than those of Si. Many misfit dislocations form at the interface during growth leading to a considerable density of threading dislocations, which extend up to the surface. In addition, the thermal expansion coefficient of lead-chalcogenides is about 7 times higher than that of Si. Therefore, the high lattice and thermal mismatch strains have to relax. Fortunately, glide of dislocations in IV-VI materials is easy. The main glide planes are of {100} type, and the Burgers vectors <110>. The Schmid factors in (111) oriented layers are therefore different from zero, dislocations can glide in this main glide system under the influence of the thermal mismatch stress field to relieve strain. They glide on each temperature change [2,3]. In addition, two dislocations, which meet within a certain reaction distance may annihilate, or two dislocations may fuse so that one dislocation only is left [4]. Thermal cycling therefore leads to a reduction of the dislocation densities, no dislocation blocking occurs in IV-VI materials with the {100}<110> glide system. The dislocation densities may be determined directly by etch-pit counting, calculated from the X-ray diffraction rocking curve line widths, or from the low temperature saturation Hall mobilities (which are inversely proportional to the mean distance $1/\rho$ between two threading dislocations [ρ dislocation density]). The lowest dislocation

densities we observed in about 10 µm thick layers were in the 10^6 cm^{-2} range. In thinner layers as used for IR-device fabrication dislocation densities are typically about 10^7 cm^{-2}. These rather high densities do not impede the fabrication of infrared sensors of acceptable quality: The high permittivities of IV-VI materials shield the electric fields caused by defects over short distances.

Below we review some of our results for different devices: Infrared sensor arrays for thermal imaging on active Si read-out chips, RCEDs (resonant cavity enhanced IR detectors), optically pumped PbSe/Pb$_{1-x}$Eu$_x$Se edge emitting DH or QW lasers on Si-substrates and "wavelength transformers" (VCSEL (vertical cavity surface emitting laser) structures operated in sub-threshold).

Note that an additional essential advantage of using IV-VI materials for fabrication of RCEDs and VCSELs is that integrated Bragg mirrors can easily be fabricated. This is because of the very high index contrast between IV-VI materials (n$_H$ = 4-5) and BaF$_2$ (n$_L$=1.43). A few pairs of quarter wavelength n$_H$/n$_L$-stacks suffice to get very high reflectivities R>99%.

2. MBE-Growth of Epitaxial IV-VI-on-Si Layers

The chalcogenide layers are grown by solid source molecular beam epitaxy (MBE) at temperatures between 250 °C and 450 °C. A 2-3 nm thick CaF$_2$ buffer layer is employed for compatibility [2,3]. This buffer layer is grown at up to 700°C if passive Si-substrates are used, or at 450°C on active Si-chips with Al-metallization. The preparation of the Si-substrate before MBE growth is crucial. For growth on passive Si(111), we use a modified Shiraki cleaning, where the artificially created surface oxide desorbs in the MBE growth chamber when heating immediately before growth to a temperature above 900°C. For growth on active Si-chips already containing an Al-metallization, a low temperature cleaning is employed. A H-terminated surface is created by etching with a HF/NH$_4$F mixture. N$_2$-bubbling ensures complete wetting [5]. When the sample is heated to the growth temperature, the H desorbs and the substrate is ready for deposition of the CaF$_2$, which forms a coherent layer. After the growth of the buffer layer, the sample is transferred in situ to the second growth chamber where the chalcogenides (and BaF$_2$ for the Bragg mirrors if needed) are deposited. The layers exhibit smooth surfaces except the slip lines due to the dislocation glide, which has occured to relieve the lattice- and thermal expansion mismatch.

3. Infrared Sensor Arrays for Thermal Imaging on Active Si Read-Out Chips

Infrared focal plane arrays (IRFPA) for thermal imaging fabricated with direct band narrow gap semiconductors (NGS) offer the highest sensitivities at a given operation temperature, and integration times can be short due to their high sensitivities and fast response. The signal read-out of the numerous pixels in large 2-d arrays is preferentially performed in Si-technology. This leads to the present hybrid NGS-Si IRFPA lay-outs with e.g. InSb or HgCdTe as sensor material [1]: The NGS chip with the sensor pixels is mated to the Si read-out integrated circuit (ROIC) with In-bumps or loop-holes.

Considerable simplifications and cost savings would result if the NGS layer could be grown directly onto the Si-ROIC chip, thus leading to a heteroepitaxial, but monolithic IRFPA. However, the high structural quality of the NGS layers needed might not easy be attained due to the large lattice and thermal expansion mismatch of the known NGS materials with respect to Si.

IV-VI semiconductors (lead chalcogenides) are much easier to grow and handle than

HgCdTe. They are "forgiving", i.e. layers with much lower structural quality suffice to get useful devices while the theoretical performance of NGS IV-VIs is the same as HgCdTe under similar conditions. We realized 1-d photovoltaic PbSnSe LWIR (8-12 µm wavelength range) and MWIR (3-5 µm) PbTe arrays on Si(111) already some time ago, as well as $Pb_{1-x}Eu_xSe$ arrays for the SWIR (2-4 µm) range [1,3].

Fig. 1 shows part of a 2-d IRFPA grown on an active Si-substrate which contains read-out electronics, and Fig. 2 a schematic cross-section of a pixel [5]. The photovoltaic IR-detector is formed by a p-PbTe/Pb semiconductor/metal junction. The size of the array is 96 x 128 pixels on a 75 µm pitch. Each pixel on the Si(111) substrate contains a switching transistor and a bare area where epitaxial growth of the IV-VI material occurs during MBE-deposition. Arrays are then processed with photolithographic techniques.

In well processed arrays, >97% of the pixels are working and, as usual for NGS devices, high external quantum efficiencies (~60%) are observed. The sensitivities were obtained by measuring the differential resistances Ro at zero bias and normalized with the area A of a device. The mean resistance area product RoA is about 90 Ωcm^2 at 95K operating temperature. This is >10 times above the background noise limit (BNL) for room temperature (RT) radiation and 180° field of view [6]. The chips were employed to set-up a demonstrational thermal imaging camera.

4. Resonant Cavity Enhanced IR Detectors (RCEDs)

The detectors described above exhibit a flat spectral response up to the cut-off wavelength. If a narrow band spectral sensitivity is desired, the active detector material may be placed inside a cavity. The Q-factor of the cavity is determined by the reflectances of the two end-mirrors, and the absorption of the active detector part. Very high Q-factors leading to very narrow spectral sensitivity may be obtained. In addition, despite a very thin detector layer, quantum efficiencies approaching 1 are obtained since a photon at the resonance wavelength is reflected back and forth many times within the cavity before it is absorbed. Since the detector volume is small, in addition, higher sensitivities than with optimized bulk-detectors result.

Fig. 3 shows the structure we realized [7]. The radiation impinges through the Si-substrate. The bottom Bragg mirror consists of two $Pb_{1-x}Eu_xSe/BaF_2$ pairs. The Eu composition x=0.5 is chosen in order that it does not absorb at the design wavelength λ_o=4.4 µm. The calculated reflectivity of the mirror at λ_o is 94 %. The optical thickness of the cavity is designed for 5th order at λ_o. The thicker bottom part again consists of about 3 µm $Pb_{1-x}Eu_xSe$, nonabsorbing at λ_o. The thin top part terminating the cavity is the active detector absorbing layer, $Pb_{1-y}Eu_ySe$ (y<x) with y=0.3. The corresponding cut-off wavelength is somewhat larger than λ_o. This ensures highest sensitivity at as high as possible operating temperature, and, in addition, lower order modes (with higher wavelengths) are not sensed. The top mirror is metallic Pb. Pb forms a blocking contact with IV-VI materials, thus resulting in a photovoltaic IR-detector as in the case of the arrays described in the previous section. The ohmic contact is formed by electrodeposited Au.

The measured spectral quantum efficiency is plotted in Fig. 4. Only the line with order m=5 is visible. Its linewidth (FWHM) is as narrow as $\Delta\lambda = 0.035$ µm ($\Delta\lambda/\lambda_o = 0.8\%$), and the peak quantum efficiency as high as 32%. This is obtained without AR-coating of the Si substrate. With AR-coating, the value would increase to 45 %. The sensitivities we obtained so far with such detectors are above the BNL for operation temperatures up to about 150K.

5. Optically Pumped PbSe/Pb$_{1-x}$Eu$_x$Se Edge Emitting DH or QW Lasers on Si Substrates

Optically pumped PbSnSeTe lasers on IV-VI substrates were already described [8]. With the introduction of compact high-power laser diodes emitting in the 800 - 1600 nm wavelength range, low-cost optically pumped lead chalcogenide IR-emitters for wavelengths above 3 µm become attractive. With optical pumping, no p-n junctions with low ohmic contacts have to be fabricated as for electrically pumped sources, and the design freedom is higher. This includes use of high resistance cladding layers like Pb$_{1-x}$Eu$_x$Se with larger Eu-content and lower carrier concentrations (which in addition diminishes Auger recombination).

The structure of the QW edge emitting laser of Fig. 5 consists of a bottom Pb$_{1-x}$Eu$_x$Se cladding layer, the active Pb$_{1-y}$Eu$_y$Se (y<x) layer containing three PbSe quantum wells (QW), and a top EuSe cladding layer which is transparent to the incoming pump beam. This structure is grown on a (100)-oriented Si wafer precovered with an epitaxial CaF$_2$/BaF$_2$ buffer layer [8]. The 2-3 µm thick IV-VI stack is (100) oriented. Since the Si-substrate does not cleave along (100) as the IV-VIs do, the IV-VI epitaxial layer is lifted off from the substrate by dissolving the BaF$_2$ buffer in water, cleaved into a rectangle with a few mm long and a 300 µm short side length. It is clamped between a heat-conducting substrate and a glass cover transparent to the pump beam. The pump beam is focussed across the short length of the rectangle using a lens, thus forming a gain-guided structure with a cavity length L=300 µm.
A pulsed III-V laser diode with 870 nm emission wavelength and a maximum peak pump power of 5.5 W$_p$ at the sample was used as pump source. The light-out vs light-in characteristics for the QW structure of Fig. 5 is shown in Fig. 6 for different temperatures. Output power is up to 200 mW with this restricted pump power, and differential quantum efficiency is as high as 20%. The laser emission is multi-mode. The highest heat sink temperature where lasing is observed is about 240K (restricted by the power of the pump laser).

IV-VI layers with (111) orientation grown on Si(111) substrates are of higher structural quality [3]. Here, thermal mismatch strains relax on each temperature cycle. Since the cleavage planes of IV-VIs are of {100}-type, the cavity mirrors have to be etched for (111)-oriented layers. We developed a dry processing technology which yields smooth vertical mirror faces. The back mirror is just a quarterwave air (λ/4) groove which yields a (calculated) reflectivity of 78% (Fig. 7). There is no need for epitaxial lift-off with this technique. Double hetero (DH) laser structures were fabricated. The threshold intensity as a function of temperature of such a structure is shown in Fig. 8. The threshold remains essentially constant up to 200K, then it increases. Lasing (employing again the 5.5 W$_p$ pump diode-laser) was observed up to 250K heat sink temperature.

Nearly similar results, but with somewhat still lower threshold pump intensities at low temperatures are observed when the structures are grown on BaF$_2$(111) substrates (second curve in Fig. 8). With this substrate, thermal expansion mismatch is absent since the thermal expansion coefficients of BaF$_2$ and IV-VI materials are almost equal.

These characteristics are compared with calculated threshold intensities for DH-structures. It turns out that the measured thresholds are up to more than two ordes of magnitude higher than the calculated ones, the latter being due to the fundamental Auger recombination and spontaneous emission. The results are roughly explained by assuming a Shockley-Read lifetime as short as 0.1 ns which is caused by the high threading dislocation density $> 10^8$ cm^{-2} in these structures [9]. Since our present technique allows fabrication of IV-VI-on-Si structures with dislocation densities $< 10^7$ cm^{-2}, there is ample room to still increase material quality of the present laser structures to obtain higher S-R lifetimes. This

will lead to considerably lower threshold intensities, or operation to higher temperatures even with the restricted emission powers of the pump diodes we employed.

6. "Wavelength transformers", VCSEL structures operated in sub-threshold.

In general, photoluminescence is broadband and extends over a wide emission angle. In order to obtain a narrow, peaked emission line, resonant cavity structures may be designed. In our device (Fig. 9), the $Pb_{1-x}Eu_xSe$ active layer contains PbSe QWs (each 20 nm thick) at the antinodes of the standing wave and has an optical thickness of $\lambda/2$ where λ is the center wavelength of the emission line. It is sandwiched between two integrated Bragg mirrors. The bottom (epitaxial) mirror consists of a single $BaF_2/Pb_{.95}Eu_{.05}Se$ L/H pair where each layer has $\lambda/4$ optical thickness. The low index L is 1.43 (BaF_2), the high index H is about 4.5 ($Pb_{.95}Eu_{.05}Se$). Note that already one or a few HL-pairs yield high reflectivity R due to the high index contrasts. (R is already 88% for one single L/H pair). The active layer on the bottom mirror is overgrown with the top mirror pairs. Here, we used three $BaF_2/EuSe$ $\lambda/4$ pairs (high refractive index h=2.4 for EuSe). This mirror is transparent to the incoming light beam of the III-V laser diode, and its reflectivity at 4.2 µm is 97%. Alternatively, since this mirror must not consist of an epitaxial material, polycrystalline SiO_2/TiO_2 L/H pairs may be evaporated or sputtered in a separate system. Both combinations exhibit nearly the same refractive indices. We tried both variants with equal success.

The device (its structure exactly corresponds to a VCSEL, but with lower reflectivity end mirrors) is operated at RT in the subthreshold region. Its line width is about 6% for the present realisation, and power efficiency is above 10^{-4}. By changing the mirror reflectivities, the quality-factor of the whole structure may be tuned [10]. The position of the gain curve is determined by the well width and allows optimization for narrow band emission ranging from about 3 to 4.6 µm at RT. This allows easy tuning to the absorption lines of gases like CO_2, CO or CH_4. The Si substrate is transparent to the output beam and also acts as a mechanical protection. This is at variance to its II-VI counterpart, where an expensive CdZnTe-substrate and lift-off techniques had to be employed [11].

Note that optically pumped IV-VI VCSELs taking advantage of the high index contrast with IV-VI materials have already been described by two groups [12,13]. These structures were grown on BaF_2 substrates, and pulsed laser emission up to RT was achieved. However, large laboratory type pump lasers were used for excitation.

7. Conclusions

Although IV-VI materials are not on the mainstream of present optoelectronic IR-devices, the unique properties of IV-VIs allow to obtain useful devices with quite a limited effort. In the present review, the following IV-VI optoelectronic devices fabricated in layers grown by MBE on Si-substrates have been described:
- monolithic heteroepitaxial IR-FPA on active Si-substrates,
- resonant cavity infrared detectors (RCED) with spectral linewidths as narrow as 0.8%,
- optically pumped edge emitting mid-IR lasers, and
- "wavelength transformers", VCSELs operating in the subthreshold region.
These devices demonstrate a broad application range of the narrow-gap IV-VI materials as detectors for thermal imaging and hyperspectral spectroscopic applications as well as emitters for various gas sensing spectroscopies.

Corresponding author: Hans Zogg, Thin Film Physics Group, Swiss Federal Institute of Technology, Technoparkstr. 1, CH-8005 Zurich, Switzerland, phone +41 1 445 1480, fax +41 1 445 1499, zogg@phys.ethz.ch, http://www.tfp.ethz.ch
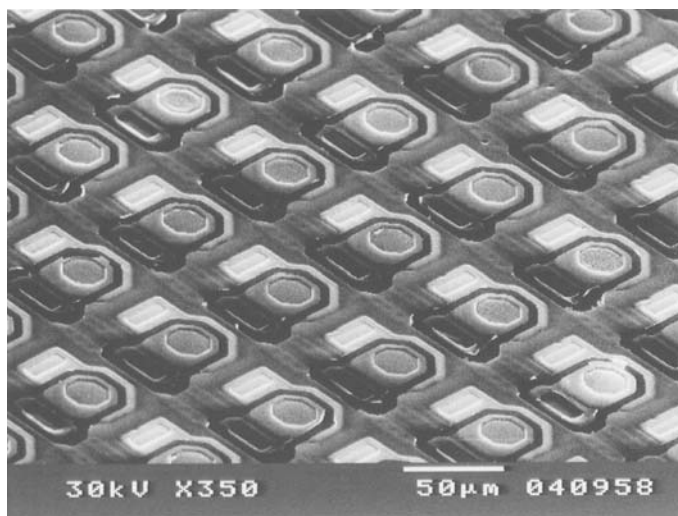
Fig. 1. Part of the completely processed monolithic 96 x 128 PbTe-on-Si IR-FPA for the MWIR with the read-out electronics in the Si-substrate.
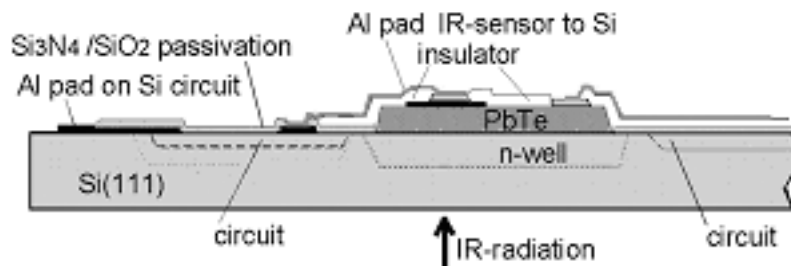
Fig. 2. Schematic cross-section of one pixel with the PbTe island as backside illuminated photovoltaic IR-sensor, and the electrical connections to the Si circuit (access transistor) and common anode.
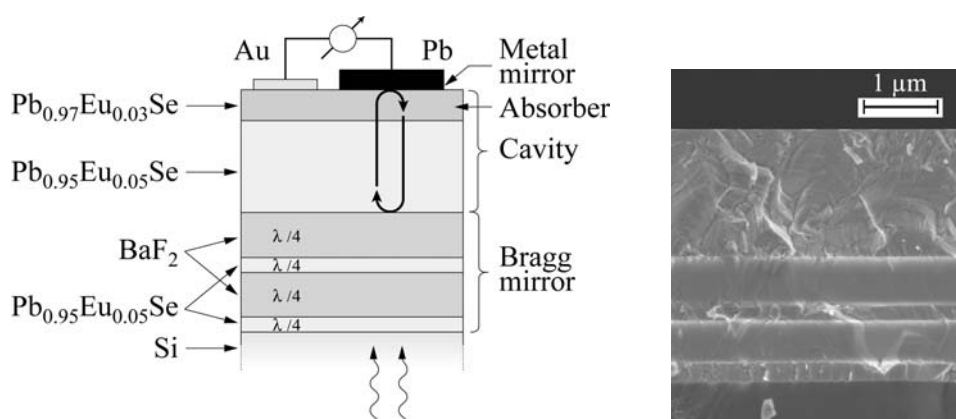
Fig. 3. Schematic cross section of a resonant cavity enhanced IR-photodetector realized with IV-VI materials on a Si substrate, and scanning electron micrograph of a cleaved cross section of the device.
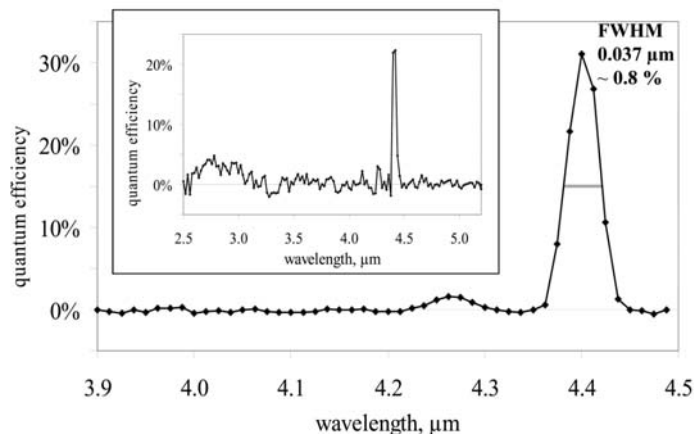
Fig. 4. Spectral quantum efficiency of the narrow band resonant cavity detector (RCED) with 32% peak efficiency (without AR-coating).
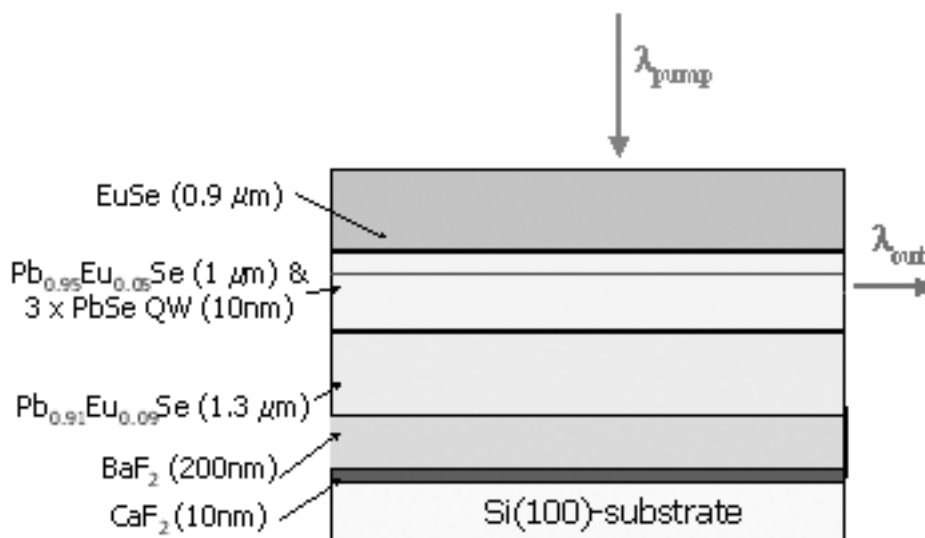
Fig. 5. Structure of an optically pumped QW IV-VI laser on a Si(100)-substrate.
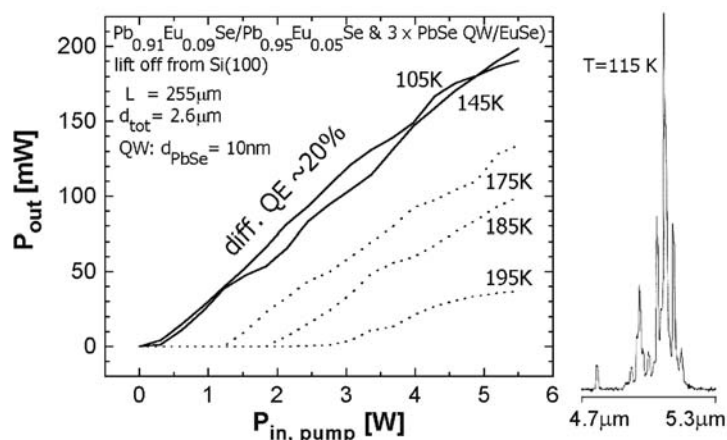
Fig. 6. Light-in/light-out characteristics of the laser structure of Fig. 5 (lifted off from the temporary (100) Si-substrate), and laser spectrum at 115K.
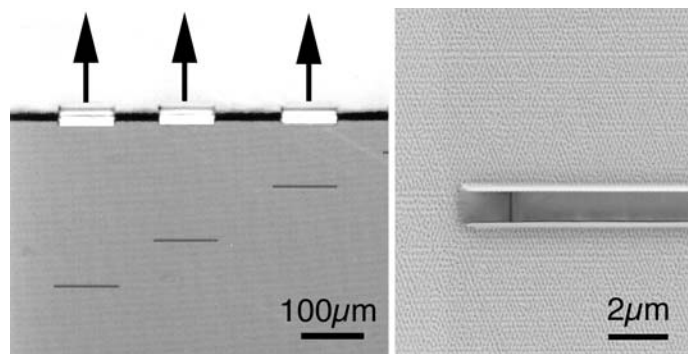
Fig. 7. FIB (focussed ion beam) etched mirrors in a IV-VI on Si(111) DH laser structure containing 3 different cavity lengths (left) and enlarged detail (right).
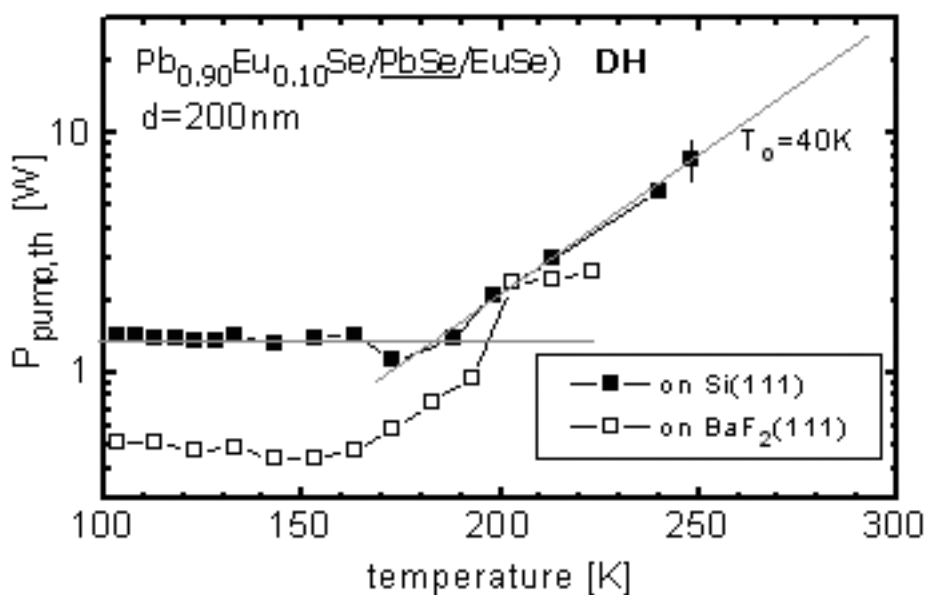
Fig. 8. Threshold pump powers vs T for a (111) oriented layer grown on Si(111) with etched mirror faces. For comparison, the results of a similar structure, but grown on a BaF_2 substrate, are indicated, too.
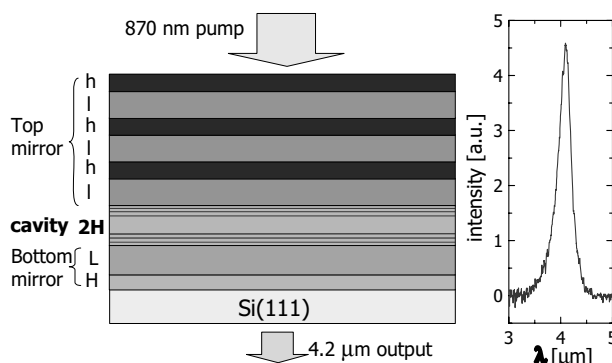
Fig. 9. Structure of a resonant cavity mid-IR source for optical excitation and corresponding emission spectrum at RT. The active cavity consists of 6 PbSe QWs embedded in a $Pb_{1-x}Eu_xSe$ layer and is sandwiched between two Bragg mirrors.

References

[1] H. Zogg, A. Ishida, IV-VI (lead chalcogenide) infrared sensors and lasers, in Infrared Detectors and Emitters, P. Capper, C.T. Elliott, eds., Kluwer Acad Publ 2000.

[2] G. Springholz, Z. Shi, H. Zogg, in "Heteroepitaxy: Thin Film Systems", Eds. W.K. Liu and M.B. Santos, Ch. 14, pp. 621-688, (World Scientific Publishing, Singapore, 1999)

[3] H. Zogg, "Lead Chalcogenide Infrared Detectors Grown on Silicon Substrates", in "Optoelectronic Properties of Semiconductors and Superlattices", M.O. Manasreh, Series editor, Vol. 18, "Lead Chalcogenides: Physics and Applications", D. Khokhlov ed., Taylor & Francis Books, Inc., New York and London, pp 587-616, 2003.

[4] P. Müller, H. Zogg, A. Fach, J. John, C. Paglino, A.N. Tiwari, M. Krejci, and G. Kostorz "Reduction of threading dislocation densities in heavily lattice mismatched PbSe on Si(111) by glide" *Phys. Rev. Lett.,* vol. 78, pp. 3007-3010, 1997.

[5] H. Zogg, K. Alchalabi, D. Zimin, Klaus Kellermann, Two-dimensional monolithic lead chalcogenide infrared sensor arrays on silicon read-out chips and noise mechanisms, IEEE Trans. Electron Devices ED50, pp. 209 - 214, Jan 2003.

[6] State of the art *hybrid* NGS IRFPA exhibit still much higher values, however.

[7] M. Arnold, D. Zimin, K. Alchalabi, H. Zogg, in preparation

[8] D.M. Dureev, O.I. Davarashivili, I.I. Zasavitskii, B.M. Matsonashvili, A.P. Shotov, Optically pumped $Pb_{1-x}Sn_xSe_{1-y}Te_y$ heterojunction lasers with matched gratings at the interface, Soviet-Journal-of-Quantum-Electronics. Dec. 1978, 8(12), 1481-3 (Original: Kvantovaya-Elektronika,-Moskva. Dec. 1978, 5(12), 2630-3)

[9] K. Kellermann, D. Zimin, K. Alchalabi, H. Zogg, Optically pumped lead-chalcogenide mid-infrared lasers on Si-substrates, J. Appl. Phys. 94, 7053, 2003.

[10] H. Zogg, K. Kellermann, K. Alchalabi, D. Zimin, Optically pumped lead-chalcogenide mid-infrared emitters on Si-substrates, Infrared Phys. Technol., in print

[11] E. Hadji, E. Picard, C. Roux, E. Molva, P. Ferret, 3.3 um microcavity light emitter for gas detection, Optics Lett. 25, 725, 2000.

[12] W. Heiss, T. Schwarzl, G. Springholz, K. Biermann, K. Reimann, "Above room temperature mid-infrared lasing from vertical cavity surface emitting PbTe quantum well lasers", Appl. Phys. Lett. 78, 862, 2001.

[13] F. Zhao, H. Wu, Lalith Jayasinghe, Z. Shi, Above room temperature optically pumped 4.12 um midinfrared vertical cavity surface emitting lasers, Appl. Phys. Lett. 80, 1129, 2002.

CHEMICAL SILVERING OF WAVEGUIDE BODIES

M. Dyntu, D. Meglei

International Laboratory of Superconductivity and Solid State Electronics, Academy of Sciences of Moldova, Academiei str., 3/3, Chisinau, Republic of Moldova

In the work there are experimentally chosen optimal compositions and regime of chemical deposition of silver on waveguide bodies, possessing much higher stability of the solution. The work gives the methods of the surface preparation, including annealing, fat removing in alkaline and organic electrolytes, etching, sensibilization followed by chemical deposition on them of a copper sublayer of copper sulphate.

It is known that bodies of waveguide devices are prepared of dielectrics (plastic or ceramics), which are subjected to metallization, mainly copper-plating and silvering. At present there are different technologies of metal cover deposition on waveguide bodies - burning-in, melting, electron-beam laser sputtering, etc. However, these methods require complex equipment and high energy expenditure.

For metallization of bodies of waveguide dielectrics the metal sputtering is used when the melted metal is sputtered by the gas spurt (air or argon) into smaller particles, which strike with high velocity (100-150 m/sec) against the metallized surface and adhering to it form the covering layer.

By sputtering one can deposit zinc, alloys of silver-cadmium and silver-tin, brass, copper, nickel, etc. For production of waveguide bodies multi-layered coverings are used. The first layer to deposit is the alloy of silver and cadmium possessing small resistivity. Its thickness is 0,25 µm. Then in order to give higher mechanical strength to the body it is covered with brass or copper up to the required thickness (3-5 µm). The coverings obtained by sputtering have low mechanical strength and porosity. Besides, metallization by sputtering is performed by special installations.

The most perspective technological method of silver deposition is the electrochemical method, precisely silver deposition from cyanide baths. Cyanide electrolytes have good scattering ability and high quality of deposits, but they have significant shortenings, they are poisonous and require application of electrical current.

Traditional non-cyanide methods of chemical reduction of silver are relatively high-productive, however their solutions are low-stable and significantly limit the sphere of their application.

Before metallization the most important operation is, as it is known, preparation of the surface of the waveguide body. Carefulness of the preparation influences greatly the covering service for any purpose. Before the chemical copper-plating the waveguide bodies were subjected to fat removing in the following solution (g/l):

NaOH - caustic soda - 15
Na_2CO_3 - calcined soda 10
$Na_3PO_4 \bullet 12H_2O$ - trisodiumphosphate - 15
$Na_2SiO_3 \bullet nH_2O$ - liquid sodium glass - 25

at the temperature 40-50°C during 10-30 min.

Chemical etching of the body was carried out in the solution containing 60 g/l H_2SO_4 and 40 g/l HF at room temperature during 5-10 min. After the chemical etching the bodies are thoroughly washed with distilled water, then they are subjected to thermal treatment at the

temperature 60±10°C during 2 hours, followed by cooling together with the furnace. Ceramics annealing is used not only for moisture removing, but also for ensuring maximally strong adhesion of the covering with the base.

After the annealing the waveguide bodies were subjected to activation in the following solution (g/l):

$SnCl2•2H_2O$ - 50

HCl - 50

at T=18-20°C during 20-30 min.

On the prepared surfaces of the waveguide bodies a copper sublayer from sulphate electrolyte was deposited by the chemical method. Formed conducting copper layer has a strong adhesion to ceramics and its thickness is directly proportional to the time of copper-plating: for 5 min it is equal to 5-6 µm, for 10 min – to 10-12 µm.

After deposition of the conducting layer and corresponding washing the waveguide bodies are activated in H_2SO_4 (50-100 g/l) during 30-50 sec at the temperature 15-25°C, then they are washed with distilled water and then silvered in the electrolyte based on $AgNO_3$ and $KNaC_4H_4O_6•4H_2O$. Silver deposition occurs during the first 20-30 minutes, and about 2 µm is deposited. For increasing of the covering thickness the body is thoroughly washed with running water, then with distilled water and is kept for 1-2 min in 10% aqueous solution of ammonia, then again it is silvered in the same solution.

Optical-microscopic analysis of silvered coverings testifies to non-porosity and uniformity of deposition on both internal and external surfaces of the waveguide bodies. The obtained coverings have high mechanical adherence with the base.

NEW TECHNOLOGY OF PREPARATION OF INDIUM ANTIMONIDE THIN FILMS ONTO DIELECTRICAL SUBSTRATES AND ONTO OXIDE SILICON SUBSTRATES

Ju.A. Nikolskii, V.V. Grigorova, S.E. Zyuzin, I.M. Kot, L.A. Pleshakova

SEE HPE "Borisoglebsk State Pedagogical Institute", Borisoglebsk, Byelorussia
E-mail: bgpi@mail.ru

The technology of preparation of the indium antimonide thin films of n-type conductivity is an actual problem at the present time. The preparation of thin semiconductor films by different methods is described in scientific literature widely and multilaterally. These methods are described for elementary, binary and multicomponent semiconductor materials, which are still widely used in practice for preparation of the new semiconductor integral schemes, devices and constructions successfully working in different spheres of human activity. These methods are applied to the vacuum evaporation of initial crystal and crystalline powder, gas-transport method, Vecshinsky method, three temperatures method, discrete evaporation, thermal recrystallisation and etc., which were improved by the process of preparation thin semiconductor layers as elementary, binary as well as multicomponent semiconductor materials.

The condensation of different materials in vacuum is one of main methods of the preparation of thin films applied in the physics investigations, electronic technique, construction of apparatus, microelectronic and other spheres of science and technique. The lawfulness of transition of substance from the condensering phase in gas one, transformation of its vapors in vacuum from the evaporator to substrate and condensation of steam onto the substrate were studied very well. The theories of vacuum evaporation, condensation processes, germination, crystallization and stature of films applicably to elementary semiconductors and binary semiconductor compounds and also to multicomponent systems were described in detail in monographies [1, 2].

Last time the methods of molecular-ray epitaxion (MRE) have spread in thin film technology. This method in used for preparation indium antimonide films, for instance, for growing of heteroepitaxial films onto [100] surface of substrates from semiisolate of GaAs alloyed by Cr [3]. The velocity of growth was about 1 μm/h. In spite of the very big disaccording in lattice parameters the single crystalline films were prepared with the polished surface at substrate temperature 330…420°C. The electrical parameters equal $n=(2…4)\cdot10^{16}\,cm^{-3}$ & $\mu_n=(4…5)\cdot10^4\,cm^2/V\cdot s$ at T=300K that it close to values of parameters for massive material.

The method of temperature source programme was used for preparation of $In_{1-x}Ga_xSb$ and $InAs_xSb_{1-x}$ films [4]. The cleave plates of mica served as the substrates. After condensation the films inflict to recrystalization. The electron mobility on InSb films was $(5.0\div6.5)\cdot10^4 cm^2/V\cdot s$ and it was decreasing quickly at increasing of GaSb content.

Among the ways of the epitaxial layers growing the epitaxy from the vapor phase and also the liquid-phase epitaxy received wide use.

The important factors technology methods of the thin semiconductor films obtaining are the simplicity of method, its reproduction, the possibility of the layer preparation with parameters and properties close to properties of single crystal or initial material. All above

named methods as a rule didn't give possibility to obtain the layers with properties close to properties of initial material.

We suggested the new method of the preparation of thin semiconductor layers n-InSb, which permits significantly to approach layers on parameters and properties to those of initial single crystal InSb of n-type conductivity.

The earlier indium antimonide thin films of n-type conductivity were received by the different above – mentioned methods onto the dielectrical substrates from mica, quartz, suphize, silicon oxide and also onto different crystallographical planes, received by cleaving of single crystals of semiconductor materials Ge, Si, also $A^{II}B^{IV}$ and $A^{III}B^{V}$ semiconductors – so as ZnTe, CdTe, ZnSe, CdSe, InSb, GaAs, InAs and entire row of the other two, three and multicomponent semiconductors.

The essence of new method consists in its essential difference from all the listed above methods and it will practically effectively solve all technological problems of the thin film semiconductor material preparation at its improvement. It needs to take a piece of n-InSb semiconductor single crystal by volume $\sim 8mm^3 = 2 \times 2 \times 2mm$, that is easy to make by cleaving it from the single crystal block and of course it is not exactly at the appointed dimension. After that put it onto substrate made of the material on which it is needed to get this layer (for instance, mica, quartz, sapphire, silicon oxide and etc.) and to heat this substrate till the temperature of the material melting in vacuum $\sim 10^{-4}$ torr. The simple calculations show that for getting thin film of this cube with thickness $20 \div 30$ µm the layer square must be $\sim 400mm^2$, i.e. 20×20 mm or 300 mm^2, i.e.17,5×17,5 mm.

It is typical, that the layers of this thickness have already physical properties approximating to properties of massive materials, because the influence of layer thickness, e.g. the dimension effect already does not influence the electrophysical properties of layers for film of InSb of n-type conductivity. The experimental investigations of heating process of substrate presuppose two types of heating: graphite furnace in which quartz tubes are fitted with nihrome spiral and simple heater from tungsten plate which possesses notable least inert ion that permits quickly to change temperature of heating process and of course easier to control melting process and layer crystallization.

In our experiment the temperature of furnace was about 550ºC at which n-InSb crystal was melting onto mica. Under action of gravitation of the plane-parallel load hung under this furnace the drop was spread equally onto the substrate, forming the layer of indium antimonide of n-type conductivity and 20-30 micron thickness. The action of this load onto drop performs during 5 seconds and then the furnace swiches off and the layer crystallizes onto the substrate. Of course in the result of the melting the crystalline structure of n-InSb binary compound destroys but in new agregate state it is for a little time and appearance of any admixtures and considerable deviations from the initial crystalline structure in the crystallization process of layer under the influence of gravity at a drop in temperature is scarcely probable.

The presense of covalent chemical cohesion in $A^{III}B^{V}$ components, which has property of direction leads to placing some limits to the mutual arrangement of atoms that prevents them from being diffused. Because of the difficulties of the diffusion there is the disturbing in the crystallization process. However in the components with covalent cohesion the diffusion coefficient increases exponentially at temperature rise according to the equlibrium that may be reached quickly enough.

After the drop spreads and the layer is subjected to the process of crystallization the form of the sample onto substrate under the influence of gravity may be diffuse.

The measurement of electrophysical parameters and properties of the preparating layer can lead to cutting of it a rectangular part by the ordinary method or by Van-der-Paw method [5].

The leading estimate of electrophisical parameters is preparating by this method of n-InSb thin film onto mica substrate at room temperature displayed that its electroconductivity is close to value in the initial single crystal and consists $\sim 10^{-3}$ $Om^{-1}cm^{-1}$ and the concentration of charge carriers equal $10^{15} \div 10^{16} cm^{-3}$. It is characteristic that these data are close to parameters of the initial single crystal.

The given method permits to prepare also heterostructure if the semiconductor substrate is on the silicon base. So for preparation of n-InSb-SiO$_2$-p-Si heterostructure the appointed method can considerably change it parameters, because at the present time it is known [2], that n-InSb layers are being prepared by the above – mentioned method at room temperature in concentration interval $(0,5-1,0) \cdot 10^{17} cm^{-3}$ and conductivity $\sim 10^2$ Om^{-1} cm^{-1}. It is significant that SiO$_2$-p-Si substrate heating in vacuum 10^{-4} torr till 550°C temperature doesn't cause any changes of its electrical properties and heterostructure prepared with the above-named n-InSb layer will possess large integral sensibility in infra-red region of spectrum.

To the given advantages of new technology preparation of n-InSb semiconductor layers and n-InSb-SiO$_2$-p-Si heterostructures we can relate the time reducing of realization of technological process, consequential economy of initial crystal. So, for instance, at discrete method of preparation the initial crystal breaks into pieces with dimension $\leq$ 150 μm and the remainder in volume – 30-40% of material isn't used in this process. Besides at the evaporation onto the substrate in best case it falls 50 per cent of initial material. Therefore the reduction of material expenditure is directly connected with economizing on initial stuff and on time of the layer preparation process. In the process of layer recrystallization prepared by discrete evaporation oxide layer influences its electrophysical parameters and in the first place its purity. All above listed methods of the preparation of the indium antimonide films of n-type conductivity and alloys on its base in this or another measure reduce electrical parameters of layers in comparison with single crystal of this material if the dimension effect is discounted.

Of course the further investigations of n-InSb films prepared by the described method intend attentive investigation of the structure by electronographic, x-ray, metallographic and other methods with aim of further explanation of influence of the structure particular films onto its electrophysical, galvano-magnetic, optical, photoelectrical and other properties.

The suggested method to the important degree is applicable for materials with melting temperature lower than 600°C. At higher temperatures the determining influence on the formed layer can render a surface of gravity acting onto layers and also time of its action. Notwithstanding we suppose that the suggested method will find successful application in technology of preparation of thin semiconductor layers.

References

[1] В.А. Касьян, П.И. Кетруш, Ю.А. Никольский, Ф.И. Пасечник Тонкие пленки антимонида индия. Монография, Кишинев, Штиинца, 162 стр., 1989.

[2] Ю.А. Никольский Кинетические явления в тонкопленочных структурах n-InSb, In$_{1-x}$Ga$_x$ Sb и n-InSb-SiO$_2$-p-Si и приборы на их основе: Монография, Борисоглебск, 2001 г., 253 стр. Деп. ВИНИТИ 22-06-01 № 1476-В 2002.

[3] M. Janoi, T. Takuje, M. Kimata, Heferoepitaxion InSb Films Grown by Molecular Beam Epitaxy // Phys. Stat . Sol., v. 54. № 2, p. 707-713, 1979.

[4] Y. Amemiya, H. Terao, Y. Sakoi, Electrical Properties of InSt-based Mixed Crystal Films.// Joum. Appl. Phys. V. 44, № 4, p. 1625-1630, 1973.

[5] L.J. Van der Pauw, Philips. Res. Rep., 13, 1, (1958).

ACOUSTICAL PROPERTIES OF RECTANGULAR GaN QUANTUM WIRES COVERED BY ELASTICALLY DISSIMILAR BARRIERS WITH CLAMPED OUTER SURFACES

D.L. Nika[1], N.D. Zincenco[1] and M. Al-Sabayleh[2]

[1]*Department of Theoretical Physics, State University of Moldova, Chisinau, Republic of Moldova*
[2]*Department of Physics, Mutan University, Mutan, Jordan*

Abstract

We had theoretically studied the energy spectra and group velocities of the acoustic phonons in the rectangular GaN nanowire, covered with elastically dissimilar barriers. It was established that the number of quantum branches increases and spatial degeneracy by wave number q disappears in such wire. The elastic properties of acoustically mismatched barrier influence dramatically the phonon spectrum. The barriers with lower sound velocity ("acoustically slow" barriers) are "compressing" the phonon energy spectrum and strongly reducing the group velocities of the phonons. The barriers with higher sound velocity ("acoustically fast barriers") demonstrated the opposite effect.

The reason for such anomalous, at first look, but strong influence of barrier had been established. In particular, it consists in the re-distribution of the elastic deformations in the heterowire. In the case of "acoustically slow" barriers the wave of elastic deformations in a wide interval of the wave vector retracts into barriers (phonon depletion of the core wire) and spreads there with the velocities corresponding to the acoustic properties of the barrier layers. The opposite situation takes place in the case of "acoustically fast" barriers.

It is concluded that these effects can be used in the phonon engineering.

1. Introduction

The last decade the great successes were achieved in the field of the manufacturing technology for the highly perfected nano-dimensional semiconductor heterostructures: quantum wells, quantum wires, and quantum dots. In this connection, the electronic and phonon properties of low-dimensional structures attract the rapt attention of researchers. The features of the energy spectrum of the acoustic phonons, stipulated by the dimensions and shape of the structures [1-11], manifest themselves in kinetic and optic phenomena when feature size d of the structure becomes smaller than the phonon mean free paths λ. The controlling of the phonon and electron phenomena by means of the modification of the phonon spectra got name of the phonon engineering [12].

Complete description of the elastic vibrations in the freestanding slabs was given in Ref. [1]. Also, there were presented some particular solutions for the problem of elastic vibrations in cylindrical and rectangular nanowires. Theoretically, the folded acoustical phonons in a layered medium have been studied by Rytov [2]. Later, the folded phonons have been observed experimentally in quantum well superlattices [3]. The important properties of the acoustic phonons in the slabs, quantum wires and quantum dots were established in Refs. [4-7]. Acoustic properties of the spherical quantum dots, surrounded by the acoustically dissimilar medium were described in Ref. [8]. Dispersion of the phonons in quantum dot

superlattices was recently calculated with account of the elastic properties of both quantum dot and barrier material [9]. The phonon spectra in the rectangular nanowires with an aspect ratio of 2 or greater were considered in Ref. [10]. The complete solution of this problem with the description of all types of the acoustic phonon polarization was given in Ref. [11].

In a number of our articles [13-15] acoustic phonon spectra and electron-phonon phenomena in the planar three-layered heterostructures with free and clamped surfaces were investigated in detail. In the present work we consider the rectangular heterowires with clamped outer surfaces. Due to the lateral confinement in the quantum wires we can expect more pronounced manifestations of the quantum phonon effects than in the planar heterostructures. We have calculated phonon energy spectra, phonon group velocities and distributions of the elastic deformations in the rectangular quantum heterowire with GaN core wire and different cladding barriers.

The remainder of the paper is organized as follows. Section 2 contains the derivation of the equation of motion for the elastic vibrations in the inhomogeneous rectangular heterowire. The hexagonal symmetry of GaN core wire is accounted. There are formulated the boundary conditions for the heterowire with clamped outer surfaces. The method of numerical solution of the equations of motion for the rectangular heterowire with inhomogeneous distribution of the mass density and elastic constants in the cross-sectional plane is described.

The results of the calculation of phonon energy spectra and group velocities depending on phonon wavenumber and phonon frequency are presented in Section 3. The conclusions are given in Section 4.

2. Theoretical model

We consider the structure consisting of rectangular GaN wire (forming quantum well) confined in the rectangular barrier. A schematic view of the structure is presented in the insets to Fig. 1.

As an example of the well material, there was used GaN, possessing wide perspectives of application in quantum electronics and optics. It is important to note that calculating programs developed and used by us allow considering the any combinations of the wells and the barrier materials. It is assumed that GaN crystal lattice has wurtzite structure with reference axis c along the nanowire axis. The axis X_3 of the Cartesian coordinate system is directed along axis c, but axes X_1 and X_2 are in the cross-sectional plane of the nanowire parallel to its sides (see insets to Fig.1). The origin of the coordinate system is in the center of the nanowire. Linear sizes of the rectangular core wire are designated $d_1^{(1)}$ and $d_2^{(1)}$ while the total lateral dimensions (nanowire thickness plus barrier thickness) are d_1 and d_2 correspondingly. The lateral dimensions of the nanowire $d_i^{(1)}$ and d_i are chosen in the nanometer range, while the length of the wire is formally considered as infinite. For the description of the influence of the barrier material we have calculated also phonon energy spectra for the bare GaN wire (see Fig.1(a,b)).

The equations of motion for elastic vibrations in an anisotropic medium can be written as

$$\rho \frac{\partial^2 U_m}{\partial^2 t} = \frac{\partial \sigma_{mi}}{\partial x_i}, \ m = 1, 2, 3; \ i = 1, 2, 3 \ , \tag{1}$$

where $\vec{U} = (U_1, U_2, U_3)$ is the displacement vector, ρ is the mass density of the material, σ_{mi} is the elastic stress tensor given by $\sigma_{mi} = c_{mikj} U_{kj}$, and $U_{kj} = (1/2)((\partial U_k / \partial x_j) + (\partial U_j / \partial x_k))$ is the

strain tensor. Some normal acoustical modes in an isotropic rectangular quantum wire without shell ($c_{iklm} = const$) have been studied in Ref. [1] and for cubic quantum wire in Ref. [11]. At the differentiation performing in Eq. (1) it is necessary to take into account that investigated structure is inhomogeneous in the cross-sectional plane of the wire (X_1, X_2), therefore elastic modules $c_{mikj}(x_1, x_2)$ and material mass density $\rho(x_1, x_2)$ are the piece-wise functions of x_1, x_2. At the performing of numerical calculations we replaced the piece-wise functions with the functions smoothly varying from the value in the nanowire material to the value in the barrier material. A posteriori check has shown that the selection of the smoothing function very weakly (of the order of calculation error) influences the calculated phonon energy spectrum and distributions of the displacements $u_i(x_1, x_2)$ if the thickness of the transition layer is taken equal to or less than lattice constant and the smoothing function is selected without sharp changes of the derivatives. We have used the standard system of the two-index notations accepted in Ref. [13]. In the wurtzite crystal of the hexagonal symmetry (hexagonal space group C_{6v}^4) there are five different elastic modules: $c_{11}, c_{33}, c_{12}, c_{13}$ and c_{44}, where

$c_{11} = c_{1111} = c_{2222}$, $c_{33} = c_{3333}$, $c_{12} = c_{1122} = c_{2211}$, $c_{13} = c_{1133} = c_{3311} = c_{2233} = c_{3322}$, $c_{44} = c_{1313} = c_{3131}$, $c_{55} = c_{44}$, $c_{66} = c_{1212} = c_{2121} = (c_{11} - c_{22})/2$. The axis X_3 is assumed to be along with the direction of the acoustical wave propagation. Since considered structure is homogeneous in the direction of X_3, and inhomogeneous in (X_1, X_2) plane we look for the solution of Eq. (1) in the following form

$$U_i(x_1, x_2, x_3, t) = u_i(x_1, x_2)e^{i(\omega t - qx_3)} \tag{2}$$

Substituting Eq. (2) in Eq. (1) we take three equations for components of the displacement vector:

$$(-\omega^2 \rho + c_{44}q^2)u_1 = c_{11}\frac{\partial^2 u_1}{\partial x_1^2} + c_{12}\frac{\partial^2 u_2}{\partial x_1 \partial x_2} + c_{13}q\frac{\partial u_3}{\partial x_1} + c_{66}[\frac{\partial^2 u_1}{\partial x_2^2} + \frac{\partial^2 u_2}{\partial x_1 \partial x_2}]$$

$$+ c_{44}q\frac{\partial u_3}{\partial x_1} + \frac{\partial c_{11}}{\partial x_1}\frac{\partial u_1}{\partial x_1} + \frac{\partial c_{12}}{\partial x_1}\frac{\partial u_2}{\partial x_2} + \frac{\partial c_{13}}{\partial x_1}qu_3 + \frac{\partial c_{66}}{\partial x_2}[\frac{\partial u_1}{\partial x_2} + \frac{\partial u_2}{\partial x_1}] \tag{3}$$

$$(-\omega^2 \rho + c_{44}q^2)u_2 = c_{11}\frac{\partial^2 u_2}{\partial x_2^2} + c_{12}\frac{\partial^2 u_1}{\partial x_1 \partial x_2} + c_{13}q\frac{\partial u_3}{\partial x_2} + c_{66}[\frac{\partial^2 u_2}{\partial x_1^2} + \frac{\partial^2 u_1}{\partial x_1 \partial x_2}]$$

$$+ c_{44}q\frac{\partial u_3}{\partial x_2} + \frac{\partial c_{11}}{\partial x_2}\frac{\partial u_2}{\partial x_2} + \frac{\partial c_{12}}{\partial x_2}\frac{\partial u_1}{\partial x_1} + \frac{\partial c_{13}}{\partial x_2}qu_3 + \frac{\partial c_{66}}{\partial x_1}[\frac{\partial u_1}{\partial x_2} + \frac{\partial u_2}{\partial x_1}] \tag{4}$$

$$(-\rho\omega^2 + q^2 c_{33} - c_{44}(\frac{\partial^2}{\partial x_1^2} + \frac{\partial^2}{\partial x_2^2}))u_3 - (\frac{\partial c_{44}}{\partial x_1}\frac{\partial u_3}{\partial x_1} + \frac{\partial c_{44}}{\partial x_2}\frac{\partial u_3}{\partial x_2}) =$$

$$= -q(c_{13} + c_{44})(\frac{\partial u_1}{\partial x_1} + \frac{\partial u_2}{\partial x_2}) - q(\frac{\partial c_{44}}{\partial x_1}u_1 + \frac{\partial c_{44}}{\partial x_2}u_2)] \tag{5}$$

In deriving these equations, we first made substitution $u_3 = -iu_3'$ and then renamed the variable again as $u_3' \equiv u_3$.

From the invariance of the system of Eqs. (3-5) regarding reflection operations in these planes four possible types of solution follow [11]:

(1) Dilatational (D): $u_1^{AS}(x_1, x_2); u_2^{SA}(x_1, x_2); u_3^{SS}(x_1, x_2) \to u_i^D$;

(2) Flexural₁ (Flex1): $u_1^{AA}(x_1, x_2); u_2^{SS}(x_1, x_2); u_3^{SA}(x_1, x_2) \to u_i^{F_1}$;

(3) Flexural₂ (Flex2): $u_1^{SS}(x_1, x_2); u_2^{AA}(x_1, x_2); u_3^{AS}(x_1, x_2) \to u_i^{F_2}$ and

(4) Shear (Sh): $u_1^{SA}(x_1,x_2); u_2^{AS}(x_1,x_2); u_3^{AA}(x_1,x_2) \to u_i^{Sh}$, where S (A) means evenness (oddness) of the function in respect of the operation of sign conversion of the corresponding variable:

$$f(x_1,x_2)=f(-x_1,x_2)=f(x_1,-x_2)\to f^{SS}(x_1,x_2); \quad f(x_1,x_2)=-f(-x_1,x_2)=-f(x_1,-x_2)\to f^{AA}(x_1,x_2)$$

and so on.

In the rectangular wire ($d_1=d_2$) the degeneracy takes place and Flexural$_1$ and Flexural$_2$ polarizations become indistinguishable.

The displacement vector of the heterowire has the form:

$$\vec{U}(x_1,x_2,x_3)=\frac{1}{\sqrt{L_3}}\sum_{\alpha,n,q}A_n^{(\alpha)}(q,t)\vec{w}_n^{(\alpha)}(x_1,x_2,q)e^{-iqx_3}\,,\qquad(6)$$

where $A_n^{(\alpha)}(q,t)$ are the amplitudes of the normal mode with polarization α ($\alpha=D,Flex1,Flex2,Sh$) from the branch n with wavenumber q. Vectors $\vec{w}$ are satisfied to the normalized conditions:

$$\int\rho(x_1,x_2)\vec{w}_n^{(\alpha)}(x_1,x_2,q)\vec{w}_n^{(\alpha')*}(x_1,x_2,q)dx_1dx_2=\tilde{\rho}_n^{(\alpha)}(q)\delta_{nn'}\delta_{\alpha\alpha'}\qquad(7)$$

$$\int\vec{w}_n^{(\alpha)}(x_1,x_2,q)\vec{w}_n^{(\alpha')*}(x_1,x_2,q)dx_1dx_2=\delta_{nn'}\delta_{\alpha\alpha'}\qquad(8)$$

where integrals in Eqs. (7) and (8) are taken over the surface of heterowire cross-sectional plane.

In the case of the clamped boundaries the displacement vector components are zero on the outer surfaces of the wire:

$$w_1=w_2=w_3=0\,.\qquad(9)$$

3. Results and discussion

The solutions of Eqs. (3-5) have been found numerically using the finite difference method. The calculations were carried out for the nanowires with the cross-section 2 nm x 3 nm embedded into "acoustically slow" plastic barrier and "acoustically fast" AlN barrier. The complete cross-sections of heterowires were 4 nm x 6 nm and 6 nm x 9 nm.

For the investigation of the influence of the barriers the wires without barriers were also considered with cross-section equal to (i) cross-section of the heterowires core (2 nm x 3 nm) and to (ii) complete cross-section of the heterowires (4 nm x 6 nm or 6 nm x 9 nm). The values of material parameters, used in our calculations were taken from Refs. [13, 16]. Due to a large number of phonon branches of all polarizations present in the rectangular nanowire we mostly represent and discuss data for the dilatation polarization. The number n of quantum branches (levels) in the wire can be expressed as $n_{max}=d_1d_2/(4a_1a_2)$, where a_1,a_2 are lattice constants in the cross-sectional plane of the wire. So the number of quantified branches in wire is $d/(2a)$ times greater than in the planar structure and growth $\sim d^2$ with the increase of the cross-section of the wire.

The dispersion curves of the dilatational polarization are presented in Fig. 1 for GaN wire of 2nm x 3nm cross-section (Fig. 1(a)); for GaN wire of 4 nm x 6 nm cross-section (Fig. 1(b); for GaN/AlN heterowire of 4 nm x 6 nm cross-section with GaN core of 2 nm x 3 nm cross-section (Fig. 1(c)) and for GaN/plastic heterowire of 4 nm x 6 nm cross-section with GaN core of 2 nm x 3 nm cross-section. In the considered case, when the wire axis is directed along reference axis c, a(GaN) = 0.318 nm and a(AlN) = 0.311 nm (where a is the lattice constant in the plane perpendicular to axis) [16].
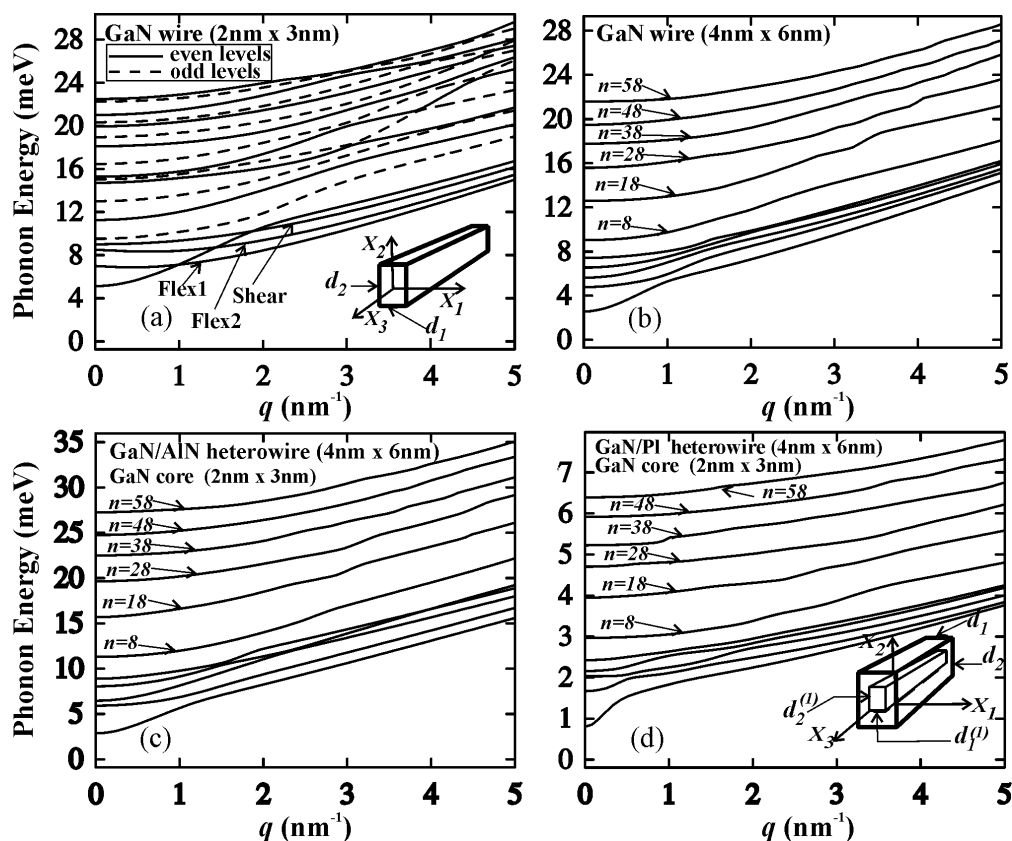
Fig.1. Phonon energy spectrum as functions of the phonon wave number q for (a) GaN wire with 2 nm x 3 nm cross-section (ground levels $n = 0$ are given for all polarizations); (b) GaN wire with 4 nm x 6 nm cross-section; (c) GaN/AlN heterowire with 4 nm x 6 nm cross-section and for (d) GaN/Pl heterowire with 4 nm x 6 nm cross-section. The results are shown for dilatational polarization.

Therefore in GaN wire of 2 nm x 3 nm cross-section the number of phonon quantum branches $n_{max} = 15$ for each polarization. In the wires with cross-section of 4 nm x 6 nm n_{max} is already equal to 59, but in the heterowires of 6 nm x 9 nm cross-section $n_{max} = 135$. Since the lattice constants for GaN and AlN are similar, the calculation of $n_{max} = d_1 d_2 /(4a^2)$ for the GaN/AlN heterowire gives approximately the similar values of n_{max} at the using of $a(GaN)$ or $a(AlN)$. In the case of the plastic material the characteristic constant $a(Pl)$, playing the role of the lattice constant can be larger than $a(GaN)$. As a result, the computation of n_{max}, using the value of $a(GaN)$ gives rather overestimated value of n_{max}. Remaining in the limit of continual approximation it is difficult to determine precisely the position of high level. However, the high branches do not participate in the majority of representing interest effects. In Figs.1(b)-1(d) 5 lowest levels and higher levels with numbers 8, 18, 28, 38, 48, and $n_{max} = 58$ are depicted.

The main conclusion from the obtained results is as follows. All energy levels are dimensionally quantized and the cross-sectional sizes of the wire and difference in the elastic constant between the heterowire core and barrier considerably influence the lower part of the energy spectrum.

As one can see from the comparison of the graphs in Figs. 1(a) and 1(b) the reduction of the wire cross-section leads to the reinforcement of the size-quantization in the lower part of spectrum but weakly influences the structure and position of higher energy levels. It is explained by the fact that position of the higher levels is determined by the inverse value of the lattice parameter $1/a$ whereas dimensional quantization in the lower part of spectrum depends on $1/d$, i.e. it is determined by the wire sizes. The influence of the elastic properties of the barriers is shown very strongly in the energy spectra of the heterowires. "Acoustically slow" barriers narrowed spectrum but "acoustically fast" widened it. In the GaN wire of 4 nm x 6 nm cross-section (see Fig. 1 (b)) the first ten phonon levels are concentrated in the energy interval of 9.5 meV, while the whole spectrum $\hbar\omega(q=0)$ is placed in the interval 22 meV. In the GaN/plastic heterowire (Fig. 1 (d)) the same number of lower levels is concentrated in the considerably less energy interval of 3 meV. But in the case of GaN/AlN heterowire first 10 levels are in the 11,9 meV energy interval. All spectra at $q=0$ are placed in interval of 27,3 meV.

The described modifications of the phonon energy spectrum in the wires, embedded into acoustically mismatched shell can become the important element of the phonon engineering.
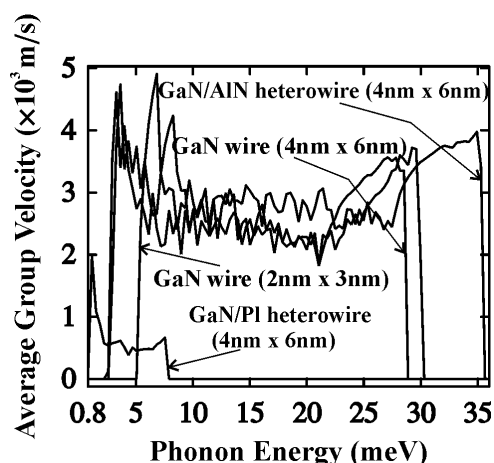

Fig.2. Averaged phonon group velocities as a function of the phonon frequencies for different GaN wires and different heterowires.

Group velocity of the phonon plays an important role in the phenomena of heat conductivity. The group velocities averaged over all quantum branches from $n = 0$ to n_{max} and over all polarization types (D, Flex1, Flex2, Sh) are given by:

$$\overline{v}(\omega) = \frac{1}{4}\sum_{\alpha} \frac{g(\omega)}{\sum_{n(\omega)} (v_n^{\alpha}(\omega))^{-1}}, \qquad (10)$$

In this formula the summing up is carried out by the numbers of dispersion branches n, containing the frequency ω, but $g^{(\alpha)}(\omega)$ is the number of given branches. Curves $\overline{v}(\omega)$ (see Fig. 2), calculated in accordance with the given formula, are strongly oscillating due to the presence of many phonon branches and sharp changes of the function $(v_n^{(\alpha)}(\omega))^{-1} = \dfrac{dq_n^{(\alpha)}(\omega)}{d\omega}$.

So, in Fig. 2 "smoothed" curves without minor vibrations are presented. Due to the size quantization the reducing of the phonon group velocities takes place in the slab in comparison with their values in the bulk at the same values of wave vectors q (so called slab-effect). In the wires, due to the lateral confinement, this effect is shown more strongly. Moreover selecting the elastic properties of the barriers we can influence considerably the value of the phonon group velocities. From the comparison of the graphs in Fig. 2 one can see that plastic

(AlN) barriers decrease (increase) sound velocity in the heterowire in comparison with GaN wire without barriers. This effect is further reinforced if the barrier thickness increases.

Simple averaging of the elastic modules and mass densities in the structure does not allow explaining such strong influence of the barriers. The physical origin of the described effects is redistribution of the displacements $\vec{w}_n^{\alpha}(x_1, x_2, q)$ in the cross-sectional plane of the heterowire.
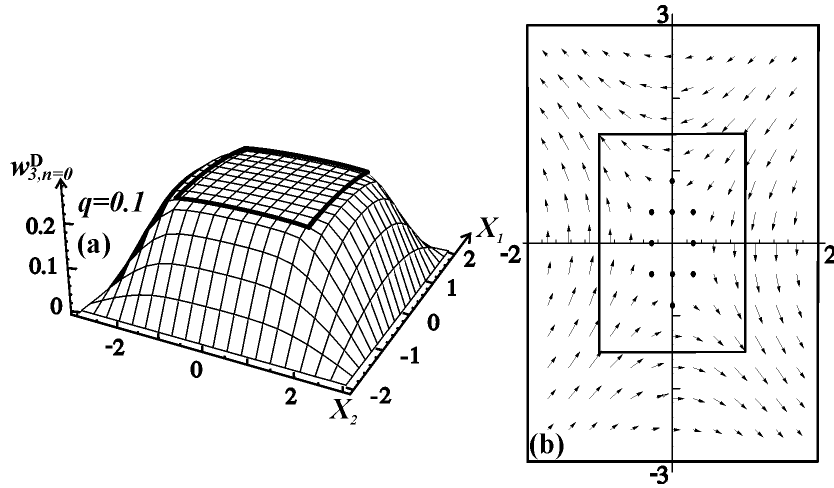
Fig.3. Distribution of the displacement vector components of the normal dilatational mode (n=0, q=0.1) in the cross-sectional plane of GaN/Pl heterowire: (a) the component $w_3(x_1, x_2, q = 0.1)$ and (b) the vector $\vec{w}_{\perp}(x_1, x_2, q = 0.1)$.
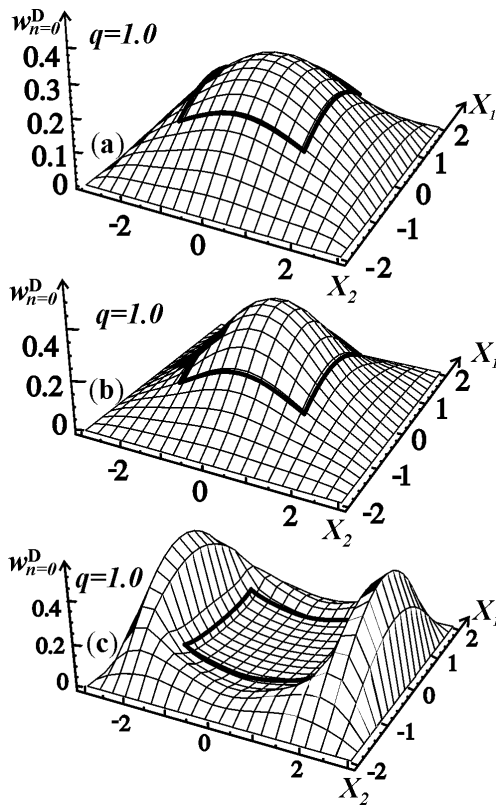
Fig.4. Distribution of the displacement module $w = \sqrt{w_1^2 + w_2^3 + w_3^2}$ of the normal dilatation mode (n=0, q=1.0). The results are shown for: (a) GaN wire; (b) GaN/AlN heterowire; (c) GaN/Pl heterowire.

Fig.5. The same as in Fig.4 but for the phonon mode (n=4, q=1.0).

109

The distribution of the displacement vector component $w_3^D(x_1, x_2, q = 0.1\,\text{nm}^{-1})$ and of the vector $\vec{w}_\perp^D(x_1, x_2, q = 0.1\,nm^{-1})$ in the wire cross-section are shown in Fig. 3 (a, b) for the dilatational mode. One can see from these figures that displacements of given mode are mainly concentrated in the "acoustically slow" plastic barrier of the heterowire.

The dependences of the distribution of the displacement vector module $w(x_1, x_2, q) = \sqrt{w_1^2 + w_2^2 + w_3^2}$ on the value of n ($n = 0, 4, 8$) are presented in Figs. 4-6. In GaN/Pl heterowire for all values of n the displacements are concentrated in Pl barrier and practically absent in GaN core (see Figs.4 (c)-6 (c)). If GaN is the quantum well of the nanostructure the weakening of the electron-phonon interaction will happen in it.
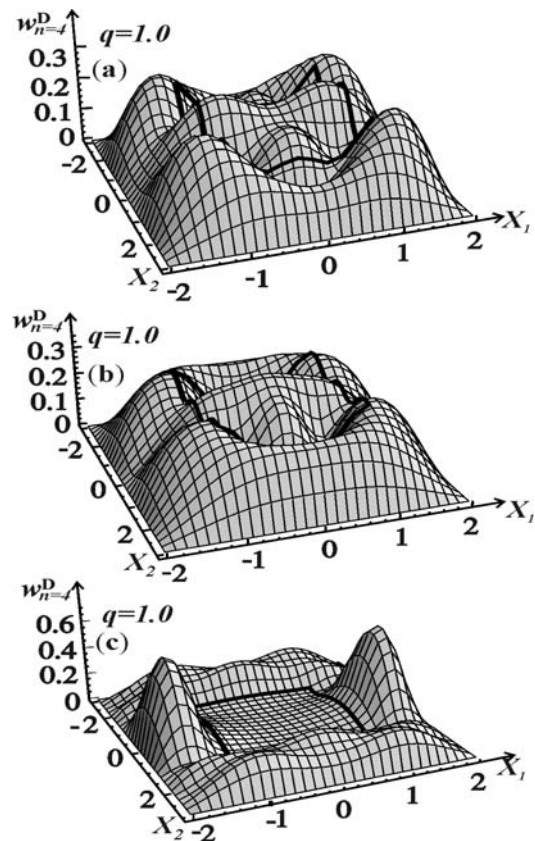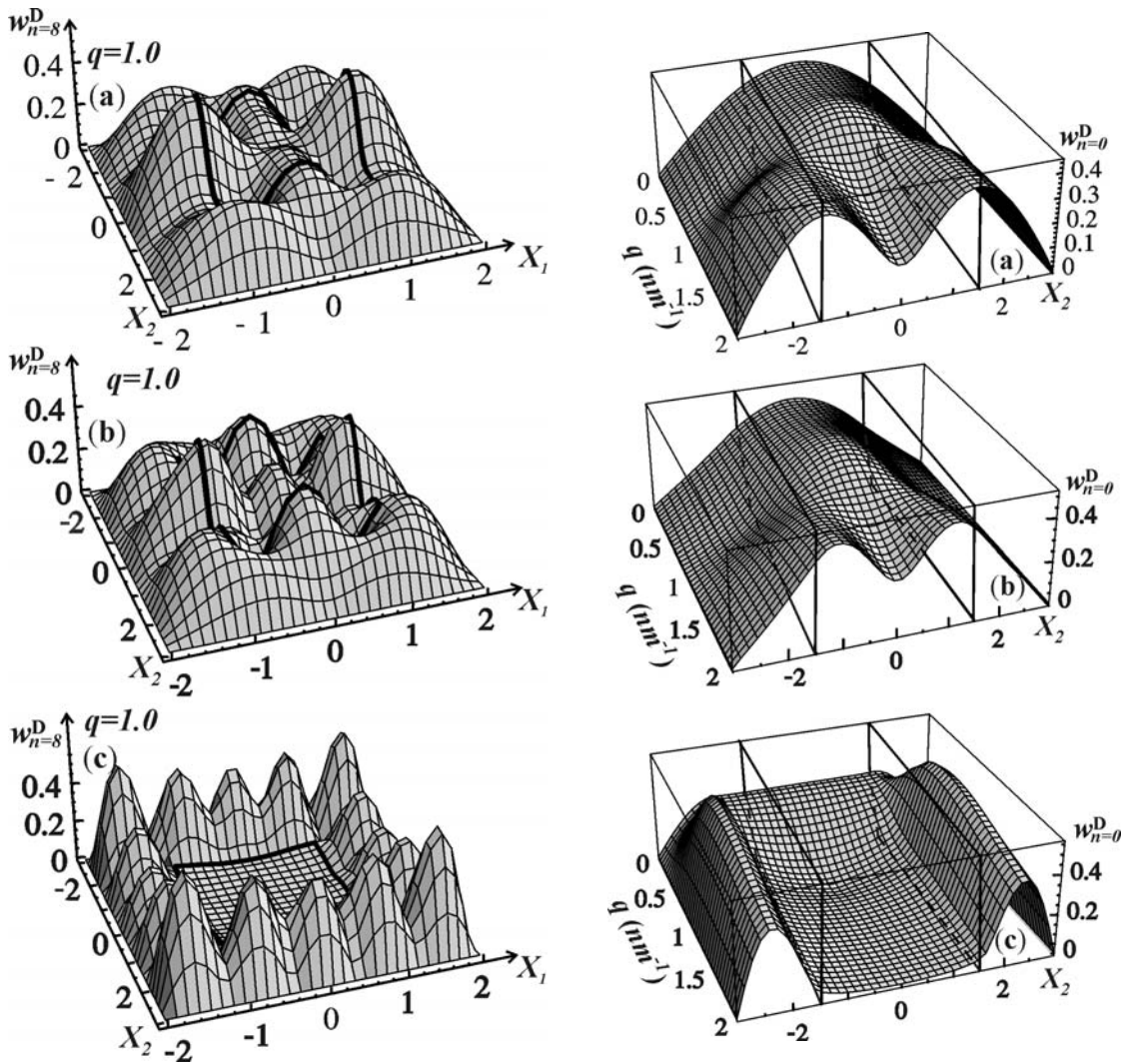

Fig.6. The same as in Fig.4 but for the phonon mode ($n=8$, $q=1.0$).

Fig.7. Distribution of the displacement vector module $w_{n=0}^D(x_1 = 0, x_2, q)$ on dependence on the phonon wavenumber q for (a) GaN wire, (b) GaN/AlN heterowire and (c) GaN/Pl heterowire in the cross-sectional plane $x_1 = 0$.

The decrease of the w function takes place in the GaN/AlN heterowire in the external AlN region in comparison with its values in GaN wire (see Figs. 4 (b)-6 (b)). Besides that, in the case $n = 4$ the central saddle point in GaN wire is transforming in the local peak in GaN/AlN heterowire. But in the case $n = 8$ the local minimum in the center of the GaN wire transforms also in the local peak. The latter should lead to the enhancement of the electron-phonon interaction in GaN core of the heterowire.

For the description of the dependence of the displacement vector module distribution on q the surfaces $w_{n=0}^D(x_1 = 0, x_2, q)$ and $w_{n=2}^D(x_1 = 0, x_2, q)$ are shown in Figs. 7 and 8 correspondingly for the GaN wire (a), GaN/AlN heterowire (b) and GaN/Pl heterowire (c). These graphs describe the evolution of the w function in the cross-section plane $x_1 = 0$. As one can see from these figures, the amplitude of the displacements increases in the "acoustically slow" barriers of GaN/Pl heterowires (see. Fig.7 (c), 8 (c)) and decreases in the "acoustically fast" barriers of GaN/AlN heterowires (see. Fig.7 (b), 8 (b)) with increasing of the value of q. General tendency consists in the accumulation of the displacements in the "acoustically slow" material with the increasing of both n and q (phonon depletion and accumulation effects in core wire).

In consequence of insignificant difference in the acoustic parameters of GaN and AlN in GaN/AlN heterowire the effect of the redistribution of deformations is not exhibited so strikingly as in GaN/Pl heterowire.
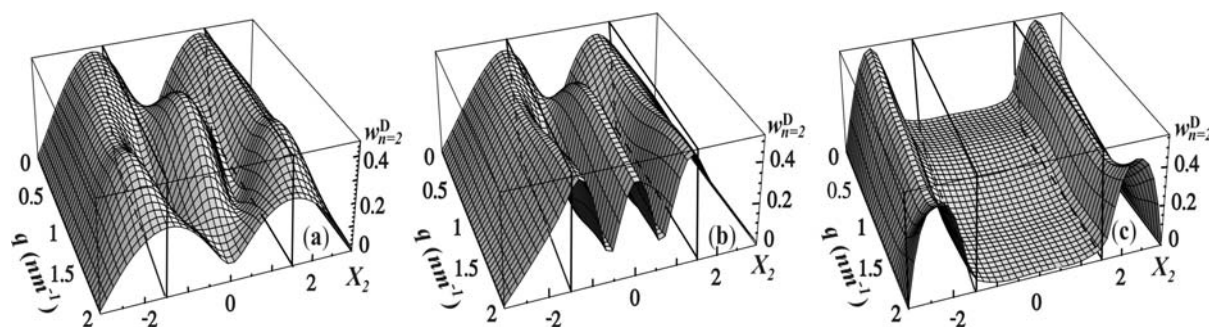
Fig.8. The same as in Fig.7 but for the phonon modes $n = 2$.

4. Conclusion

The acoustic properties of rectangular GaN wires covered by elastically dissimilar barriers with clamped outer surfaces had been considered. The equations of motion were solved numerically taking into account the non-uniform distribution of the elastic properties and mass densities in nanowires. There were obtained the phonon energy spectra and phonon group velocities. The spatial distributions of the displacement vectors of the normal modes in the wire cross-section had been described. It was established that "acoustically slow" barriers "compress" the phonon energy spectrum but "acoustically fast" ones "widen" it. It was also shown that acoustically dissimilar barriers strongly influence the phonon group velocities, increasing or decreasing them, depending on material of the shell. The established effects should have important manifestations in the thermal processes and electron-phonon phenomena in the nanodimensional heterowires.

Acknowledgements

References

[1] Physical Acoustic (Academic Press, New York, 1964) edited by W.P. Meson, vol. I, part A.

[2] S.M. Rytov, Akust. Zh. 2, 71 (1956) [Sov. Phys. – Acoust., 2, 67 (1956)].

[3] C. Colvard, T.A. Gant, M.V. Klein, R. Merlin, R. Fisher, H. Morkoc, A.C. Gossard, Phys. Rev. B 31, 2080 (1985).

[4] N. Bannov, V. Aristov, V. Mitin and M.A. Stroscio, Phys. Rev. B 51, 9930 (1995).

[5] A. Svizhenko, A. Balandin, S. Bandyopadhyay and M.A. Stroscio, Phys. Rev. B 57, 4687 (1998).

[6] M.A. Stroscio, K.W. Kim, S.G. Yu, A. Ballato, J. Appl. Phys.76, 4670 (1994).

[7] V.G. Grigoryan and D.G. Sedrakyan, Akust. Zh. 29, 470 (1983).

[8] S. Ruffo, M. Dutta and M. Stroscio, J. Appl. Phys. 93, 2900 (2003).

[9] L.O. Lazarenkova and A.A. Balandin, Phys. Rev. B 66, 245319 (2002).

[10] X. Lu, J.H. Chu, W.Z. Shen, J. Appl. Phys. 93, 1219 (2003).

[11] N. Nishiguchi, Y. Ando and M. Wybourne, J.Phys.: Condens. Matter. 9, 5751 (1997)

[12] A. Balandin and K.L. Wang, Phys. Rev. B 58, 1544 (1998).

[13] E.P. Pokatilov, D.L. Nika and A.A. Balandin, J. Superlatt. Microstruct. 33, 155 (2003).

[14] E.P. Pokatilov, D.L. Nika and A.A. Balandin, J. Appl. Phys. 95, 5625 (2004).

[15] E.P. Pokatilov, D.L. Nika and A.A. Balandin, Appl. Phys. Lett. 85, 825 (2004).

[16] I. Vurgaftman, J.R. Meyer and L.R. Ram-Mohan, J. Appl. Phys. 89, 5815 (2001).

COMPUTATIONAL STUDY OF NON-STATIONARY CLUSTER SIZE DISTRIBUTION AND RATE OF NUCLEATION IN CASE OF PRE-EXISTING CLUSTERS

V. Gamurari[*], F. Paladi[*§], V. Eremeev[§] and M. Al-Sabayleh[#]

[*]Department of Theoretical Physics, State University of Moldova, A.Mateevici str.60, Chisinau, MD-2009, Republic of Moldova
[§]Department of Engineering and Computer Sciences, Free International University of Moldova, Vlaicu Parcalab str.52, Chisinau MD-2012, Republic of Moldova
[#]Department of Physics, Mutah University, Jordan

The dynamics of a cluster-type system formed by constant total number of molecules, M, is studied when clusters change their sizes by nearest-size transitions (the Szilard model) with time-dependent boundary conditions and non-zero initial cluster size distribution. We compare these results to those reported previously [5], when non-stationary cluster size distribution was considered under the condition that only monomers are present in the system at the initial moment $t=0$, and describe the effect of arbitrary pre-existing clusters on the time evolution of the interacting clusters with different sizes, n. The average group size problem is also solved, and the process of relaxation in the system is studied.

1. Introduction

The process of nucleation can begin in the presence of clusters formed previously in the system, and one may expect that these pre-existing clusters could be a factor affecting the kinetics of nucleation [1–4]. For instance, the pre-existing clusters are able to grow spontaneously right after initial moment and will thus cause an increase in the non-stationary nucleation rate at the earliest stage of the process. Also, the pre-existing clusters can exert influence on the concentration of supernuclei in the system and the nucleation delay-time, so the effects of the pre-existing clusters on the rate of non-stationary nucleation [2], homogeneous nucleation of crystals in vitrified melts, and 2d and 3d heterogeneous nucleation of condensed phases on foreign and own substrates [1, 3] were widely studied.

In general, nucleation itself is the process of random generation of those nanoscopically small formations of the new phase that have the ability for irreversible overgrowth to macroscopic sizes. In case of the cluster approach, these nanoscopically small formations of the new phase are considered as a group of clusters of a certain number n of molecules (or atoms) in them. The cluster itself is regarded as separated from the old phase by a phase boundary and that makes it possible to say which of all M molecules in the system are still in the old phase and which of them already belong to the new phase [1]. In [5] a model based on the cluster theory was developed and used to simulate the dynamics of complex systems with different sizes M. In particular, the role of attachment probability was described by comparison between this model and other kinetic models of random growing networks and herding phenomena, and the size effect on the formation of clusters, under the condition that only monomers are present in the system at the initial moment, was elucidated. Therefore, it is worth looking further into the role of pre-existing random generated clusters with different

Phone: +373-22-577584, Fax: +373-22-244248, E-mail: inginerie@ulim.md

sizes in the non-stationary cluster size distribution, and we present in this paper our findings relating to this intriguing matter.

2. The Model

In [5] a detailed description of the model is given. The following two basic assumptions, which allow a mathematical formalism to be developed, are indispensable in the framework of the Szilard model: 1) There exist clusters in the initial state which consist of different number n of molecules (or atoms) ($n=1, 2, \ldots$); 2) Transformations of n-sized clusters into m-sized ones at time t occur with certain frequencies f_{nm} ($n, m=1, 2, \ldots$). Denoting $f_n=f_{n,n+1}$, $f_{n-1}=f_{n-1,n}$, $g_n=f_{n,n-1}$, $g_{n+1}=f_{n+1,n}$, where $f_{nm}=0$ for $|n-m|>1$ and $f_{nm}\neq0$ for $|n-m|=1$, the clusters will change size by nearest-size transitions. This is illustrated in Figure 1 in which the arrows symbolize the number of forward $n\rightarrow n+1$ and backward $n\rightarrow n$-1 transitions, and the quantity f_nZ_n, for example, gives the number of $n\rightarrow n+1$ transitions undergone by the n-sized clusters per unit time, divided by the number of interacting clusters $N(t)$, where $N(t) = \sum_{k=1}^{M} n_k(t)$, M is a number of molecules (or atoms) in a closed system ($M=const$), and $n_k(t)$ is number of groups (clusters) of size k at time t. The evolution of the process is sought to be described by the function $Z_n(t)$, which represents the solution of the kinetic master equation and characterizes the time-dependence of the concentration of clusters of size n:

$$\frac{dZ_n(t)}{dt} = f_{n-1}Z_{n-1}(t) - g_nZ_n(t) - f_nZ_n(t) + g_{n+1}Z_{n+1}(t) \quad . \quad (1)$$

By definition, $f_0=0$, $g_1=0$, $Z_{M+1}=0$, and $Z_n(t)$ and M are connected by the relation

Fig.1. Schematic presentation of the possible changes in the size of a cluster of n molecules by nearest-size transitions. The quantity of n-sized clusters diminishes because of $n\rightarrow n$-1 and $n\rightarrow n+1$ transitions, and increases due to n-1$\rightarrow n$ and $n+1\rightarrow n$ transitions, and these processes are represented by arrows leaving size n and those ending at size n, respectively.

$N(t)\sum_{n=1}^{M} nZ_n(t) = M$, where the initial cluster size distribution $Z_n(0)$ is considered to be *a priori* known. Note that one time step in this formulation corresponds to one update in the numerical simulation under time-dependent $Z_1(t) \neq 0$ and $Z_M(t)\equiv0$, and non-zero random initial cluster size distribution $Z_n(0)\neq0$ ($n=1, 2, 3, \ldots, M$-1). So equation (1) becomes a set of M-1 homogeneous ordinary linear differential equations of first order in the M-1 unknowns $Z_1(t)$, $Z_2(t)$, $Z_3(t)$, $\ldots$, $Z_{M-1}(t)$. In this case the problem can be solved in a straightforward manner, and the solution $Z_n(t)$ given in [5] takes a new form without the stationary cluster size distribution part, and $i=1, 2, \ldots, M$-1. The d_i is the only parameter affected by the non-zero initial cluster size distribution, $Z_n(0)\neq0$, and now it is given by the following determinant of order M-1:
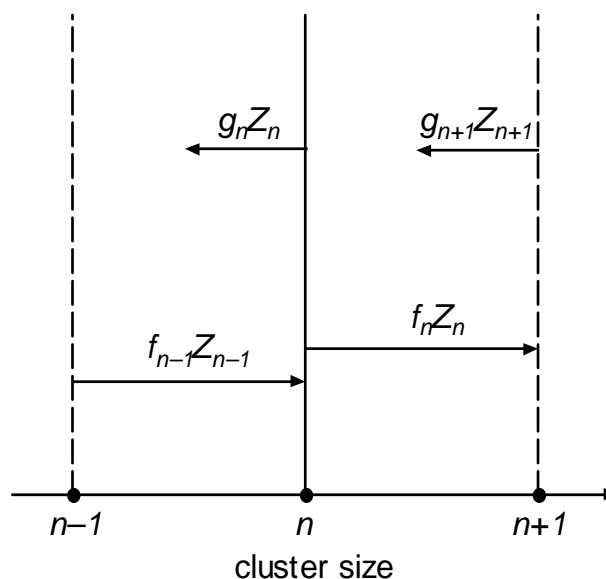
$$d_i = \begin{vmatrix} a_{11} & a_{12} & a_{13} & \cdots & a_{1,i-1} & Z_1(0) & \cdots & a_{1,M-1} \\ a_{21} & a_{22} & a_{23} & \cdots & a_{2,i-1} & Z_2(0) & \cdots & a_{2,M-1} \\ \vdots & \vdots & \vdots & \vdots & \vdots & \vdots & \vdots & \vdots \\ a_{M-1,1} & a_{M-1,2} & a_{M-1,3} & \cdots & a_{M-1,i-1} & Z_{M-1}(0) & \cdots & a_{M-1,M-1} \end{vmatrix}, \qquad (2)$$

where a_{ni} are the same constants described in [5] with the help of transition frequencies f_n and g_n.

We can now determine the non-stationary rate $J(t)$ of nucleation at pre-existing clusters in the system. For $n=1, 2, \ldots, M$-1

$$J(t) = \sum_{i=1}^{M-1} (d_i / d')(f_n a_{n,i} - g_{n+1} a_{n+1,i}) \exp(-\lambda_i t), \qquad (3)$$

where $\lambda_i > 0$ is the ith eigenvalue, i.e. the ith root of the characteristic equation [5], and d' is a determinant of order M-1:

$$d' = \begin{vmatrix} a_{11} & a_{12} & a_{13} & \cdots & a_{1,i-1} & a_{1,i} & \cdots & a_{1,M-1} \\ a_{21} & a_{22} & a_{23} & \cdots & a_{2,i-1} & a_{2,i} & \cdots & a_{2,M-1} \\ \vdots & \vdots & \vdots & \vdots & \vdots & \vdots & \vdots & \vdots \\ a_{M-1,1} & a_{M-1,2} & a_{M-1,3} & \cdots & a_{M-1,i-1} & a_{M-1,i} & \cdots & a_{M-1,M-1} \end{vmatrix}. \qquad (4)$$

For $M>5$ we must resort to numerical methods for solving the problem, because the exact analytical solution can be found only for $M \leq 5$.

3. Results and Discussion

Time evolution of the interacting n-sized clusters was numerically simulated for $M=7$ and $g_i/f_i = \{0.229, 1.458, 2.466, 2.835, 0.686\}$, $i=2, 3, \ldots, 6$, and the results for $n=2, 3, \ldots, 6$ in both cases of arbitrary pre-existing clusters (solid curves) and when only monomers are present in the system at the initial moment $t=0$ (broken curves) are shown in Figure 2.
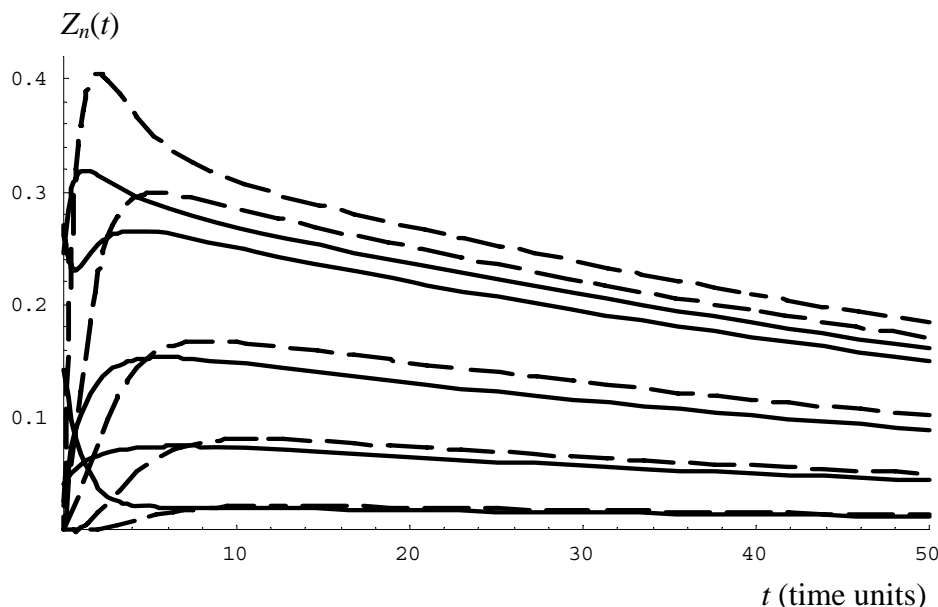

Fig.2. Time dependences of the concentration of clusters of size n in case of arbitrary pre-existing clusters (solid curves) and when only monomers are present in the system at the initial moment (broken curves) for $M=7$ ($n=2, 3, 4, 5$ and 6, from top to bottom).

We can conclude that the impact of pre-existing random generated clusters with different sizes n=1, 2, …, 6 on the non-stationary cluster size distribution in the short time limit depends on the size of clusters, and it is stronger for smaller groups. For large t the effect vanishes, and this is expected since the pre-existing clusters cannot affect the cluster distribution at equilibrium. They can only shorten the time needed for the establishment of the final distribution, and this fact can be clearly seen on the figure, regardless of the size n of clusters. Time dependence of the average group sizes, $M/N(t)$, represented in Figure 3 for both types of initial conditions by solid and broken curves respectively, also indicates that the system relaxes towards equilibrium faster in case of pre-existing random generated clusters. The sum $\sum_{n} nZ_n(t)$ was calculated between the limits 2 and M-1. In particular, it is important to note that these results give us more flexibility in choosing initial conditions, especially in case of evolution of large groups in the time limit $t\to\infty$, i.e. for late stages of cluster formation, because the accuracy of analytical solutions will not be affected since the

Fig.3. Time dependences of the average group sizes for M=7. Solid curve represents the result in case of pre-existing random generated clusters with different sizes n=1, 2, … 6, and broken curve that for only $Z_1(0) \neq 0$.

difference between particular results obtained by applying different initial conditions is insignificant.

In this paper the non-stationary cluster size distribution in a network of agents (i.e. atoms or molecules) which evolves randomly has been studied at early and late stages of clusters formation, when they are expected to grow and decay mainly by gaining and losing monomers, because a relatively low cluster concentration at the early stage and an immobile stable structure at the late stage would require a single-agent mechanism of cluster formation. The advanced stage could be characterized additionally by merge of clusters of various sizes into a new bigger one (coagulation effect), and the contacts between them begin to have an increasingly important role in the size changes. So the more specific features, such as new agents entering the system (open structure), preferential attachment, coagulation effect etc, have been applying to the system to study both random and preferential dynamics of cluster-structures.

References

[1] D. Kashchiev, Nucleation: Basic Theory with Applications, Butterworth-Heinemann, Oxford, 2000.
[2] D. Kashchiev, Surface Sci. 18, 389 (1969).
[3] K.F. Kelton, A.L. Greer, C.V. Thompson, J. Chem. Phys. 79, 6261 (1983).
[4] B. Shizgal, J.C. Barrett, J. Chem. Phys. 91, 6505 (1989).
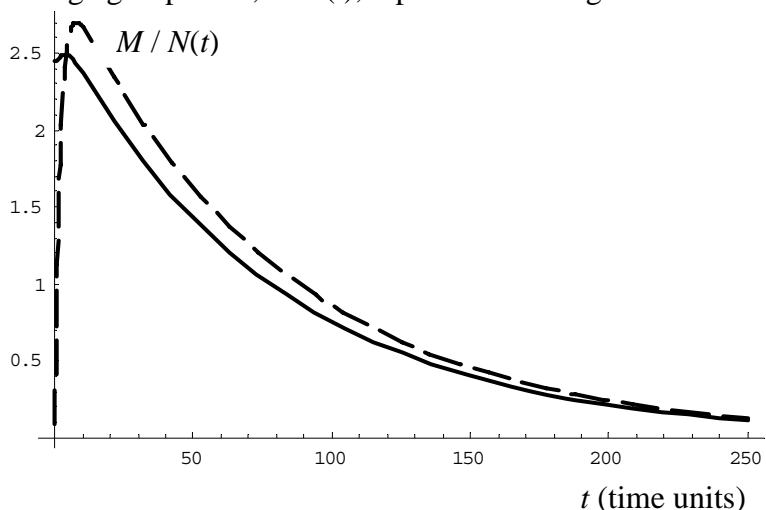[5] F. Paladi, V. Eremeev, Physica A: Statistical Mechanics and its Applications, v. 348, p. 630-640, (2005).

GROUND-BASED OBSERVATION OF SHORTWAVE SOLAR RADIATION DURING SOLAR ECLIPSE ON OCTOBER 3, 2005 IN CHISINAU, MOLDOVA

A. Aculinin, V. Smicov

Atmospheric Research Group (ARG), Institute of Applied Physics, Academy of Sciences of Moldova, 5 Academiei Str., Chisinau, MD-2028, Republic of Moldova;
E-mail: akulinin@phys.asm.md

Abstract

The influence of partial annular solar eclipse observed during October 3, 2005 onto the variation of shortwave downwelling solar irradiation at the Chisinau site is analyzed. Evaluation of the components of broadband solar radiation from UV-B to near IR falling onto the Earth's surface is presented. Such type of dimming was due to partial annular solar eclipse event with maximum phase of 40%, which resulted in 3.4- 4.5% reduction of daily totals of shortwave downwelling solar radiation.

1. Introduction

Solar eclipse represents the phenomenon of covering the solar disk by moon and as the case it may be characterized as full, annular or partial. Fraction of the surface of the solar disk obscured by the moon during solar eclipse is determined by the time and position given. That phenomenon occurs rather frequently. Every year from 2 to 5 of solar eclipses can be observed all around the world. In each specific place on the Earth's surface solar eclipses are observed on an average one time in few years. For example, there were observed 35 solar eclipses in Moldova of recent 100 years. All these eclipses were characterized as partial ones. The next solar eclipse which can be observed on the territory of Moldova will occur on March 29, 2005 and will be characterized as a partial eclipse. Maximum of solar disk obscuration will consist of 75%.

Solar eclipse represents an interest for investigation because during the solar eclipse there can be observed solar radiation flux decreasing, changing of the optical properties of the atmosphere(spectral transmittance, polarization properties, etc) and meteorological parameters [1-3]. Solar radiation remains the main measurable parameter affected by solar eclipse. The subject of this paper is to investigate variation of the broadband shortwave downwelling solar radiation in the spectral wavelength range from ultraviolet (UV) to near IR during the solar eclipse observed over Moldova on October 3, 2005.

2. Equipment and results of measurements

Since 2003 continuous measurements of broadband shortwave downwelling solar radiation from UV to IR have been carrying out at the ground based solar radiation monitoring station at the Institute of Applied Physics. The station consists of radiometric complex, automatic weather station, ozonometer, and sunphotometer Cimel-318. Radiometric complex is composed of the set of radiometric sensors from Kipp&Zonen such as CM-11 pyranometers, CH-1 pyrheliometer, Photosynthetically Active Radiation (PAR), UV-B and UV-A sensors to measure solar radiation [3]. Stability of optical properties of atmosphere

over the site was checked with collocated and synchronous measurements of spectral aerosol optical depths (AOD) with sunphotometer Cimel-318. Spectral AODs were measured with sunphotometer at seven wavelengths from 340 nm through 1020 nm. Measurements of AOD were fulfilled within the framework of the Aerosol Robotics Network (AERONET) programme, managed by NASA/GSFC [4].

Ordinary solar eclipse took place on October 3, 2005. Moon angular diameter was smaller than the solar one, so in zone of maximum phase the moon didn't obscure the solar disk completely. In Chisinau this solar eclipse was observed as partial annular eclipse with maximum obscuration of solar disk with 40%. Solar eclipse continued from 08:22:23 UTC to 10:46:55 UTC. The maximum of occultation was observed in Chisinau at 09:33:50 UTC.
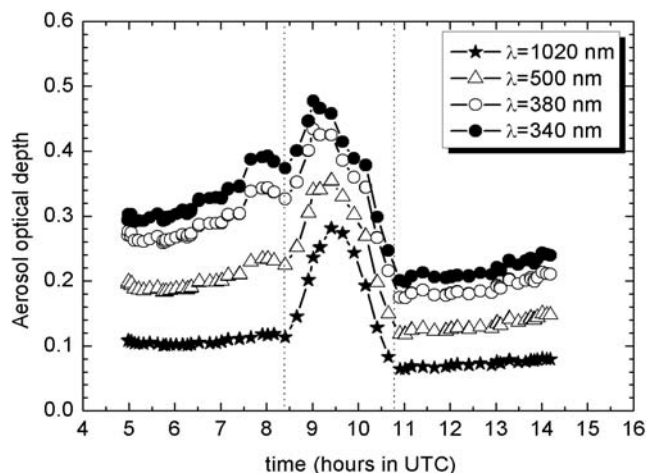

Figure 1. Diurnal variation of spectral AOD $\tau_a(\lambda)$ measured with sunphotometer Cimel-318 at the Chisinau site during solar eclipse event in October 3, 2005.

The overall meteorological conditions were good: cloudless sky with light haze during the whole day and the eclipse period. Diurnal variation of spectral aerosol optical depths $\tau_a(\lambda)$ measured with sunphotometer at selected wavelengths in the UV-visible-near IR range during partial annular solar eclipse is shown in Figure 1. Two vertical dotted lines show beginning and ending of solar eclipse. AODs $\tau_a(\lambda)$ show smooth variation both in the morning and afternoon hours, that confirms the fact of the stability of optical properties of the atmosphere during observation. Some clearance of the atmosphere was observed in the afternoon hours. Spectral aerosol optical depths $\tau_a(\lambda)$ measured in the morning hours are higher than analogous values obtained in the afternoon, i.e. AOD values $\tau_a(\lambda)$ measured at λ=500 nm and averaged over period of time before(in the morning) and after (in the afternoon) solar eclipse were $<\tau_a>$ =0.20 and $<\tau_a>$ =0.13, respectively. For comparison, climatological mean value of AOD $<\tau_a>$ obtained at the Chisinau site over period of observation 1999-2004 equals 0.23 at λ=500 nm. The appearance of distinctive maximum in $\tau_a(\lambda)$ for each of wavelengths during the eclipse event is accounted for by the fact that AODs are deduced using the Langley calibration technique. This technique defines extra-atmospherical constants as input parameters for sunphotometer in the case of clear solar disk. In the case of solar eclipse these constants remain the same as initial ones obtained at the calibration facilities, but incoming solar radiation measured by sunphotometer at the Earth's surface is partially attenuated due to eclipse event only. The appearance of the above mentioned maxima in AOD's cannot be connected with the low transparency of atmosphere due to increase of aerosol loading or cloud effect. It must be considered as artifacts and AODs data collected during eclipse period should be eliminated from the final dataset.

Global components of shortwave downwelling solar radiation were measured with sensors mounted on the stationary platform. Direct and diffuse components of solar radiation were measured with set of sensors installed on moving platform of active sun-tracker 2AP BD. Radiometric data were collected with 1-minute averaging interval. This interval is well suited to observe the impact of transient solar eclipse on measured shortwave downward solar

radiation. Diurnal variation of global and direct components of solar radiation measured at Chisinau site during solar eclipse event on October 3, 2005 is shown in Figure 2 (a,b).

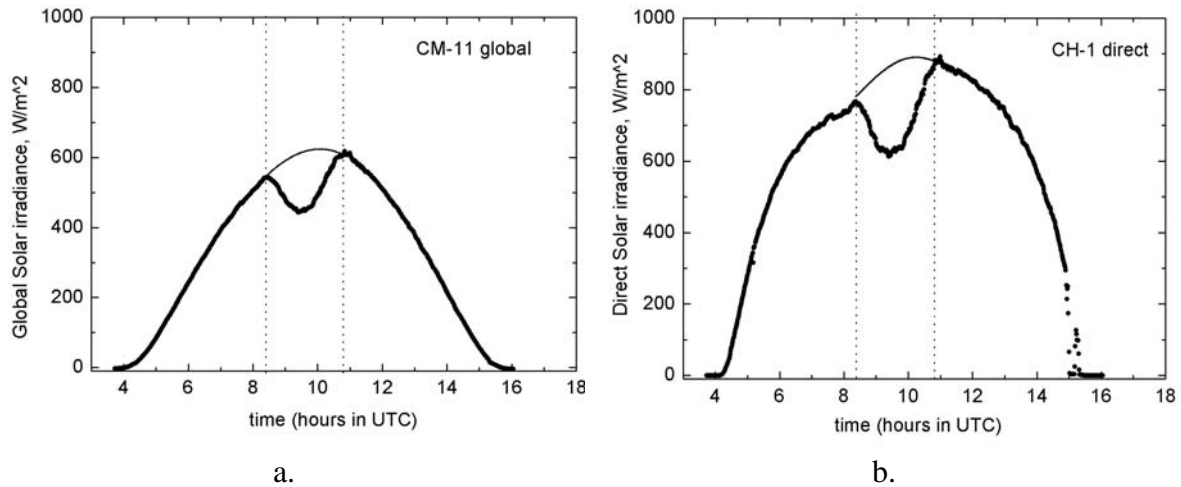a.   b.

Figure 2(a,b). Diurnal variation of global (a) and direct (b) components of shortwave downwelling solar radiation measured at Chisinau site during solar eclipse event on October 3, 2005. Vertical dotted lines correspond to the beginning and ending of eclipse. Thin curves show the expected variation of solar irradiance during eclipse.

It is clearly seen that obscuration of solar disk resulted in temporal dimming or reduction of solar radiation fluxes measured at the Earth's surface. From 08:22:23 UTC shortwave downward solar radiation began to decrease and at 09:33:50 UTC radiative flux reached the minimum. Then it began gradually to increase and at 10:46:55 UTC radiative flux returned to normal value. Appearance of the minimum on the curve, describing diurnal variation of any component of solar radiation, corresponds to the maximum of solar disk obscuration. The analogous variation is typical for diffuse component of solar radiation, UV-B and UV-A radiation, and PAR. Some asymmetry in the shape of curve describing diurnal variation of direct solar radiation (on perpendicular plane) is observed. This was due to the fact that spectral transparency $e^{-\tau(\lambda)}$ of atmosphere in the morning hours was lower than in the afternoon. Expected variation of solar irradiance during eclipse is marked by thin curves in Figure 2(a,b). These modeled relationships are used to evaluate influence of temporal dimming effect caused by solar eclipse. Values of contribution for each of components of broadband solar radiation are computed relatively to the maximum of the phase of solar eclipse, to the sums recorded during the period of eclipse and to the daily totals of solar radiation. Respective values of contribution are presented in Table 1.

Computed values of contributions from dimming effect due to partial annular solar eclipse relative to the maximum of the phase of solar eclipse and to the sums recorded during the period of eclipse ranged from 23.9% to 43.5% and from 12.2% to 20%, respectively. Diffuse component of shortwave solar radiation showed the deepest minimum ~43.5% among other components of solar radiation. This was owing to relative low transparency of the atmosphere with haze. Reduction of daily totals of solar radiation due to solar eclipse varied from 3.4% to 4.5%.

Table 1. The influence of partial solar eclipse onto the components of broadband solar radiation (from UV-B to near IR) falling on horizontal surface. Values of contribution for each of components are computed relative to respective estimated values of solar radiation.

Components of broadband solar radiation	Relative to the maximum of the phase of solar eclipse, %	Relative to the sums during the period of solar eclipse, %	Relative to the daily totals, %
UV-B 280-315 nm (global)	24.1	13.1	4.0
UV-B 280-315 nm (diffuse)	26.1	12.2	3.6
UV-A 315-400 nm (global)	23.9	13.0	3.4
PAR 400-700 nm (global)	25.7	13.6	3.5
Solar 400-1100 nm (global)	27.2	14.4	3.7
Solar 300-2800 nm (global)	26.9	14.4	3.7
Solar 300-2800 nm (diffuse)	43.5	20.0	4.5
Solar 300-4000 nm (direct)	27.7	16.6	3.7

3. Summary and conclusions

This study was confined to the investigation of the responses of broadband shortwave downwelling solar radiative fluxes in the wavelength range from UV to near IR to the partial annular solar eclipse event of October 3, 2005. Shortwave downwelling solar radiation was measured with the radiometric complex at the ground-based station of the Chisinau site. Measurements were fulfilled with 1-minute averaging interval, which was enough to evaluate the impact of a transient solar eclipse on radiative fluxes. Stability of optical properties of atmosphere over the site was checked with collocated and synchronous measurements of spectral aerosol optical depths with sunphotometer Cimel-318 operating within the frames of global AERONET network. The overall meteorological conditions were good: cloudless sky with light haze during the whole day of observation. Diffuse component of shortwave solar radiation showed the deepest minimum ~43.5% among other components of solar radiation. This was owing to relatively low transparency of the atmosphere with haze. Reduction of daily totals of solar radiation due to solar eclipse varied from 3.4% to 4.5%.

References

[1] D. Ahrens, M.G. Iziomon, L. Jaeger, A. Matzarakis and H. Mayers, *Meteorol. Zeitschrift*, v. 10, n. 3, 215-223 (2001).
[2] S.L. Jain, B.C. Arya, A. Kumar, S.D. Ghude and A. Kumar, in Proceed. of the Quadrennial Ozone Symposium (QOS 2004), the Island of Kos, Greece, 1 - 8 June, 2004, 1095-1096 (2004).
[3] A. Aculinin, A. Smirnov, V. Smicov, T. Eck, and A. Policarpov, *Moldavian J. Phys. Sci.,* v.3, n.2, 204-213 (2004).
[4] Holben, et.al., *J. Geophys. Res.*, v.106, 12 067-12 097, (2001).

BLACK SEA INFLUENCE ON FORMATION OF HAIL-HAZARDOUS CUMULONIMBUS CLOUDS IN SOUTH MOLDOVA

V.I. Petrov, I.A. Garaba, E.I. Potapov

Special Service for Active influences on hydrometeorological processes of the Republic of Moldova, Grenoble str.197, Chisinau, Republic of Moldova;
International Laboratory of Solid State Electronics, Academy of Sciences of Moldova, Academiei str.3/3, Chisinau, MD-2028, Republic of Moldova.
E-mail: epotapov@mail.ru

The space-time structure of hail-hazardous cumulonimbus clouds evolving on the sea-breeze fronts in northwestern Black Sea coast for the period of 1996-1999 is investigated with the help of MRL-5. A chart of number of days with radio echo of cumulonimbus clouds with radar reflectivity more than 65 dBZ in days with evolution of sea-breeze fronts is obtained. Statistic characteristics of sea-breeze fronts are presented.

Introduction

South part of the Republic of Moldova is located in close proximity to the Black Sea at the distance 70-100 km. It is known that vicinity of two heterogeneous underlying surfaces, for example land-sea, always leads to appearance of various mesometeorological processes, including evolution of hail-hazardous cumulonimbus clouds (Cb) which are connected with such dangerous weather phenomena as showers, thunderstorms, hail, squall [2,8].

Knowledge of conditions for formation and dynamics of evolution of these Cb is of direct interest for solution the problems of weather modification with the purpose of both decrease of losses from hail and artificial increase of precipitation.

North-western regions near the Black Sea (territory of the south-western part of Odessa province of the Ukraine and South of Moldova) in warm period of the year are characterized by high recurrence of breezes [2]. The breezes are the local mesometeorological processes evolving in coastal regions of oceans, seas, large reservoirs and rivers. Above the land, at a distance from the coast line, a convective instability line, so called sea-breeze front (SBF) is often formed. This is a convergence zone located parallel to the coast line formed as a result of interaction with the day (sea) breeze and weakened and moisty large-scale background flow from the land, where in the presence of unstable stratification cumuli and cumulonimbus clouds are evolved. The sea-breeze front is distinguished by space-time image of TV and IR pictures obtained from meteorological satellites of the Earth or by structure of field of radio-echo of cumulonimbus clouds found by radar. The sea-breeze front penetration depth defined as a distance from the coast line to the external boundary of radio-echo of cumulonimbus clouds (RECC) may reach from 50 to 200 km, covering south regions of the Republic of Moldova, including those where works on protection of agricultural products from hail are constantly carried out [6].

The purpose of the given work is to investigate space-time structure of hail-hazardous cumulonimbus clouds evolving on mesoscale sea-breeze fronts in the north-western regions of the Black Sea on the basis of radar and aerosynoptic data.

For the period (April-September) of 1996-1999 there were analyzed 139 days with evolution of breeze fronts, in 32 cases (days) radio-echo from cumulonimbus clouds with radar reflectivity more than 65 dBZ ($\eta > 65$ dBZ) was observed, and besides several cases of RECC with $\eta > 65$ dBZ were stated during one day.

The observations were carried out with the help of radar MRL-5 in the Kahul special department of the Special service on active influences on hydrometeorological processes of the Republic of Moldova. Photoregistration of all the radar information was carried out in the radius of 300 km in every 15-20 minutes, in the radius of 100 km - in every 10-15 minutes. For the analysis the data of radio-soundings of Odessa and Chisinau stations and charts of baric topography were used.

Main results

In works [2, 3, 6] it is shown that the sea-breeze fronts evolve in weakened field of general circulation of the atmosphere, in unstably stratified and moisty air mass, and in 56% cases come on small-gradient baric fields of high and low pressure. The large-scale background flow is characterized by weakened westerly, north-westerly and northerly winds with the modal velocity 4-7 m/s in the stratum of 850-500 hPa, i.e. by seaward winds that provided divergence of air flows and intensification of convection in the zone of sea-breeze front. In work [3] there was estimated the value of horizontal divergence of wind velocity while sea-breeze front evolving for north-western regions of the Black Sea on the basis of radar measurements of RECC area in the grid 30x30 km from the plan-position indicator (PPI) of the radar MRL-5. The divergence order appeared to equal 10^{-4} s^{-1} being comparable with its value at macroscale atmospheric frontal passage. In the convergence regions (negative divergence) maximal values of radar parameters of RECC are determined.

For the north-western coast of the Black Sea the penetration depth of sea-breezes averages 20-25 km [2, 3]. Average number of days with breezes is 58, but it may oscillate from 50 to 78 [2]. Table 1 shows recurrences of time of RECC appearance on the sea-breeze fronts (A) and time of appearance on them of RECC with radar reflectivity $\eta > 65$ dBZ (B). It is seen from Table 1 that sea-breeze fronts most often evolve in the period from noon to 2 p.m. (50.4%), i.e. in the period of maxima evolution of the day (sea) breeze. Hail-hazardous cumulonimbus clouds most often evolve from 4 p.m. to 6 p.m. (50.5%).

Table 1. Recurrence (%) of time of appearance of RECC (A) and RECC with radar reflectivity $\eta > 65$ dBZ (B) on the sea-breeze fronts for the period of 1996-1999

			Gradation, hour						Sum
			10-12	12-14	14-16	16-18	18-20	20-22	
A	Number of cases		31	70	30	7	1	-	139
	Recurrence, %		22.3	50.4	21.6	5.0	0.7	-	100
B	Number of cases		-	18	44	79	49	5	195
	Recurrence, %		-	9.2	22.6	40.5	25.2	2.5	100

Note. Discrepancy of number of cases of RECC with $\eta > 65$ dBZ and number of days with the sea-breeze fronts is explained by the presence of several cases of RECC with $\eta > 65$ dBZ in the same day.

Table 2 presents the results of radar observations of the sea-breeze fronts for the mentioned period. Table 2 data show that in the breeze period for the north-western regions of the Black Sea coast on the average in 59.9% cases RECC evolution on the sea-breeze fronts is observed, in 23.5% cases of them evolution of RECC with radar reflectivity $\eta > 65$ dBZ is registered.

It follows from tables 1 and 2 that not all breeze circulations are accompanied by formation cloudy band of RECC. It is obvious in this case that there is absent one of the mentioned conditions: the ascending branch in the breeze cell, instability of the atmosphere and convergence of air flows in the sea-breeze front zone.

Table 2. Results of radar observations of the sea-breeze fronts in the north-western region of the Black Sea for the period of 1996-1999

Years / Denomination	1996	1997	1998	1999	Sum	Average
Number of days with SBF	36	38	35	30	139	34.7
Number of days with RECC on SBF with $\eta > 65$dBZ	5	6	12	9	32	8.0
Recurrence (%) of ratio of number of days with RECC on SBF with $\eta > 65$dBZ to number of days with SBF	13.9	15.8	34.3	30.0	94.0	23.5
Recurrence (%) of ratio of number of days with SBF to average number of days with breezes	62.1	65.5	60.3	51.7	239.6	59.9

In work [6] a chart of number of days with RECC in the radius of 300 km in days with evolution of the sea-breeze fronts with the value of radar reflectivity above 12 dBZ with resolution 30x30 km is obtained. However, practice of anti-hail protection requires construction of a chart of number of days with radar reflectivity above 65 dBZ, but with higher space resolution in order to reveal general regularities of distribution of hail-hazardous cumulonimbus clouds evolving on the sea-breeze fronts. Taking into account the fact that radar parameters of hail-hazardous cumulonimbus clouds for MRL-5 are most representatively measured in the radius 100-150 km, this chart was constructed in the radius of 100 km from the radar location. The investigated territory of the north-western regions of the Black Sea was divided into squares 10x10 km. In the coordinates "azimuth-range" all cases with radio-echo from the hail-hazardous cumulonimbus clouds with radar reflectivity $\eta > 65$ dBZ were plotted and they were summed up in each square for the period of four years. Then isolines of equal values of number of days with RECC were drawn (Fig.1).

The chart analysis shows that distribution of the number of days with RECC with the radar reflectivity $\eta > 65$ dBZ is characterized by high spotted in both directions perpendicular and parallel to the coast line. It is seen from Fig.1 that the sea breeze penetration depth averages 20-25 km, and the distance between the maxima centers is multiple by 25 km, i.e. by the sea-breeze penetration depth.

If one unites the maxima centers, the obtained picture will resemble meso-scale cellular structure of thunderstorm-hail processes, in the units of which maxima of number of days of RECC with $\eta > 65$ dBZ are registered (Fig.1-b).

Thunderstorm-hail process (THP) is a process of evolution of cumulonimbus clouds (scale of several hundreds kilometers) of frontal or air-mass character in the atmosphere leading to formation of thunderstorms, showers, hail, squall. Methods for obtaining and analysis of thunderstorm-hail processes are given in [5, 6].

In works [3, 6] it is shown that the convergence zone formed in result of interaction between seaward background flow with breeze circulation varies in time and covers the coast strip (100-150 km), where in the presence of unstable stratification Cb evolve. The convergence zone width and its value depend on characteristics of both large-scale background flow and breeze [8]. In this zone there are formed meso-scale circulation systems of movement of the Benar open cell type (meso-β-scale), which exist during several hours. Appearance of new Cb and evolution of already existing Cb on the sea-breeze fronts occur in the zones of updrought of regular structures with characteristic size of mesocells in the RECC field 30-40 km horizontally [6]. In work [5] there is made a conclusion on determinacy of atmospheric processes of meso-γ-scale, i.e. cloud-scale, by circulations of meso-β-scale. Existence of these circulations against the background of larger scale determines limits of predictability of meso-γ-scale processes [5]. Meso-scale movements are classified according to [9].

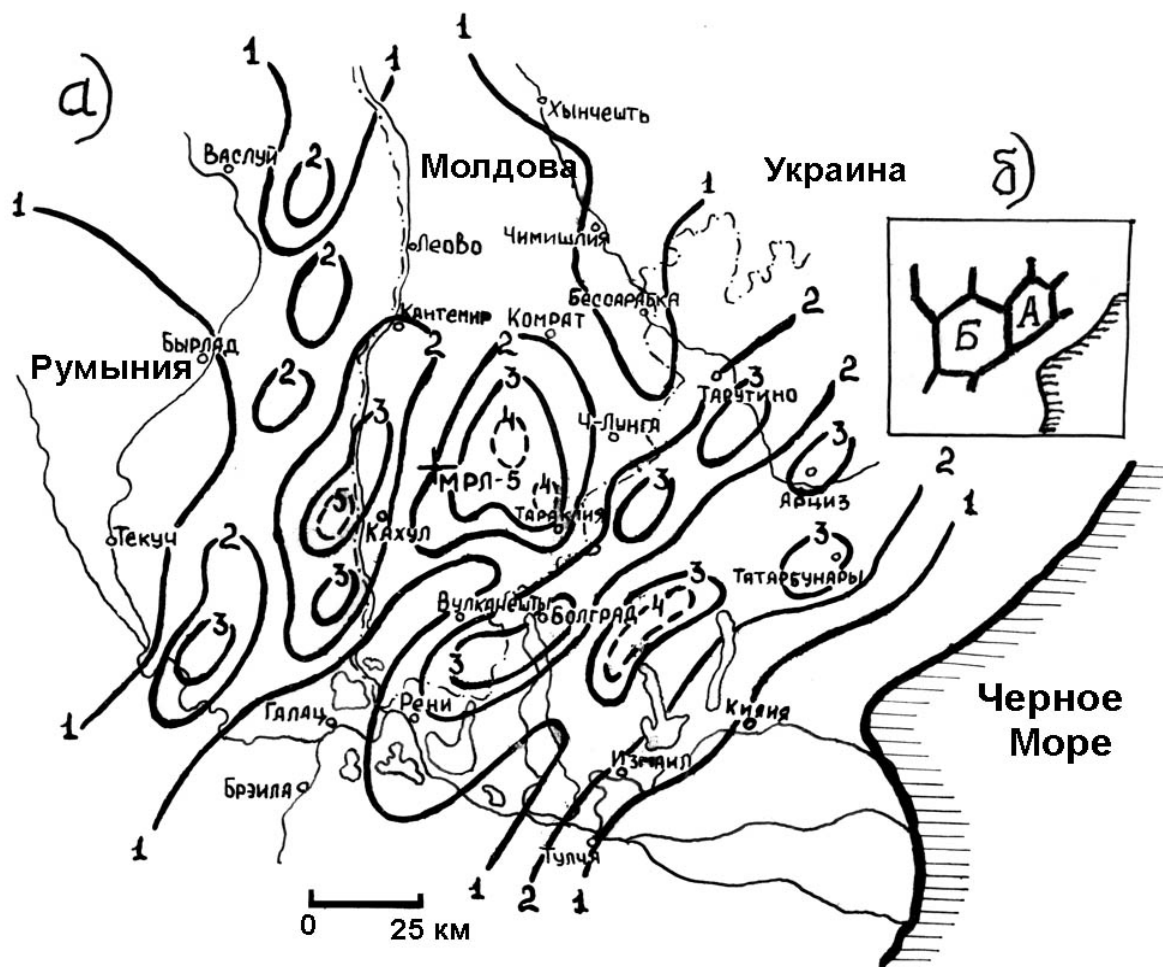Fig.1. Chart of number of days of RECC with radar reflectivity $\eta>65$ dBZ in the days with evolution of the sea-breeze fronts for the period of 1996-1999 in the radius 100 km (a) and scheme of meso-scale cellular structure of maxima of number of days of RECC with $\eta>65$ dBZ (b). Average diameter of mesocell A is 40 km, of mesocell B - 60 km. Location of the radar МРЛ-5 is marked by cross.

Meso-scale cellular structure of cumulonimbus clouds evolution is the most obviously pronounced at weaken background flow characterized by small values of velocity of steering flow and vertical shear of wind with height (no more than 1 m/s per kilometer all over the troposphere) [7], this being typical for aerologic structure of the sea-breeze fronts [2, 3, 6].

In this case average diameter of mesocell A is 40 km, and that of mesocell B - 60 km (Fig.1-b). In central parts of mesocells number of days of RECC with $\eta > 65$ dBZ is less than along the sides and in units of the meso-scale net, i.e. for meso-scale processes of this type, regions of maxima of number of days of RECC with $\eta > 65$ dBZ are geographically determined by higher recurrence of hail-hazardous cumulonimbus clouds than in neighboring regions. This property must be taken into account for planning of anti-hail protection system and for estimation of efficiency of active influences. In the South of the Republic the maxima distribution of number of days of RECC with $\eta > 65$ dBZ is located in its central part between the towns Kahul, Taraklia, Chadyr-Lunga and in the lower part of the near-Prut lowland.

It should be noted one more ecological peculiarity concerning the problems of the sea-breeze fronts. Contaminants carried by night (coast) breeze to the sea area, in the day-time with day (sea) breeze evolving may be carried back to the coast zone, where being drawn into the processes of cloud-precipitation formation, may deposit on the surface of the Earth. In the zones of maximum of number of days of RECC with $\eta > 65$ dBZ level of contamination is expected to be higher than in neighboring territories.

The results given in Fig.1 are in a good agreement with the data presented in [4], where a chart of average annual number of days with hail in the south-western Odessa region was obtained taking into account all types of thunderstorm-hail processes evolving in this region.

Table 3. Recurrence (%) of time of RECC existence with radar reflectivity $\eta > 65$ dBZ on the sea-breeze fronts for the period of 1996-1999

Denomination	Gradation, min					Sum
	1.0-3.0	3.5-5.0	5.5-7.0	7.5-9.0	> 9	
Number of cases	94	37	27	20	17	195
Recurrence, %	48.2	19.0	13.8	10.3	8.7	100

Note. Discrepancy of number of cases of RECC with $\eta > 65$ dBZ and number of days with the sea-breeze fronts is explained by the presence of several cases of RECC with $\eta > 65$ dBZ in the same day.

Table 3 presents recurrence of time of existence of RECC with radar reflectivity $\eta > 65$ dBZ on the sea-breeze fronts. It is seen from Table 3 that the highest recurrence of existence of RECC with $\eta > 65$ dBZ falls on gradation 1.0-3.0 minutes (48.2%). Only 8.7% cases fall on gradation >9 minutes. Area of the RECC with radar reflectivity $\eta > 65$ dBZ near the Earth changes within the limits of $1 \div 10$ km^2 (100-1000 ha), and the longer existence of RECC with $\eta > 65$ dBZ the larger the area.

For practice it is very interesting to reveal direction of evolution of hail-hazardous cumulonimbus clouds relative to the steering flow, i.e. the direction wherein new hail convective cells appear. For the steering flow the velocity and direction of wind per 600 hPa was taken [7]. For this purpose 20 of hail-hazardous cumulonimbus clouds with convective cells reaching $\eta > 65$ dBZ were studied. The results are given in Table 4.

Table 4. Recurrence (%) of directions of evolution of hail-hazardous cumulonimbus clouds relative to the steering flow

Denomination	To the left of the flow	To the right of the flow	Upflow	Downflow	Sum
Number of cases	3	5	10	2	20
Recurrence, %	15	25	50	10	100

It is seen from Table 4 that direction of evolution of hail-hazardous cumulonimbus clouds may occur in any direction relative to the steering flow; however prevailing evolution (50%) is found at upflow evolution.

Analysis of 139 studied the sea-breeze fronts has shown that in all the cases one-cell (8%) and multi-cell disordered (92%) thunderstorm-hail processes (THP) are evolved on them. Super-cell and ordered multi-cell THP have not been found in the studied cases. This is connected with a certain thermobaric structure of the atmosphere in days with evolution of the sea-breeze fronts, when there are absent vertical wind shears with height both in direction and velocity typical for super-cell and multi-cell ordered THP. The classification of THP is given by [1].

Conclusions

The results of the carried out investigations allow us to make the following conclusions:

1. The sea-breeze fronts are the most frequently shown in the period from noon to 2 p.m. (50.4%), and hail-hazardous cumulonimbus clouds evolving on them from 4 p.m. to 6 p.m. (40.5%).
2. In the breeze period for the north-western regions of the Black Sea in average in 59.9% cases RECC evolution on the asea-breeze fronts is observed, in 23.5% cases of them evolution of RECC with radar reflectivity $\eta > 65$ dBZ is registered.
3. The chart of number of days of RECC with radar reflectivity $\eta > 65$ dBZ in the days with evolution of the sea-breeze fronts for the period of 1996-1999 in the radius 100 km is obtained. The chart has meso-scale cellular structure with characteristic linear horizontal size of 40 and 60 km, in its units maxima of number of days of RECC with $\eta > 65$ dBZ are observed.
4. The highest recurrence of existence of RECC with $\eta > 65$ dBZ falls on gradation 1.0-3.0 minutes (48.2%). Only 8.7% cases fall on gradation >9 minutes.
5. Direction of evolution of hail-hazardous cumulonimbus clouds may occur in any direction relative to the steering flow, however prevailing evolution (50%) is found at evolution up flow.
6. On the sea-breeze fronts in the north-western regions of the Black Sea one-cell (8%) and multi-cell disordered (92%) THP are evolved. Super-cell and ordered multi-cell THP have not been found in the studied 139 cases.
7. In the south of the Republic the maxima distribution of number of days with RECC with $\eta > 65$ dBZ is located in its central part between the towns Kahul, Taraklia, Chadyr-Lunga and in the lower part of the near-Prut lowland.

References

[1] M.T. Abshaev, Trudy VGI, 53, 6 (1984).

[2] E.A. Burman, L. Gidrometeoizdat, 342 (1969).

[3] V.G. Voloshin, V.I. Petrov Active influence on hail processes in Moldova (in Russian), 4, 217 (2004).

[4] E.I. Danov, G.M. Danova Meteorology, climatology and hydrology (in Russian), 17, (1981).

[5] A.A. Zhelnin, A.N. Starostin Meteorology and hydrology (in Russian), 10, 5 (1987).

[6] V.I. Petrov Meteorology, climatology and hydrology (in Ukranian), 48, 69 (2004).

[7] N.A. Ryazantsev, V.S. Shvetsov Problems of active influence on atmospheric processes in Moldova (in Russian), 1, 51 (1986).

[8] B.W. Atkinson, Academic Press, 495 (1981).

[9] I. Orlanski, Bull. Am. met. Soc., 56, 527 (1975).

ON THE OCCASION OF THE 75$^{\text{TH}}$ BIRTHDAY OF ACADEMICIAN DUMITRU GITSU, DOCTOR HABILITY IN PHYSICS AND MATHEMATICS, MOLDOVA STATE PRIZE LAUREATE

Dumitru Gitsu was born on January 13, 1931 in v. Drepcautsi, region Briceni, the Republic of Moldova. He is a specialist in the physics of semimetals and narrow gap semiconductors. he is doctor hability in physics and mathematics (1973), assistant professor (1985), Associate member (1976), academician (1984). In 1949 D. Gitsu has finished middle school in Lipcani, R.Moldova. In 1954 he has graduated from the State University of Moldova. In 1956-1959 he is a post-graduate student of the A. Gertsen State Pedagogical University of Leningrad (Sanct-Petersburg), physics department, where in 1961 he becomes a Doctor in physics and mathematics, and in 1973 he receives the Diploma of Doctor hability degree in physics and mathematics.

Acad. D. Gitsu has begun his working activities as a lecturer of the Tiraspol Pedagogical Institute (1954-1956) and of the Moldova State University (1960-1961). Since 1961 D. Gitsu works in the Academy of Sciences of Moldova. His employment in the ASM was the following: Junior research scientist (1961-1962); Research scientist, Senior research scientist (1962-1969); Head of Laboratory (since 1969); Director-deputy on scientific problems, Institute of Applied Physics of AS of Moldova (1974-1978); Chief academician-secretary of the Presidium of the AS of Moldova (1978-1984); Academician-secretary of the Physics and mathematics department (1984-1995); Director of the Center "International Laboratory of High Temperature Superconductivity and Solid State Electronics" (1995-2000); Director of the Specialized Bureau on Solid State Electronics (2000 - to present).

Scientific interests of acad. D. Gitsu are shown in a wide spectrum of problems:

Physics of semimetals and narrow-gap semiconductors, technology of growth of single crystals; peculiarities of impurity states in systems with weak degeneration of carriers determined by overlapping of energy bands; dimensionality influence on classical and quantum electron phenomena; high temperature superconductivity; binary and ternary compounds and their alloys - isoelectronic analogues of five-valent semimetals; topological

phase transitions; nonlinear electron processes in submicron and nanodimensional single crystal wires; tensoelectric phenomena. There was solved phenomenological and microscopic theory of anisotropy of electron transport phenomena in arbitrary classical magnetic fields on the basis of polynomial representations of kinetic coefficients; there were explained peculiarities and variability of efficiency of impurities in semimetals. There was experimentally found phenomenon of the magnetic flux quantization in submicron bismuth wires.

Effect of quantization of a magnetic stream in a normal (nonsuperconducting) condition in simply connected geometry in submicron and Bi nanowires for the first time was developed. The effect is a subject of broad discussion in International publications, scientists with world famous names, such as: S. Washburn and R.A. Webb. Rep. Prog. Phys. 55 (1992) 1311-1383; U. Sivan, Y. Imry, C. Hartzstein. Phys. Rev. B, v.39, N 2, (1989), 1242-1249; V. Chandrasekhar, M.J. Rooks, S. Wind, D.E. Prober. Phys. Rev. Lett. V.55, N 15, (1985), 1610-1613.

On the basis of this large fundament of the accumulated theoretical-experimental knowledge, there was elaborated a number of original transducers and devices being superior the existing ones (angular anisotropic transducers, nonselective radiation detectors, vacuummeters, microrefrigerators for deep cooling, set of transducers for research in medicine, biology, etc.), which were awarded to medals and diplomas at international and republican exhibitions.

On this basis there was created a center for investigation of electrophysical properties of solids with diverse possibilities to study transport phenomena, including dimensional and quantum ones in magnetic field.
Parallel to fundamental studies there were elaborated several types of sensors and measuring devices: vacuummeters, pyrometers, etc., being utilized in diverse spheres of industry and applied scientific researches, including those in cosmic space.

Proceeding from the decisive role of sophisticated experimental equipment in modern scientific researches and from the necessity of active implementation of obtained scientific results in practice for solving the most urgent social-economic problems, academician D. Gitsu became an initiator of organization in the Academy of "Center of design and technology in solid state electronics". On its basis there were open "Center of automation and metrology" and "Center of instrument-making for biology", and later - the Center "TEHMED" intended for elaboration of equipment for medicine. Acad. D. Gitsu was also an initiator of organization of Cryogenic center for obtaining of liquid nitrogen and helium, this made it possible to study properties of solids in Chisinau at the world level.

Profound combination of fundamental investigations and applied elaborations has created favourable conditions for intensive creative work of scientists and engineers, for training of highly skilled specialists, and for being recognized by specialists from the country and abroad.

D. Gitsu has published more than 500 scientific works, 2 monographs (coauthor), more than 30 inventor's certificates. Here we should mention that acad. D. Gitsu was a supervisor of 35 theses of doctor in physics and mathematics and of 4 theses of doctor hability (F. Munteanu, N. Popovici, A. Nikolaeva, P. Bodiul). Scientific works of the academician D.V. Gitsu are published in such journals as: JETP, Phys. Rev. Lett, Phys. St. Sol., Physica B, Science and Engineering, J. Thermoelectricity at al.

Acad. D. Gitsu is a member of the International thermoelectricity society, Honorary member of Tsielkovsky Cosmonaut Academy of Russia, Honorary professor of the University of Oradea (Romania), Honorary professor of the Pedagogical University of Balti, he is the

Moldova State Prize Laureate in science and technique, "Honoured Scientist" of the Republic of Moldova, he is awarded to "Order of the Republic".

D. Gitsu is a member of the editorial board of the International journal "Thermoelectricity", of the "Moldavian Journal of the Physical Sciences". He is awarded to two medals in the International Saloons of Inventions in Bruxelles (2001) and Geneva (2002). Acad. D. Gitsu is a Chairman of the Scientific Council on theses of doctor and doctor hability in solid state physics, he is a member of the Committee for attestation of scientific personnel.

Dumitru Vasile Gitsu helped many people, he supported them in difficult situations. He has celebrated his 75th anniversary being full of energy and creative power. In December 2005 he was approved as a deputy director of newly organized Institute of Electronics Engineering and Industrial Technologies. Plans on connection of science and industry may be realized in it.

We wish him health, creative longevity, success.

Editorial Board of the "Moldavian Journal of the Physical Sciences".